

UNIVERSITY OF BIRMINGHAM

Wideband Air-Filled Waveguide Antennas

by

Qingchun You

A thesis submitted to the University of Birmingham for the degree of DOCTOR OF PHILOSOPHY

School of Engineering
College of Engineering and Physical Sciences
University of Birmingham
January 2025

UNIVERSITY OF
BIRMINGHAM

University of Birmingham Research Archive

e-theses repository

This unpublished thesis/dissertation is copyright of the author and/or third parties. The intellectual property rights of the author or third parties in respect of this work are as defined by The Copyright Designs and Patents Act 1988 or as modified by any successor legislation.

Any use made of information contained in this thesis/dissertation must be in accordance with that legislation and must be properly acknowledged. Further distribution or reproduction in any format is prohibited without the permission of the copyright holder.

ABSTRACT

High-gain antennas play a crucial role in point-to-point and point-to-multipoint communication systems. In applications such as microwave backhaul, satellite communication, and radar systems, air-filled hollow waveguide array antennas have become a mainstream choice due to their low loss and high-gain characteristics. Meanwhile, dual-polarized antennas, with their ability to provide polarization diversity and enhance channel capacity in multipath fading environments, are pivotal in point-to-point communication systems. In satellite communication on-the-move systems, dual-polarized antennas enable arbitrary linear polarization, allowing for more effective tracking of the satellite's polarization state. This PhD thesis focuses on the design and performance optimization of dual-polarized, multiband co-aperture, and ultra-wideband waveguide array antennas. The primary contributions are as follows: (1) Present a compact corporate-fed dual-polarized array antenna: By implementing a novel one-to-one excitation method for individual radiating elements, this design effectively addresses the trade-offs between bandwidth, grating lobes, isolation, and cross-polarization performance in wideband dual-polarized arrays, significantly enhancing the overall antenna performance. (2) Present an innovative dual-mode back cavity design: This design operates in TE120/TE210 and TE140/TE410 modes and incorporates a diamond-shaped radiation slot, greatly improving the radiation bandwidth and pattern stability. Using SLA 3D printing technology followed by copper plating simplifies the manufacturing process, resulting in a compact and high-performance antenna array. This design achieved a 30.2% impedance bandwidth with high aperture efficiency and is the first to realize a 3D-printed dual-polarized array antenna with bandwidth exceeding 30%, fully covering the Ku-band satellite communication range of 10.7–14.5 GHz. (3) Present a unique dual-band, dual-polarized, shared-aperture waveguide array antenna design method: This method features a flexible frequency ratio design, catering to diverse application scenarios. An example design covering the K- and Ka-bands was fabricated and tested, making it the first planar array antenna to meet the Ka-band satellite communication transceiver bandwidth requirements (Rx: 17.7–21.2 GHz, Tx: 27.5–31 GHz). (4) Address the challenges in ultra-wideband antenna array design: By introducing an innovative design approach, this work achieves high aperture efficiency and a low-profile structure while effectively minimizing grating lobes. The ability to cover multiple frequency bands makes it particularly suitable for modern satellite communication and point-to-point microwave backhaul systems. This design achieves an unprecedented 105% fractional bandwidth with a profile height of just 0.3λ, representing a significant breakthrough in ultra-wideband antenna array technology. (5) Prevent a sub-terahertz corrugated horn fabricated using Micro Laser Sintering (MLS) metal 3D printing. A 45° inclined corrugation enables vertical printing without support, preserving circular symmetry and achieving >36 dB XPD. The integrated rectangular-to-circular waveguide transition enhances compactness, while optimized gold plating reduces ohmic loss. This is the first high-performance 3D-printed metal corrugated horn beyond 100 GHz, offering a new fabrication approach for millimeter-wave and terahertz applications.

ACKNOWLEDGEMENT

I would like to express my sincerest gratitude to my supervisor, Prof. Yi Wang. Throughout my Ph.D. journey, he has provided me with patient guidance and unwavering support. Not only did he offer valuable insights into my academic work, but he also gave me tremendous encouragement in life. Prof. Wang's humility and openness have inspired me to explore new research directions, and his mentorship has greatly benefited me, becoming a true role model in my academic pursuit. It has been an honor to be his student, and I am deeply thankful for the time and effort he dedicated to my growth.

I am also very grateful to my colleagues in the Emerging Device Technology research group. It is this harmonious and vibrant team that has made my research journey so enriching. Our interactions have constantly sparked new ideas, allowing me to experience the joy of exploring knowledge.

I extend my heartfelt thanks to my parents and my wife for their unwavering support and encouragement. Their love has been a source of strength and warmth throughout my academic journey.

PUBLICATIONS

Journals

1. Q. You, Y. Wang, M. Huang, J. Huang, Z. -W. Zheng and Y. Lu, "Wideband Dual-Polarized Hollow-Waveguide Slot Array Antenna," *IEEE Trans Antennas Propag*, vol. 70, no. 10, pp. 9326-9336, Oct. 2022, doi: 10.1109/TAP.2022.3184544.

2. Q. You, L. Qian and Y. Wang, "3D-Printed Wideband Dual-Polarized Hollow-Waveguide Antenna Array with Dual-Mode Back Cavity," *IEEE Trans Antennas Propag*, Submit in August. 2024, Under revise, after major revision.

3. Q. You, K. Ye, L. Qian, Y. Wang and J. Huang, "Wideband Corporate-Fed Dual-band Dual-polarized Long Slot Array Antenna for Satcom," *IEEE Trans Antennas Propag*, Submit in July. 2024, Under revise, after major revision.

4. Q. You and Y. Wang, "Ultra-Wideband, Low-Profile Waveguide Antenna Array with High Aperture Efficiency," *IEEE Trans Antennas Prop*ag, Prepared submissions.

5. Q. You, T. Skaik, P. Young, N. Miller, P. Hunyor, P. Huggard and Y. Wang., "Subterahertz Monolithic Metal 3D-Printed Corrugated Horn Antenna with High Cross-Polar Discrimination," *IEEE Trans. Terahertz Sci. Technol*, vol. 15, no. 1, pp. 128-132, Jan. 2025, doi: 10.1109/TTHZ.2024.3501585.

Conference

1. Q. You, Y. Wang and N. Miller, "High-Efficiency Low-Profile Waveguide Array Antennas," *2022 International Workshop on Antenna Technology (iWAT)*, Dublin, Ireland, 2022, pp. 6-8, doi: 10.1109/iWAT54881.2022.9811029.

Contents

ABSTRACT I

ACKNOWLEDGEMENT II

PUBLICATIONS III

Journals III

Conference III

CHAPTER 1: INTRODUCTION 1

1.1 Background and Motivation 1

1.2 Novelty and Contributions of the Thesis 2

1.3 Outline of the Thesis 3

References 5

CHAPTER 2: LITERATURE REVIEW 7

2.1 Planar Hollow Waveguide Array Antennas for Millimeter-Wave Applications 7

2.1.1 Series-Fed and Partially Corporate-Fed Waveguide Slot Array Antennas 7

2.1.2 Fully Corporate-Fed Waveguide Slot Array Antennas 8

2.1.3 Dual-Linear Polarized Waveguide Slot Array Antennas 9

2.1.4 Dual-Circularly Polarized Waveguide Slot Array Antennas 10

2.1.5 Multi-Band Shared-Aperture Dual-Polarized Waveguide Array Antennas 12

2.2 Monolithic Metal 3D-Printed Corrugated Horn Antenna for Sub-Terahertz Applications 14

2.3 Discussion on the State-of-the-art and Research Objectives 15

2.4 Summary 16

References 18

CHAPTER 3: Wideband Dual-Polarized Hollow-Waveguide Slot Array Antenna 22

Abstract 23

3.1 Introduction 24

3.2 Antenna Configuration 26

3.3 Analysis and Design 26

3.3.1 Array Element 27

3.3.2 Feed networks in Sub-array 30

3.4 Experimental verification 34

3.4.1 Reflection Coefficient and Isolation 35

3.4.2 Radiation patterns and Efficiency 37

3.4.3 Comparison 37

3.5 Conclusion 38
Reference 39
CHAPTER 4: 3D-Printed Wideband Dual-Polarized Hollow-Waveguide Antenna Array with Dual-Mode Back Cavity 42
Abstract 43
4.1 Introduction 44
4.2 Design and Analysis 46
4.3 2×2 sub-array 46
4.3.1 Dual-mode Back Cavity 47
4.3.2 Design Variation of The Radiation slots 48
4.3.3 Wideband OMT 50
4.4 Feeding Network 51
4.4.1 Differential Feeding Network for Vertical Polarization 51
4.4.2 In-phase Feeding Network for Horizontal Polarization 52
4.5 Experimental Results 53
4.5.1 Manufacturing and Surface Treatment 53
4.5.2 S-parameters 55
4.5.3 Radiation Performance 55
4.5.4 Comparison 56
4.6 Conclusion 57
References 58
CHAPTER 5: Wideband Corporate-Fed Dual-band Dual-polarized Long Slot Array Antenna for Satcom 61
Abstract 62
5.1 Introduction 63
5.2 Overview of Antenna Array Configuration 64
5.3 Evolution and Analysis 65
5.3.1 Design Evolution (2×2 Array) 65
5.3.2 Bandstop structure to suppress leakage between the two polarizations 66
5.3.3 Evaluation of the maximum allowed frequency ratio 67
5.4 DESIGN AND SIMULATION 69
5.4.1 Performance Comparison of the 2×2 Subarrays 69
5.4.2 DBDP PPW feeding network 69
5.4.3 Orthogonal Line Source Generator (LSG) and in-phase combiners 71
5.4.4 Complete Array Antenna and method for Generating Circular Polarization .. 73

5.5 Experimental Verification 75
5.5.1 Reflection Coefficient and Port Isolation 78
5.5.2 Radiation patterns and Efficiency 78
5.5.3 Comparison 79
5.6 Conclusion 80
References 80
CHAPTER 6: Ultra-Wideband Low-Profile Waveguide Antenna Array with High Aperture Efficiency 84
Abstract 85
6.1 Introduction 86
6.2 Overview of Antenna Configuration 87
6.3 Wideband Antenna Element – Design Theory 88
6.3.1 Evolution from TE10 to Quasi-TEM Mode Radiator 88
6.3.2 Bandwidth limit factors of the quasi-TEM mode radiator 89
6.3.3 Impact of ω/P_x on aperture efficiency and bandwidth 89
6.4 Wideband Antenna Element – Design Procedure 92
6.4.1 Determining the dimensions of double-ridged waveguide 92
6.4.2 Determining the period P_x 92
6.4.3 Transition from double-ridged waveguide to free space 92
6.4.4 Eight-element linear array 93
6.5 Array and Feeding Network 93
6.5.1 Feeding configuration 93
6.5.2 Rectangular-coaxial-to-ridge-waveguide transition 94
6.5.3 1-to-4 feeding network of the 2×2 sub-array 95
6.5.4 1-to-16 corporate feeding network for complete array 96
6.6 Experimental Results 97
6.6.1 S Parameters 98
6.6.2 Radiation Performance 98
6.6.3 Comparison 99
6.7 Applications for SATCOM and mmWave backhaul 100
6.8 Conclusion 100
CHAPTER 7: Sub-Terahertz Monolithic Metal 3D-Printed Corrugated Horn Antenna with High Cross-Polar Discrimination 104
Abstract 105
7.1 Introduction 106

7.2 Configuration and Design 107
7.2.1 Rectangular-to-circular waveguide adapter 108
7.2.2 TE_{11}- HE_{11} mode converter 108
7.2.3 Linear-profile corrugated horn 109
7.3 Fabrication and Experimental Results 110
7.4 Conclusion 112
CHAPTER 8: Conclusions and Future Work 115
8.1 Conclusions 115
8.2 Future Work 116

CHAPTER 1: INTRODUCTION

1.1 Background and Motivation

With the rapid development of multi-band, multi-functional wireless communication systems, there is an increasing demand for antennas that can support multiple operating frequency bands. For instance, frequencies such as 6/7/8/11/13/15/18/23/60/70/80 GHz have been allocated for point-to-point microwave backhaul systems [1], and the Ku (10.7–14.5 GHz), K (17.7–21.2 GHz) and Ka (27.5–31 GHz) are already widely used in satellite communications (SATCOM) [2]. In these scenarios, wideband or multi-band shared-aperture waveguide array antennas with high-gain capabilities are highly desirable.

Furthermore, flexible polarization configurations are widely utilized to enhance communication quality. For example, dual-linearly polarized antennas are employed in point-to-point microwave backhaul systems to increase channel capacity and transmission data rates [3]. Circular polarization (CP) is extensively used in satellite communication and radar systems due to its insensitivity to antenna orientation, strong signal penetration capability, and reduced multipath interference. In many transceiver systems, CP in the transmit and receive bands is orthogonal, which helps to increase isolation between transmit and receive paths [4].

Polarization-reconfigurable and multi-polarization shared-aperture antennas have found widespread applications in modern communication systems [5], as they not only improve spectral efficiency and enhance communication link reliability but also allow efficient integration of multi-service, multi-band operations. This integration capability is essential to meet the demands of future communication systems for high data rates, high reliability, and multifunctional operation.

An effective approach to achieving multi-band and multi-polarization shared-aperture performance is the use of wideband or multi-band shared-aperture dual-linearly polarized waveguide array antennas. All forms of polarization can be synthesized through the two orthogonal polarization channels of a dual-polarized antenna. For instance, in communication-on-the-move systems, polarization tracking can be achieved using arbitrary polarization synthesis networks based on dual-polarized antennas [6]. Circular polarization can also be synthesized by adding a 3 dB coupler to the dual-polarized input ports, achieving dual circular polarization [7].

Published dual-linearly polarized waveguide array antennas can be categorized into several types: those based on waveguide orthomode couplers [8], multi-port orthogonal excitation directly radiating elements [9], CTS (Continuous Transverse Stub) dual-polarized array antennas [10], [11], and multi-band nested shared-aperture dual-polarized antennas [7]. The bandwidth of current wideband dual-polarized array antennas is typically limited either by the feed network or by the fundamental mode bandwidth of the radiating slots. The widest bandwidth reported for such antennas is about 30% [9], [12]. For dual-band shared-aperture designs, radiating slots are usually nested for the two frequency bands, which inherently restricts design flexibility, making it difficult to adapt the frequency ratio to system requirements [7].

Another approach for designing multi-band, multi-polarization shared-aperture antennas is to add a multi-band polarizer with an FSS (Frequency Selective Surface) structure onto an ultra-wideband linearly polarized antenna [13]. However, this approach

imposes even more stringent bandwidth requirements on the waveguide array antenna. For example, point-to-point microwave backhaul systems operate across multiple bands from 6 up to 86 GHz, while high-throughput satellites cover the 10.7–31 GHz range. The widest bandwidth achieved by currently published waveguide array antennas is around 60%, which still falls short of the requirements for these demanding applications [14].

Therefore, expanding the bandwidth of dual-polarized array antennas, innovating multi-band shared-aperture topologies, and realizing ultra-wideband linearly polarized antennas are of great importance for high-capacity communication systems. These advancements will be critical in meeting the evolving needs of next-generation wireless communication systems.

As the operating frequency approaches the terahertz range, planar array antennas become increasingly challenging to manufacture and assemble. The corrugated horn antenna, known for its ease of integration and flexible beam-shaping capabilities, is widely employed as a primary feed source for reflector antennas in applications such as radio astronomy and precision measurement instruments [15]. These antennas require circular symmetric radiation, low sidelobes, and high cross-polarization discrimination (XPD), making their fabrication highly demanding. Traditional manufacturing methods, such as direct machining [16] and electroforming [17], face significant limitations at sub-terahertz frequencies due to stringent precision requirements, high production costs, and long fabrication cycles. The complexity of machining fine corrugations with a depth-to-width ratio of 3–4 or the need for delicate mandrels for electroforming further constrain the scalability.

The emergence of metal 3D printing offers a promising alternative, but existing laser powder bed fusion (LPBF) techniques suffer from insufficient precision, poor surface roughness, and unwanted structural asymmetry caused by tilted printing orientations [18]. These issues degrade radiation performance, especially at higher frequencies.

1.2 Novelty and Contributions of the Thesis

This thesis addresses the current challenges in the bandwidth enhancement for dual-polarized waveguide array antennas, introduces novel topologies for multi-band shared-aperture dual-polarized antennas, and develops new design methodologies for ultra-wideband waveguide array antennas. It also explores the application of high-precision Micro Laser Sintering (MLS) metal 3D printing by demonstrating a high-performance sub-terahertz corrugated horn antenna. The specific novelty and contributions of this research work are summarized as follows:

(1) In Chapter 3, this work overcomes the performance trade-off in wideband dual-polarized arrays between bandwidth, grating lobe, isolation and cross polarization by using a number of new design features. The key one is a new topology of two sets of full-corporate-feed networks implemented using two different transmission structures (square coaxial line and ridge waveguide, respectively). This topology ensures wideband impedance matching, facilities signal routing and effectively minimizes the space between the array elements. It excites the radiation slots in a one-to-one fashion without requiring backed cavities. This improves the antenna's radiation performance across a wide frequency band. This demonstration provides a promising wideband dual-pol antenna solution for high data-rate wireless applications.

(2) In Chapter 4, this work introduces a novel dual-mode back cavity operating in TE120/TE210 and TE140/TE410 modes, combined with a diamond-shaped radiation slot, to significantly enhance radiation bandwidth and pattern stability. Utilizing stereolithography apparatus (SLA) 3D printing technology and subsequent copper plating simplifies the manufacturing process, resulting in a compact and high-performance antenna array. This design achieves a 30.2% impedance bandwidth and high aperture efficiency, outperforming published designs and making it highly suitable for practical applications.

(3) In Chapter 5, this work addresses key challenges in dual-band dual-polarized (DBDP) antenna array design by introducing several notable innovations. The use of an orthogonal parallel plate waveguide (PPW) for dual polarization excitation offers an efficient and compact solution, directly tackling issues of polarization purity and feed network complexity. To further enhance performance, dual-band band-stop structures are integrated within the PPW network, effectively suppressing polarization leakage and significantly improving transmission efficiency—an area where many conventional designs fall short. Moreover, the design accommodates a wide frequency ratio range from 1 to 2.64 between the two bands, providing the flexibility needed to support a broad range of practical applications. The introduction of a novel orthogonal linear signal generator (LSG) enables ultra-wideband, dual-polarized quasi-TEM excitation, ensuring consistent performance across an expansive bandwidth.

(4) In Chapter 6, this work addresses the challenges of grating lobes and aperture efficiency degradation in traditional ultra-wideband waveguide slot arrays, especially at mm-wave frequencies. This is achieved by a low-profile quasi-TEM radiator that is directly excited by a corporate feed network constructed from rectangular coaxial waveguides. This approach enables smooth impedance transitions and maintains a compact feed structure. As a result, the design achieves a remarkable 105% fractional bandwidth across the 10 to 32 GHz range, with an aperture efficiency exceeding 90%. This achievement marks the first instance of a full-metal, air-filled planar waveguide antenna delivering such a broad bandwidth with a low-profile configuration.

(5) In Chapter 7, this work demonstrates a horn antenna with 45° inclined corrugations, enabling vertical 3D printing without internal support. This preserves circular symmetry of the structure and enhances cross-polarization discrimination (XPD). The rectangular-to-circular waveguide transition is integrated within a monolithic compact structure, avoiding minimizing assembly-induced losses. The MLS process achieves 10 μm precision and 1.8 μm surface roughness, overcoming the limitations of conventional LPBF techniques. The optimized electroless nickel and gold plating process enhances conductivity and reduces ohmic loss, allowing the antenna to approach the performance of ideal metals. These advancements enable the first high-performance 3D-printed metal corrugated horn beyond 100 GHz, achieving >36 dB XPD and 18–22 dBi gain over 145–225 GHz.

1.3 Outline of the Thesis

The thesis is presented as a series of published or under-review papers following the University's Alternative Format Thesis guidelines. The thesis comprises eight chapters, organized as follows:

Chapter 1: This chapter introduces the research background and motivation. It outlines the primary contributions of the thesis and provides an overview.

Chapter 2: A detailed literature review is presented, covering topics from horn antennas, series-fed waveguide slots arrays, fully corporate-feed waveguide antenna arrays, dual-polarized waveguide antenna arrays to muti-band shared-aperture dual-polarized waveguide antenna arrays.

Chapter 3: A wideband dual-polarized slot array antenna based on hollow-waveguide is presented in this chapter. Its wide bandwidth and high performance are enabled by two separate feeding networks, from the side and the bottom, using square coaxial line and ridge waveguide structures, respectively. The full-corporate-feed networks excite the radiation slots in a one-to-one fashion without using backed cavities. Tight element spacing is made possible, suppressing the grating lobe and maintaining high cross polarization discrimination (XPD) across the wideband. This resolves a usual trade-off between bandwidth and grating lobe. A double-ridge rectangular waveguide cavity is devised as an orthogonal mode splitter for isolation enhancement. Several design features are used to minimize the signal path length and facilitate routing. An 8×8-element prototype in K-band is designed, fabricated, and measured. Experimental results show that the antenna has a wide bandwidth of 23.4% (from 17 – 21.5 GHz) free from grating lobes. More than 25.5 dBi peak gain, higher than 51.2 dB isolation and over 43.6 dB XPD are obtained for the dual polarizations.

Chapter 4: This chapter presents a novel wideband dual-polarized hollow-waveguide antenna array, designed for manufacturing using stereolithography (SLA) 3D printing technology and metallized by copper plating. By replacing the conventional single-mode back cavity with a dual-mode (TE120/TE210 and TE140/TE410 modes) back cavity, a wider radiation bandwidth is achieved. A diamond-shaped radiation slot was employed to enhance the stability of the radiation pattern and mitigate gain drop-off at higher frequencies. Two different types of feeding networks were used for the two polarizations. For the vertical polarization, a novel, highly compact differential feed network was devised under severe space constraint while allowing the ease of printing and plating. The fabricated antenna array prototype achieves an impedance bandwidth of 30.2% (10.7-14.5 GHz), with measurements confirming high aperture efficiency (AE > 72%) and high port isolation (>48 dB).

Chapter 5: This chapter presents a design approach for dual-band dual-polarized (DBDP) waveguide antenna array. A novel transmission network using orthogonal parallel plate waveguide (PPW) is proposed for the excitation of dual polarization. Dual band bandstop structures are incorporated into the PPW feeding network. They suppress the leakage between the two polarizations and improve the transmission efficiency of the network. They also enable a wide range of frequency ratio from 1 to 2.64 between the two bands. A new orthogonal linear signal generator (LSG) enables ultra-wideband, dual-polarized quasi-TEM excitation, ensuring consistent and reliable performance across a broad bandwidth. Fed by four sequentially rotated single-ridge 1-to-4 power dividers, the LSG effectively generates dual-polarized signals. For demonstration, a K/Ka-band shared-aperture dual-polarized array antenna has been designed, analyzed and experimentally verified. The array features a wide impedance bandwidth (17.7 - 21.2 GHz and 27.5 - 31 GHz), high isolation (>50 dB), and excellent cross polarization discrimination (XPD) (>40 dB). The prototype demonstrates high aperture efficiency up to 80% and consistent radiation patterns at both bands, affirming its potential for SATCOM systems.

Chapter 6: This chapter presents a novel ultra-wideband planar antenna design featuring a low-profile quasi-TEM radiator directly excited by a corporate feed network constructed from rectangular coaxial waveguides. The design addresses key challenges, such as grating lobes and aperture efficiency degradation, ensuring a compact and efficient solution. The key innovations include quasi-TEM mode radiators, ultra-wideband rectangular coaxial-to-ridge waveguide transition, and in-phase air-filled corporate feed network based on rectangular coaxial line. The design achieves an impressive fractional bandwidth (FBW) of 105% across the 10–32 GHz range, with an aperture efficiency of up to 80% and a low-profile height of 0.28 wavelengths at the lowest frequency. The antenna structure is fully metal and manufactured using CNC machining, with laser cutting employed for the coaxial core layer. Experimental results show excellent agreement with simulations, confirming the potential for use in SATCOM and other wideband point-to-point communication systems.

Chapter 7: This chapter presents the design, fabrication, and characterization of a high-performance sub-terahertz corrugated horn antenna manufactured using Micro Laser Sintering (MLS) metal 3D printing. A 45° inclined corrugation design enables vertical printing without internal support, preserving circular symmetry and achieving >36 dB XPD. The integration of a rectangular-to-circular waveguide transition enhances compactness and eliminates assembly errors. The MLS process, achieving 10 μm precision and 1.8 μm surface roughness, overcomes the limitations of conventional LPBF techniques. An optimized electroless nickel and dual-layer gold plating process improves conductivity and reduces ohmic loss. Experimental validation confirms a measured gain of 18–22 dBi over 145–225 GHz, marking the first demonstration of a high-performance 3D-printed metal corrugated horn beyond 100 GHz. This work establishes a new pathway for advanced millimeter-wave and terahertz antenna fabrication.

Chapter 8: The final chapter concludes the thesis by summarizing the key findings and contributions. It also discusses the research limitations and suggests potential directions for future work.

References

[1] T. Suzuki, J. Hirokawa, and M. Ando, “Iteration-free design of waveguide slot array with cavities,” *IEEE Trans Antennas Propag*, vol. 58, no. 12, pp. 3891–3897, Dec. 2010, doi: 10.1109/TAP.2010.2078435.

[2] K. Hashimoto, J. Hirokawa, and M. Ando, “A post-wall waveguide center-feed parallel plate slot array antenna in the millimeter-wave band,” *IEEE Trans Antennas Propag*, vol. 58, no. 11, pp. 3532–3538, Nov. 2010, doi: 10.1109/TAP.2010.2071356.

[3] S. Park, Y. Tsunemitsu, J. Hirokawa, and M. Ando, “Center feed single layer slotted waveguide array,” *IEEE Trans Antennas Propag*, vol. 54, no. 5, pp. 1474–1480, May 2006, doi: 10.1109/TAP.2006.874310.

[4] M. Ando, Y. Tsunemitsu, M. Zhang, J. Hirokawa, and S. Fujii, “Reduction of long line effects in single-layer slotted waveguide arrays with an embedded partially corporate feed,” *IEEE Trans Antennas Propag*, vol. 58, no. 7, pp. 2275–2280, Jul. 2010, doi: 10.1109/TAP.2010.2044346.

[5] H.-Y. Lee’, G.-C. Kang’, and B. Lee’, “Cavity-Backed Planar Slot Array Antenna with a Single Waveguide-Fed Sub-array.” vol. 58, no. 7, pp. 2275–2280, Jul. 2010, doi: 10.1109/TAP.2010.2044346.

[6] Y. Miura, J. Hirokawa, M. Ando, Y. Shibuya, and G. Yoshida, "Double-layer full-corporate-feed hollow-waveguide slot array antenna in the 60-GHz band," *IEEE Trans Antennas Propag*, vol. 59, no. 8, pp. 2844–2851, Aug. 2011, doi: 10.1109/TAP.2011.2158784.
[7] G. L. Huang, S. G. Zhou, T. H. Chio, H. T. Hui, and T. S. Yeo, "A low profile and low sidelobe wideband slot antenna array feb by an amplitude-tapering waveguide feed-network," *IEEE Trans Antennas Propag*, vol. 63, no. 1, pp. 419–423, Jan. 2015, doi: 10.1109/TAP.2014.2365238.
[8] L. Qin, Y. Lu, Q. You, Y. Wang, J. Huang, and P. Gardner, "Millimeter-wave slotted waveguide array with unequal beamwidths and low sidelobe levels for vehicle radars and communications," *IEEE Trans Veh Technol*, vol. 67, no. 11, pp. 10574–10582, Nov. 2018, doi: 10.1109/TVT.2018.2866245.
[9] J. Y. Zhang, J. D. Zhang, and W. Wu, "Single-Layer Planar Waveguide Array Antenna with High Antenna Efficiency," *IEEE Antennas Wirel Propag Lett*, vol. 21, no. 6, pp. 1153–1157, Jun. 2022, doi: 10.1109/LAWP.2022.3159827.
[10] X. Wang, Y. Li, F. Sun, J. Wang, L. Ge, and B. Ai, "A Millimeter-Wave 51% Bandwidth High-Gain 3-D-Printed Antenna Array Based on Optimized Multistage Phase Cancellation in Feed Network," *IEEE Trans Antennas Propag*, vol. 71, no. 12, pp. 10003–10008, Dec. 2023, doi: 10.1109/TAP.2023.3314102.
[11] H. Zhao et al., "E-Band Full Corporate-Feed 32 × 32 Slot Array Antenna with Simplified Assembly," *IEEE Antennas Wirel Propag Lett*, vol. 20, no. 4, pp. 518–522, Apr. 2021, doi: 10.1109/LAWP.2021.3055763.
[12] S. You, S. C. Ahn, Y. S. Kim, and G. Byun, "Asymmetric Iris Structures for Dual-Polarization Waveguide Slot Arrays for E-Band Wireless Backhaul Systems," *IEEE Trans Antennas Propag*, vol. 70, no. 4, pp. 2633–2644, Apr. 2022, doi: 10.1109/TAP.2021.3118729.
[13] S. G. Zhou, G. L. Huang, T. H. Chio, J. J. Yang, and G. Wei, "Design of a Wideband Dual-Polarization Full-Corporate Waveguide Feed Antenna Array," *IEEE Trans Antennas Propag*, vol. 63, no. 11, pp. 4775–4782, Nov. 2015, doi: 10.1109/TAP.2015.2479639.
[14] Y. J. Cheng, F. Y. Tan, M. M. Zhou, and Y. Fan, "Dual-Polarized Wideband Plate Array Antenna with High Polarization Isolation and Low Cross Polarization for D-Band High-Capacity Wireless Application," IEEE Antennas Wirel Propag Lett, vol. 19, no. 12, pp. 2023–2027, Dec. 2020, doi: 10.1109/LAWP.2020.3020385.
[15] Y. Liu, Y. J. Cheng, M. -H. Zhao and Y. Fan, "Dual-band shared-aperture high-efficiency reflectarray antenna based on structure-reuse technique," *IEEE Antennas Wireless Propag. Lett.*, vol. 20, no. 3, pp. 366-370, Mar. 2021.
[16] A. Gonzalez, K. Kaneko, and S. Asayama, "Recent work on (sub-) mm-wave ultra-wideband corrugated horns for radio astronomy," in *Proc. IEEE 11th Eur. Conf. Antennas Propag.*, 2017, pp. 3327–3331.
[17] Y. Beniguel, A. Berthon, C. V. Klooster and L. Costes, "Design realization and measurements of a high performance wide-band corrugated horn," *IEEE Trans. Anten. Propag.*, vol. 53, no. 11, pp. 3540-3546, Nov. 2005.
[18] I. Agnihotri and S. K. Sharma, "Design of a 3D Metal Printed Axial Corrugated Horn Antenna Covering Full Ka-Band," *IEEE Antennas Wireless Propag. Lett.*, vol. 19, no. 4, pp. 522-526, Apr. 2020.

CHAPTER 2: LITERATURE REVIEW

Hollow waveguide antennas are finding more and more applications in high microwave and millimeter-wave systems. However, current designs of such antenna systems face limitations in achieving the wide bandwidth and shared-aperture capabilities, necessary for advanced communication systems. This review examines recent advancements in various waveguide antennas, including series-fed, fully corporate-fed, dual-linearly polarized, dual-circularly-polarized, and multi-band shared-aperture dual-polarized array antennas. It discusses their strengths and challenges, with a focus on enhancing bandwidth and developing shared-aperture techniques to meet emerging and more stringent requirements. These advancements are crucial for pushing the boundaries of waveguide antenna technology in communication and radar systems. In addition, the relevant literature on subterahertz corrugated horn antenna will also be reviewed.

2.1 Planar Hollow Waveguide Array Antennas for Millimeter-Wave Applications

Planar hollow waveguide array antennas are widely used in millimeter-wave communication systems, radar, and satellite payloads, owing to their low loss, high power handling capability, and effective beam-shaping characteristics. Unlike dielectric-filled waveguide arrays, hollow waveguide arrays eliminate dielectric loss, making them highly suitable for applications where low insertion loss and high radiation efficiency are critical.

2.1.1 Series-Fed and Partially Corporate-Fed Waveguide Slot Array Antennas

Series-fed waveguide slot array antennas have gained popularity due to their high efficiency and simplicity in millimeter-wave applications [1]. However, they are inherently prone to frequency dispersion caused by the long-line effect, which results in beam squint, meaning the beam direction deviates from the array's normal as the frequency changes. This effect becomes increasingly detrimental in point-to-point communication, especially in high-gain applications where larger apertures narrow the main beam, making any squint more pronounced. To mitigate these effects, center feeding methods have been employed to reduce the effective length of the series feed line by half, subsequently enhancing the operational bandwidth [2], [3]. Another improvement, as shown in Fig. 2.1, comes from integrating small series-fed arrays with a corporate feed network. This can significantly extend the bandwidth [4]. Despite these advancements, the reported partially corporate feed waveguide slot arrays have not yet surpassed a bandwidth of 12%, far from meeting the demands of modern applications [5]. For instance, in E-band (71-86 GHz) point-to-point backhaul, it requires a 19.2% bandwidth, while high-throughput satellite terminal antennas demand even broader bandwidths, such as 30.2% for Ku-band (10.7-14.5 GHz) and 56% for Ka-band (17.7-31 GHz).

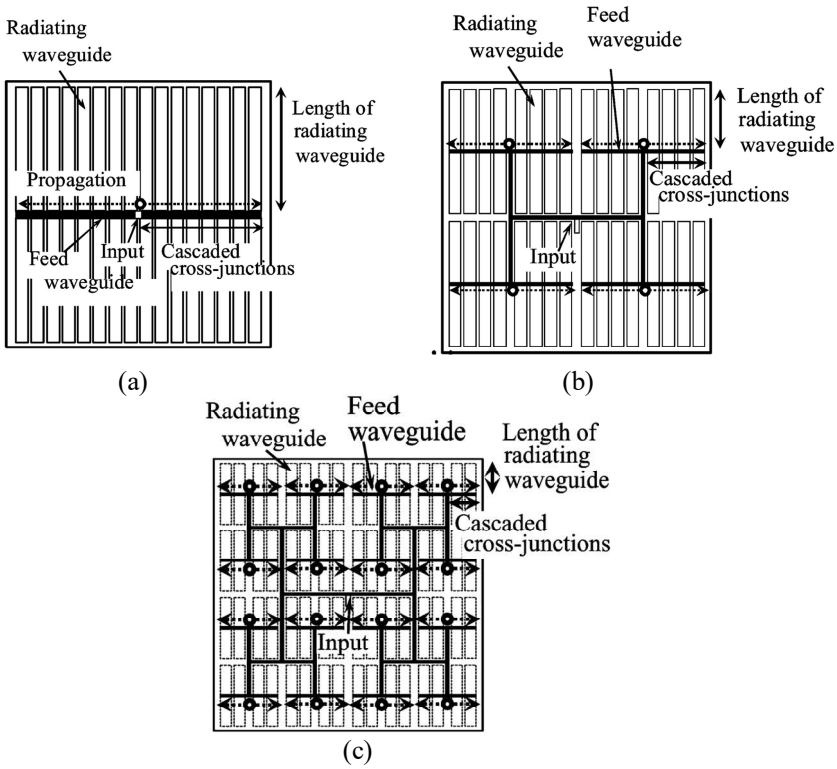


Fig. 2.1 Partially corporate feed slotted waveguide array antenna. (a) Centre-feed. (b) Partially corporate feed (divided into 4 units). (c) Partially corporate feed (divided into 16 units) [5].

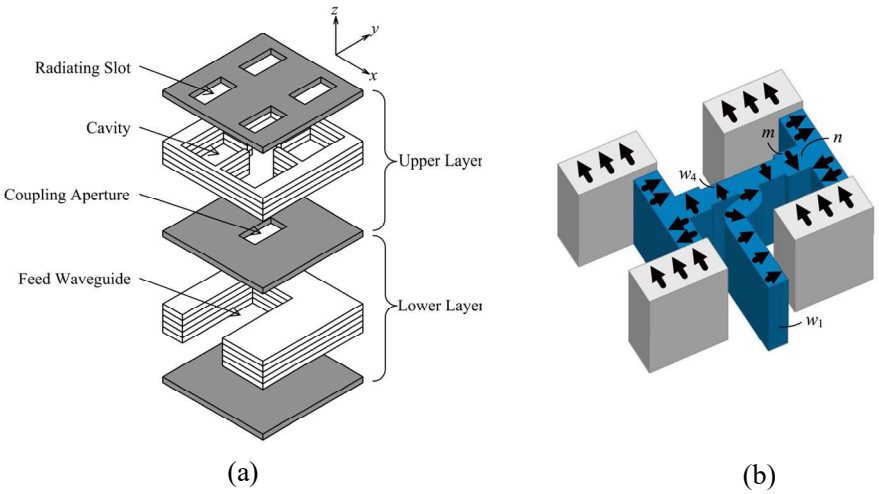


Fig. 2.2 2×2 subarray of fully corporate feed slotted waveguide array antenna, (a) using a 1-to-4 back cavity to connect the corporate feed network with the radiating slots; (b) by directly connecting each output of the corporate feed network to individual radiating slots.

2.1.2 Fully Corporate-Fed Waveguide Slot Array Antennas

Fully corporate-fed waveguide slot array antennas provide a competitive alternative to address the inherent bandwidth limitations of series-fed designs, as they eliminate beam squint caused by frequency dispersion [6], [7], [8], [9], [10], [11]. The feed network in fully corporate-fed arrays typically adopts one of two topologies. The first topology (in Fig.

2.2(a)) uses a 1-to-4 back cavity to connect the corporate feed network with the radiating slots [6]. This approach simplifies the feed network's complexity but faces challenges in achieving low sidelobes due to the uniform amplitude and phase distribution of the 2×2 subarray elements, which often results in grating lobes appearing within the 30-50° elevation range. The second topology (in Fig. 2.2(b)) directly connects each output port of the corporate feed network to individual radiating slots, offering more precise control over the amplitude and phase of each radiating element [9], [10], [11]. However, this method complicates the design, as it requires narrower waveguide channels, making fabrication more challenging. It requires advanced CNC machining techniques to maintain high dimensional accuracy.

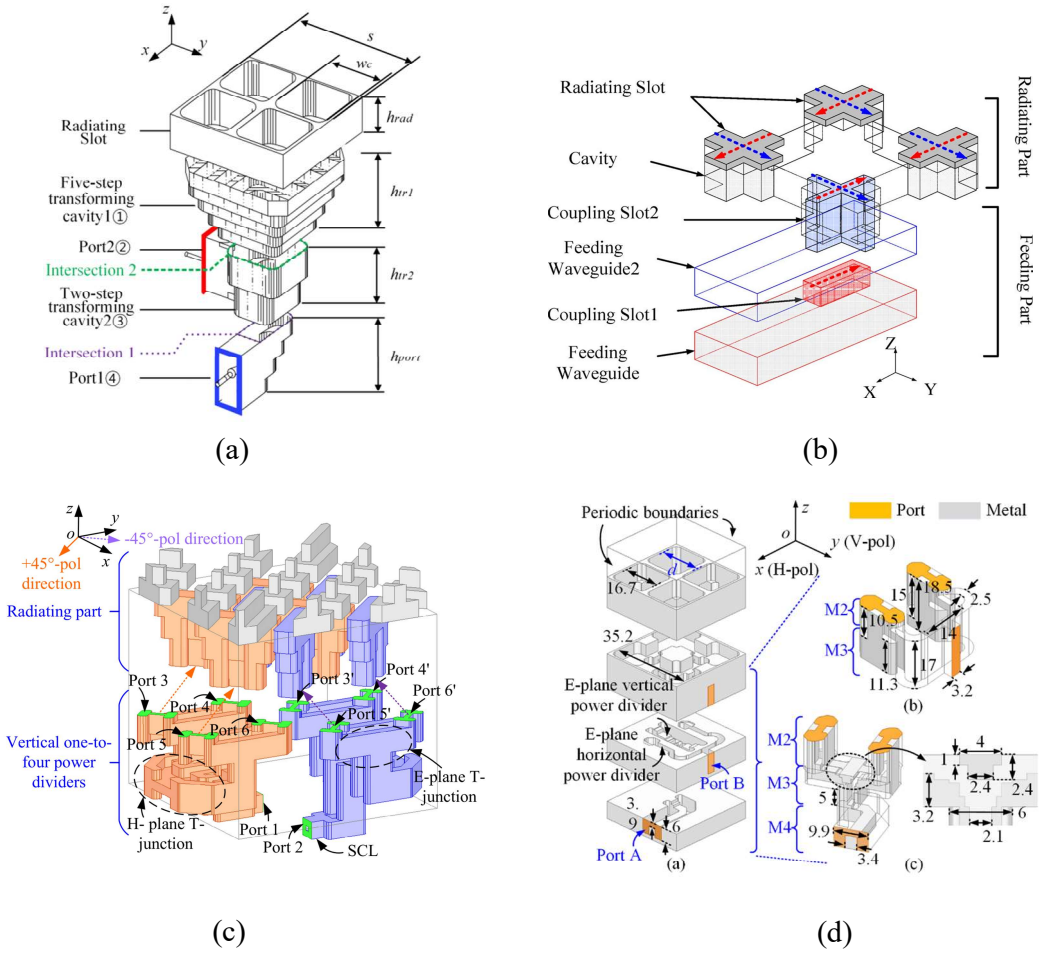


Fig. 2.3 Fully corporate feed dual-linear polarized array antenna. (a) Fed by a 'T' type OMT with a 1-to-4 back cavity [12]; (b) Fed by a cross slot with a 1-to-4 back cavity [15]; (c) Multi-port excited orthomode transducers directly exciting radiators [16]; (d) Multi-port excited orthomode transducers directly exciting radiators [17].

2.1.3 Dual-Linear Polarized Waveguide Slot Array Antennas

Dual-polarized antennas have seen widespread application in point-to-point microwave backhaul, satellite communication, and radar systems due to their capability to enhance channel capacity and enable polarization modulation. These antennas can be divided into those incorporating a 1-to-4 back cavity and those without it, as shown in Fig. 2.3. For

designs utilizing a back cavity [12], [13], [14], [15], cross-slot couplers [15] and T-type orthomode transducers (OMTs) [13] are commonly employed for generating orthogonally polarized feed. Arrays based on cross-slot coupling typically face bandwidth limitations because the slot's coupling strength restricts operational bandwidth.

The combination of T-type OMTs with multimode back cavities represents a more advanced solution, allowing for larger bandwidths [18], [19]. For example, a design proposed by [19] demonstrated a back cavity structure operating in TE320/TE230 and TE140/TE410 modes, achieving a 22.8% impedance bandwidth, marking the widest bandwidth achieved for back-cavity-based OMT-excited dual-polarized arrays to date. However, this is still insufficient for meeting the expansive bandwidth requirements of high-throughput satellite communication systems. As an alternative, multi-port excited orthomode transducers directly exciting radiators in a one-to-one configuration have emerged as a promising solution for achieving wideband performance in dual-polarized waveguide slot array antennas. This approach provides precise control over the amplitude and phase of each radiating element, allowing for improved polarization purity and isolation. By directly coupling the OMT outputs to individual radiating slots, this configuration can achieve enhanced bandwidth and better impedance matching compared to traditional feed methods [16], [17], [20]. As a result, it is particularly well-suited for applications requiring broad bandwidth and high polarization efficiency, such as high-throughput satellite communication systems [17], where over 30% impedance bandwidth was achieved. However, extending this bandwidth further remains challenging due to limitations imposed by the fundamental mode bandwidth of the radiating slots. Future advancements in this domain may involve hybrid techniques that combine the advantages of multi-port excitation with novel radiating slot designs to achieve even wider bandwidths.

2.1.4 Dual-Circularly Polarized Waveguide Slot Array Antennas

Achieving dual circular polarization (CP) in waveguide slot arrays is a critical requirement for some modern communication systems, such as satellite communication and advanced radars. There are three widely used approaches shown in Fig. 2.4: (1) Waveguide circularly polarized radiator fed by a dual linearly polarized array [21], [22], [23]; (2) Dual linearly polarized array fed by a 90° coupler [24]; and (3) Dual linearly polarized array covered with a FSS-based polarizer [25], [26], [27].

The first two configurations, although effective, are often complex, bulky, and necessitate multi-layer CNC machining, leading to manufacturing difficulties and therefore increased costs. By contrast, cascading a wideband linear polarization planar array with a linear-to-circular polarization converter (LCPC) is a more flexible solution, allowing for easier implementation in multi-band and multi-polarization systems [25]. Despite this advantage, the primary limitation lies in the bandwidth constraint imposed by the feed network and radiating elements. For instance, a study by [26] utilized a double-step double-ridged slot element, achieving a broadened bandwidth of 46.8%, but this was still limited by the radiating element. Another example [27] employed CTS elements with a single-ridged waveguide feed network, reaching a 60% bandwidth. While CTS radiating slots theoretically possess infinite bandwidth, practical limitations of the feed network often restrict their performance.

Frequency-selective surfaces (FSSs) are widely used in LCPC design, which can be divided into resonant and non-resonant types. Resonant FSSs, like those based on split slot rings, cross dipoles, and Jerusalem cross (JC) slots, generally have narrow axial ratio (AR) bandwidth and high insertion loss due to large element spacing. Non-resonant structures with sub-wavelength elements offer wider bandwidth [28], [29]. Compared to the single-band LCPCs, the dual-band LCPCs generally show narrow operation bands and high insertion loss due to the mutual coupling between the two bands [30], [31], [32], [33]. Using multi-layer non-resonant structures is an effective approach to increasing the bandwidth of dual-band LCPCs. For instance, [34] presents a K/Ka-band LCPC that consists

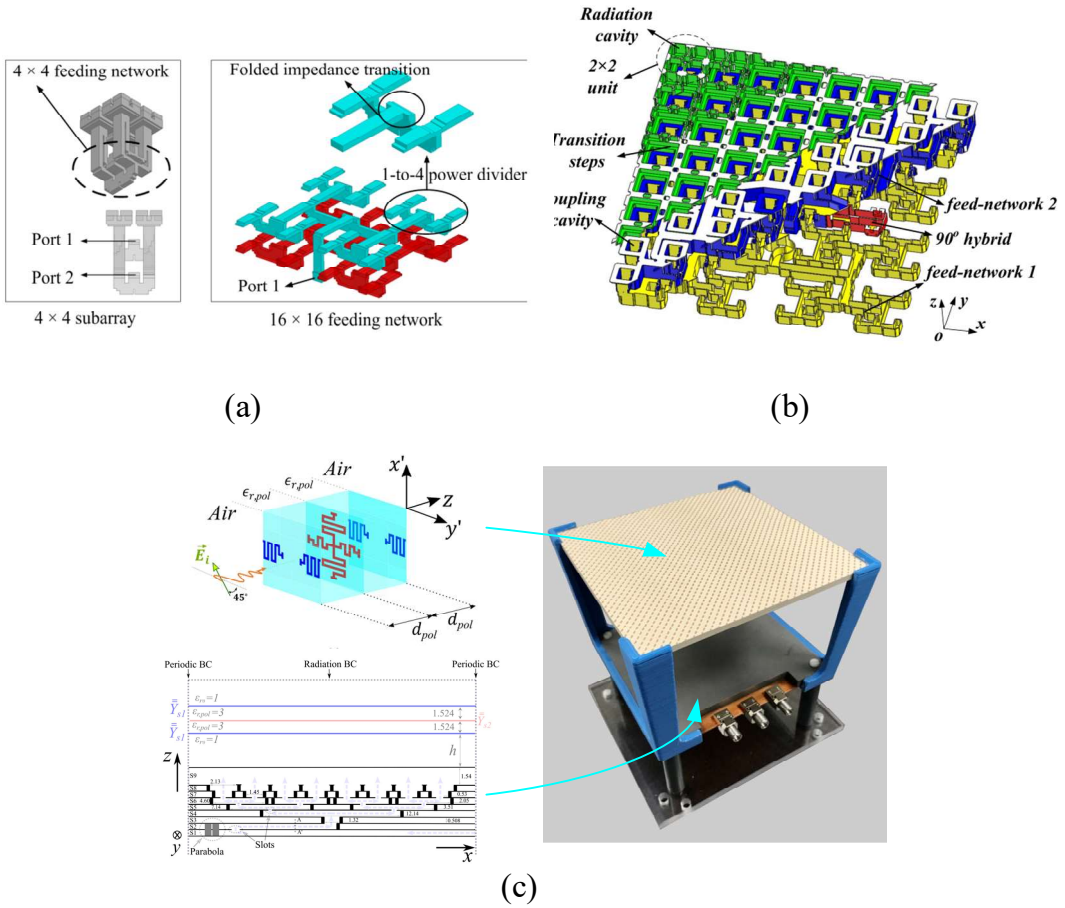


Fig. 2.4 Fully corporate feed dual-circular polarized array antenna solutions. (a) Waveguide circularly polarized radiator fed by a dual linearly polarized array [21]; (b) Dual linearly polarized array fed by a 90° coupler [24]; (c) Dual linearly polarized array covered with an FSS-based polarizer [25].

of two identical metallic layers with connected Jerusalem cross and "I"-type dipoles for each layer. The measured AR bandwidths reach 29% and 12%, with IL better than 2 dB and 0.8 dB in the K- and Ka- bands, respectively. Another study [31] proposes a systematic design of dual-band orthogonal polarization LCPCs, exhibiting an axial ratio (AR) lower than 3 dB over 18-22.2 GHz (21%) and 28.7-30.4 GHz (6%) bands, with insertion loss above 1 dB within the same bands.

In summary, the pursuit of dual circular polarization (CP) can be effectively approached through two main methods. The first involves combining a broadband dual-polarized

antenna with a 90-degree coupler, yielding dual CP but often at the expense of increased design complexity and physical size. Future advancements should aim to streamline this integration, reducing size and simplifying manufacturing without compromising performance. The second approach, incorporating a dual-band dual circular polarizer using the frequency-selective surface (FSS) structure on an ultra-wideband linearly polarized antenna, offers a more flexible solution for achieving wideband CP. Moving forward, optimizing the FSS design to enhance bandwidth, reduce insertion loss, and improve axial ratio performance will be crucial, making this method particularly suited for next-generation satellite and radar communication systems.

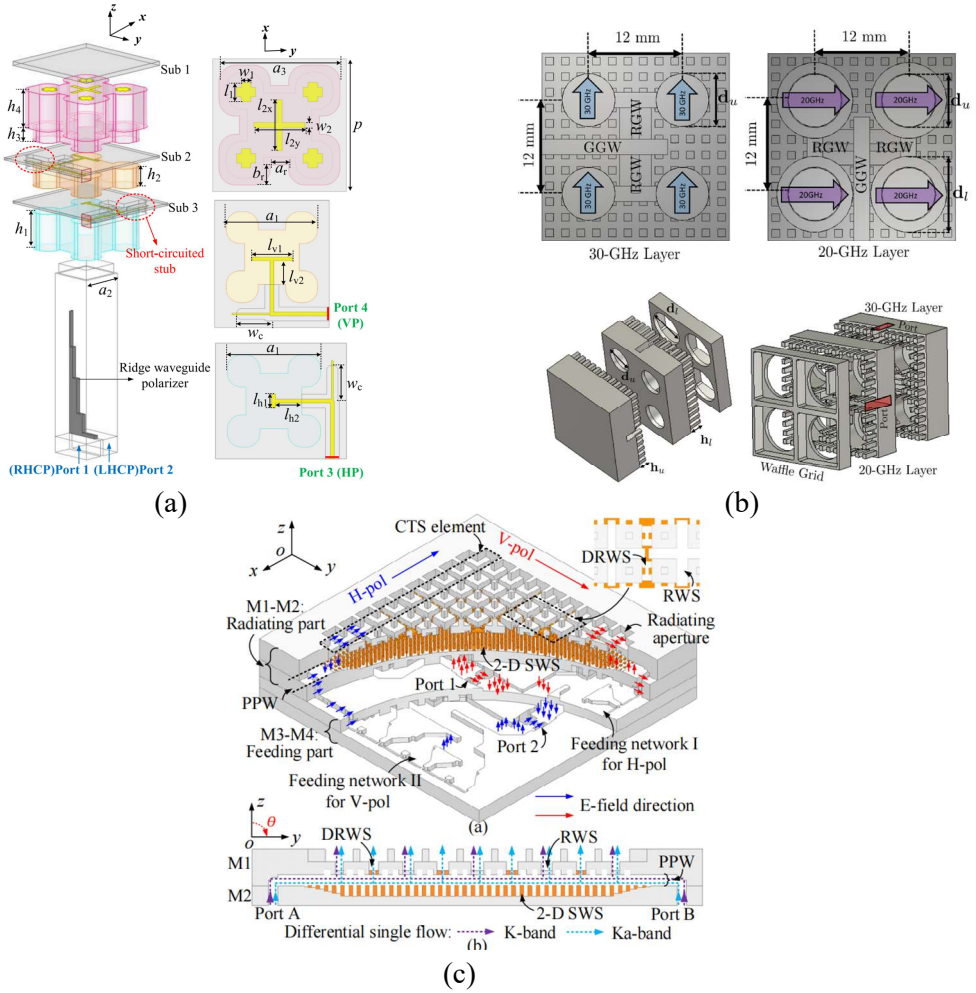


Fig. 2.5 Dual-band dual-polarized array antenna. (a) Dual-band nested dual-polarized shared-aperture antenna array [37]; (b) OMT-based orthogonal polarization shared-aperture antenna array [38]; (c) Partially shared-aperture dual-band dual-polarized antenna array [39].

2.1.5 Multi-Band Shared-Aperture Dual-Polarized Waveguide Array Antennas

Multi-band shared-aperture dual-polarized arrays have gained traction as an effective solution for integrating radiating elements across multiple frequency bands into a single

aperture [35], [36]. Based on the type of shared-aperture configuration of the radiating elements, there are three main forms as shown in Fig. 2.5:

(1) Dual-band nested dual-polarized shared-aperture antenna array: This antenna design aims to achieve dual-polarization functionality across two different frequency bands by nesting radiating elements within a shared aperture. It can support both horizontal and vertical polarizations while maintaining a compact structure, making it suitable for high-performance communication systems that require multi-band operation.

(2) OMT-based orthogonal polarization shared-aperture antenna array: This design utilizes an Orthomode Transducer (OMT) to achieve orthogonal polarization, enabling horizontal and vertical polarizations to operate at different frequencies. The OMT structure ensures high polarization isolation and efficiency, allowing the antenna to deliver dual-band orthogonal polarization within a shared aperture, ideal for systems requiring multi-band and multi-polarization capabilities.

(3) Partially shared-aperture dual-band dual-polarized antenna array: This antenna structure typically achieves partial sharing of the radiating aperture between two frequency bands while providing dual-polarization functionality. It supports both horizontal and vertical polarizations across different frequency bands, allowing for effective signal transmission. At the higher frequency, radiation occurs through all slots, whereas at the lower frequency, only alternating elements contribute to radiation. This design enhances antenna efficiency at higher frequency but degrades efficiency at the lower frequency due to the reduced effective radiating aperture. However, the partially shared aperture configuration reduces the overall physical size, making it well-suited for communication systems with stringent multi-band and dual-polarization requirements.

A significant challenge in dual-band designs is achieving flexible frequency ratios, often restricted by the inherent topological structure. For instance, in [37], the array combined Ku-band linearly polarized elements with Ka-band circularly polarized elements, resulting in a fixed frequency ratio of approximately 2:1 (14.4-17.5 GHz and 32.5-35 GHz), as shown in Fig. 2.5(a). Addressing this limitation, recent developments have introduced full-metal dual-band arrays with orthogonal polarization, such as [38] in Fig. 2.5(b), where K-band operates with horizontal polarization and Ka-band with vertical polarization. However, this approach lacks the flexibility to generate arbitrary polarization directions, constraining its use in applications requiring polarization switching and tracking.

CTS antennas in Fig. 2.5(c) stand out as a promising option for wideband, multi-band shared-aperture designs, and have been widely adopted in high-performance mmWave systems [39], [40], [41], [42], [43]. A tri-band CTS antenna reported in [40] used frequency multiplexing within the parallel-plate waveguide (PPW) feed network, achieving broad operational bandwidths for Ku-/K-/Ka-band SATCOM. Nonetheless, achieving a genuinely shared-aperture dual-polarized design with CTS antennas is more challenging. As highlighted in [41] and [42], the bandwidth of dual-polarized CTS arrays is constrained by the quasi-TEM mode of the dual-mode circular parallel-plate waveguide (CPPW) feed network, limiting bandwidth to around 11.6%. Achieving broader bandwidths would require both polarizations to operate in the TEM mode. However, developing a feed network that efficiently supports both dual-band and dual-polarized operation remains a challenge. Hybrid feed network designs show promise for expanding the operating bandwidth while maintaining dual-polarization performance.

In summary, multi-band shared-aperture dual-polarized arrays offer an effective solution for integrating elements across multiple frequency bands but face challenges with controlling the frequency ratios. Recent advancements, such as full-metal dual-band arrays with orthogonal polarization, show potential but lack flexibility for polarization tracking. CTS antennas present a promising alternative for wideband, multi-band shared-aperture applications, yet achieving true shared-aperture dual polarization remains difficult due to feed network bandwidth limitations.

2.2 Monolithic Metal 3D-Printed Corrugated Horn Antenna for Sub-Terahertz Applications

Horn antennas are widely used in millimeter-wave and terahertz systems due to their broad bandwidth, high gain, low loss, and excellent beam control capabilities. As the demand for high-frequency communication, imaging, and sensing grows, the development of sub-terahertz horn antennas (100–300 GHz) has become increasingly important [44]. These antennas serve as key components in satellite communications, radio astronomy, high-resolution radar, and wireless backhaul links, where precise beamforming and minimal XPD are required. Their ability to efficiently couple free-space radiation with guided wave modes makes them indispensable for feed systems in reflector antennas and quasi-optical networks.

Traditional horn antenna fabrication relies on precision machining and electroforming [45], [46]. This becomes challenging at sub-terahertz frequencies due to the stringent dimensional tolerances and complex corrugation structures required for optimal performance. As frequency increases, manufacturing constraints such as surface roughness, assembly misalignment, and machining precision directly impact the antenna efficiency, sidelobe performance, and XPD. Among various horn designs, corrugated horns are particularly advantageous in sub-terahertz applications due to their ability to achieve high XPD, low sidelobes, and symmetric beam patterns. However, conventional fabrication methods struggle with the fine geometrical features required for corrugations, leading to performance degradation. These challenges have motivated the exploration of metal 3D printing technologies as a viable alternative for fabricating high-performance sub-terahertz horn antennas [47]. The recent advancement of additive manufacturing technology offers a new alternative fabrication route for metal waveguide structures like horn antennas. The laser powder bed fusion (LPBF) technology typically with a manufacturing tolerance of 20 - 200 μm, cannot deliver the manufacturing precision and surface quality required for sub-millimeter features in corrugated horns above 100 GHz, where the corrugation width is usually under 200 μm. A few conical horn antennas, with no corrugation, near the G-Band were reported in [44] and [47]. In [44], a 300 GHz corrugated horn was printed using a polymer stereolithography based printer. However, the subsequent attempt to metallize the antenna failed. We have not found reports of any 3D-printed metal corrugated horns working above 50 GHz in the literature. This is because metal printers that are capable of delivering a tolerance below 10 μm and a centimeter-scale printing volume are very rare. The use of Micro Laser Sintering (MLS) based metal 3D printing was reported on different waveguide filters operating from 60 to 300 GHz [48] – [50]. In these components, MLS achieved 5-10 μm manufacture tolerance, under 2 μm surface roughness, and monolithic print with integrated waveguide flanges. This

demonstrates that Micro Laser Sintering (MLS) metal 3D printing can achieve the precision required for sub-terahertz waveguide components, making it a viable option for fabricating sub-terahertz corrugated horn antennas.

2.3 Discussion on the State-of-the-art and Research Objectives

The literature review provides a comprehensive summary of advancements in research fields relevant to this PhD project, as outlined in Table 2.1. The key findings are summarized as follows:

Waveguide slot array antennas are important antenna technologies for high-frequency applications, particularly millimeter-wave systems. However, existing designs often struggle to achieve wide bandwidth and shared-aperture capabilities. While recent developments in series-fed, fully corporate-fed, dual-polarized, and multi-band shared-aperture structures have shown progress, they still face significant limitations in bandwidth and polarization flexibility.

Series-fed and partially corporate-fed arrays work well at high frequencies but suffer from frequency dispersion, which limits their operational bandwidth. Partially corporate-fed designs can improve bandwidth but are still affected by transmission line dispersion, leading to lower efficiency. Fully corporate-fed designs mitigate beam squint issues but present challenges in achieving low sidelobes and require complex feeding networks. For fully corporate-fed single-polarized arrays, recent work has focused on radiators operating in quasi-TEM modes to alleviate bandwidth limitations caused by slot radiation. However, bandwidth remains restricted by the fundamental mode bandwidth of the transmission lines in the feed network.

For dual-polarized antennas, single-band designs attempt to enhance bandwidth by employing multimode backed cavities. However, the large element spacing introduced by the backed cavities results in grating lobes at high frequencies. Waveguide OMTs present another limiting factor for bandwidth. Meanwhile, dual-band dual-polarized antennas require even tighter element spacing, which prevents the use of fully corporate-fed topologies and leads to narrower bandwidth.

For dual circular polarization, the main implementation approaches involve integrating a 3 dB coupler or employing waveguide polarizers. These methods present significant trade-offs between complexity and bandwidth performance.

Moving forward, the primary research objectives of this thesis include developing innovative feed networks and quasi-TEM radiators to enhance bandwidth for single-polarized antennas. For dual-polarized antennas, the initial focus of the work is on mitigating gain degradation and grating lobes caused by multimode backed cavities. Further exploration aims to eliminate the backed cavity and ultimately remove the waveguide OMT to achieve an ultra-wideband design. Efforts will also be directed toward creating shared-aperture solutions to meet the stringent requirements of advanced communication systems. Overcoming these challenges will be pivotal in advancing waveguide slot array antenna technology for high-frequency point-to-point communication applications.

Planar hollow waveguide arrays face manufacturing challenges at sub-terahertz frequencies. The shrinking component size and strict fabrication tolerances make milling-based techniques impractical, requiring multi-part assemblies that lead to bulky strucutres, alignment issues, and increased ohmic losses. These limitations hinder their use in compact,

high-frequency systems, necessitating alternative solutions. Horn-fed reflector antennas offer a practical alternative, providing high gain, low loss, and simpler fabrication. Among them, corrugated horns achieve low sidelobes and high cross-polarization discrimination (XPD), making them ideal for sub-terahertz communication, radar, and sensing. However, traditional machining and electroforming struggle to meet the required precision at these frequencies. This research explores Micro Laser Sintering (MLS) metal 3D printing to fabricate monolithic, high-precision sub-terahertz corrugated horns. By leveraging MLS technology, this study aims to enhance bandwidth, improve XPD, and achieve seamless waveguide integration, establishing horn-fed reflectors as a viable alternative to planar waveguide arrays for sub-terahertz applications

2.4 Summary

This review delves into the most recent advancements in waveguide slot array antennas for high-frequency communication systems, addressing a range of configurations including series-fed, fully corporate-fed, dual-polarized, and multi-band shared-aperture designs. While these developments mark significant progress, they also underscore the persistent challenges in achieving truly wideband performance and effective shared-aperture integration. To advance this technology to the next level, especially for high-demand applications like satellite communication and radar, future research must prioritize the optimization of feed network designs and the enhancement of polarization flexibility. These efforts will be crucial in meeting the stringent performance requirements of modern communication systems operating in high-frequency domains. Additionally, at sub-terahertz frequencies, planar hollow waveguide arrays face manufacturing constraints, making horn-fed reflector antennas a practical alternative. Corrugated horns provide high gain, low sidelobes, and strong cross-polarization discrimination (XPD) but are difficult to fabricate using traditional methods. Micro Laser Sintering (MLS) metal 3D printing offers a promising solution, enabling monolithic, high-precision horn antennas. To advance this technology, future research must explore MLS-based fabrication for high-frequency applications.

Table 2.1: Review and Comparison of Single-Polarized and Dual-Polarized Waveguide Array Antennas

Ref.	Radiation element	Feeding Topology	Backed cavities	Feeding Mechanism	Frequency range	FBW (%) (S11<-10DB)	Fabrication methods	Grating lobes	Polarization	
[3]	Slots	Series-Fed	No	Hollow waveguide	25.3GHz	4	CNC	No	Single- polarization	
[4]	Slots	Partially Corporate-Fed	No	Hollow waveguide	25.3GHz	12	CNC	No		
[7]	Slots	Corporate-Fed	Single-mode	Hollow waveguide	15GHz	13.8	CNC	Yes		
[10]	Slots		No	Hollow waveguide	33Ghz	51.5	3D printing	Yes		
[26]	Ridged Slots		No	Gap waveguide	27GHz	46.8	CNC	Yes		
[27]	CTS		No	Ridge waveguide	26GHz	61.2	CNC	No		
[13]	Slots	Corporate Fed+Cross coupling OMT	Single-mode	Hollow waveguide	60GHz	10.9	Diffusion bonding	Yes	Dual- linear polarization	Dual-polarization
[15]	Slots	Corporate-Fed+T-shaped OMT	Single-mode	Hollow waveguide	13GHz	17.1	CNC	Yes		
[16]	Slots	Corporate-Fed+T-shaped OMT	Dual-mode	Hollow waveguide	13GHz	22.8	3D printing	Yes		
[19]	ME dipole	Corporate-Fed	Tri-mode	Hollow waveguide	33GHz	26.3	3D printing	Yes		
[21]	Slots	Corporate-Fed+Septum polarizer	Tri-mode	Hollow waveguide	30GHz	16	CNC	No	Dual-circular polarization	
[23]	Slots	Corporate-Fed+grooved waveguide polarizer	No	Hollow waveguide	78GHz	6.4	CNC	No		
[24]	Slots	Corporate-Fed dual-linear polarized array + 3dB coupler	Single-mode	Hollow waveguide	13.2	19	CNC	Yes		
[37]	Slots	Partially Corporate-Fed	Single-mode	Hollow waveguide and suspended stripline	16 33.7	19.4 7.4	CNC+PCB	Yes	Dual-band dual-polarization	
[43]	CTS	Series-Fed	No	PPW	18.7 29.25	13.3 5.1	CNC	No		

References

[1] T. Suzuki, J. Hirokawa, and M. Ando, "Iteration-free design of waveguide slot array with cavities," *IEEE Trans Antennas Propag*, vol. 58, no. 12, pp. 3891–3897, Dec. 2010, doi: 10.1109/TAP.2010.2078435.

[2] K. Hashimoto, J. Hirokawa, and M. Ando, "A post-wall waveguide center-feed parallel plate slot array antenna in the millimeter-wave band," *IEEE Trans Antennas Propag*, vol. 58, no. 11, pp. 3532–3538, Nov. 2010, doi: 10.1109/TAP.2010.2071356.

[3] S. Park, Y. Tsunemitsu, J. Hirokawa, and M. Ando, "Center feed single layer slotted waveguide array," *IEEE Trans Antennas Propag*, vol. 54, no. 5, pp. 1474–1480, May 2006, doi: 10.1109/TAP.2006.874310.

[4] M. Ando, Y. Tsunemitsu, M. Zhang, J. Hirokawa, and S. Fujii, "Reduction of long line effects in single-layer slotted waveguide arrays with an embedded partially corporate feed," *IEEE Trans Antennas Propag*, vol. 58, no. 7, pp. 2275–2280, Jul. 2010, doi: 10.1109/TAP.2010.2044346.

[5] H.-Y. Lee', G.-C. Kang', and B. Lee', "Cavity-Backed Planar Slot Array Antenna with a Single Waveguide-Fed Sub-array."

[6] Y. Miura, J. Hirokawa, M. Ando, Y. Shibuya, and G. Yoshida, "Double-layer full-corporate-feed hollow-waveguide slot array antenna in the 60-GHz band," *IEEE Trans Antennas Propag*, vol. 59, no. 8, pp. 2844–2851, Aug. 2011, doi: 10.1109/TAP.2011.2158784.

[7] G. L. Huang, S. G. Zhou, T. H. Chio, H. T. Hui, and T. S. Yeo, "A low profile and low sidelobe wideband slot antenna array feb by an amplitude-tapering waveguide feed-network," *IEEE Trans Antennas Propag*, vol. 63, no. 1, pp. 419–423, Jan. 2015, doi: 10.1109/TAP.2014.2365238.

[8] L. Qin, Y. Lu, Q. You, Y. Wang, J. Huang, and P. Gardner, "Millimeter-wave slotted waveguide array with unequal beamwidths and low sidelobe levels for vehicle radars and communications," *IEEE Trans Veh Technol*, vol. 67, no. 11, pp. 10574–10582, Nov. 2018, doi: 10.1109/TVT.2018.2866245.

[9] J. Y. Zhang, J. D. Zhang, and W. Wu, "Single-Layer Planar Waveguide Array Antenna With High Antenna Efficiency," *IEEE Antennas Wirel Propag Lett*, vol. 21, no. 6, pp. 1153–1157, Jun. 2022, doi: 10.1109/LAWP.2022.3159827.

[10] X. Wang, Y. Li, F. Sun, J. Wang, L. Ge, and B. Ai, "A Millimeter-Wave 51% Bandwidth High-Gain 3-D-Printed Antenna Array Based on Optimized Multistage Phase Cancellation in Feed Network," *IEEE Trans Antennas Propag*, vol. 71, no. 12, pp. 10003–10008, Dec. 2023, doi: 10.1109/TAP.2023.3314102.

[11] H. Zhao *et al.*, "E-Band Full Corporate-Feed 32 × 32 Slot Array Antenna with Simplified Assembly," *IEEE Antennas Wirel Propag Lett*, vol. 20, no. 4, pp. 518–522, Apr. 2021, doi: 10.1109/LAWP.2021.3055763.

[12] S. You, S. C. Ahn, Y. S. Kim, and G. Byun, "Asymmetric Iris Structures for Dual-Polarization Waveguide Slot Arrays for E-Band Wireless Backhaul Systems," *IEEE Trans Antennas Propag*, vol. 70, no. 4, pp. 2633–2644, Apr. 2022, doi: 10.1109/TAP.2021.3118729.

[13] D. Kim, M. Zhang, J. Hirokawa, and M. Ando, "Design and fabrication of a dual-polarization waveguide slot array antenna with high isolation and high antenna efficiency for the 60 GHz band," *IEEE Trans Antennas Propag*, vol. 62, no. 6, pp. 3019–3027, 2014, doi: 10.1109/TAP.2014.2313140.

[14] Y. J. Cheng, F. Y. Tan, M. M. Zhou, and Y. Fan, "Dual-Polarized Wideband Plate Array Antenna with High Polarization Isolation and Low Cross Polarization for D-Band High-Capacity Wireless Application," *IEEE Antennas Wirel Propag Lett*, vol. 19, no. 12, pp. 2023–2027, Dec. 2020, doi: 10.1109/LAWP.2020.3020385.
[15] S. G. Zhou, G. L. Huang, T. H. Chio, J. J. Yang, and G. Wei, "Design of a Wideband Dual-Polarization Full-Corporate Waveguide Feed Antenna Array," *IEEE Trans Antennas Propag*, vol. 63, no. 11, pp. 4775–4782, Nov. 2015, doi: 10.1109/TAP.2015.2479639.
[16] Y. Cheng and Y. Dong, "Wideband Dual-Polarized Gap Waveguide Antenna Array Based on Novel 3-D-Printed Feeding-Network Topologies," *IEEE Trans Antennas Propag*, vol. 71, no. 2, pp. 1493–1505, Feb. 2023, doi: 10.1109/TAP.2022.3217955.
[17] Q. You, Y. Lu, M. Huang, J. Xu, and J. Huang, "High-Efficiency Air-Filled Wideband ±45° Dual-Polarized Slot Array Antenna," *IEEE Trans Antennas Propag*, vol. 71, no. 5, pp. 4582–4587, May 2023, doi: 10.1109/TAP.2023.3243256.
[18] Y. Hu, Y. Lu, K. Zhou, Q. You, and J. Huang, "Wideband Hollow-Waveguide Dual-Polarized Antenna with Reduced Metal Layers," *IEEE Trans Antennas Propag*, vol. 72, no. 1, pp. 1027–1032, Jan. 2024, doi: 10.1109/TAP.2023.3313207.
[19] F. Sun *et al.*, "A Millimeter-Wave Wideband Dual-Polarized Antenna Array with 3-D-Printed Air-Filled Differential Feeding Cavities," *IEEE Trans Antennas Propag*, vol. 70, no. 2, pp. 1020–1032, Feb. 2022, doi: 10.1109/TAP.2021.3111502.
[20] N. J. G. Fonseca, "Broadband Waveguide Dual-Polarization Four-Way Power Divider for Small Passive Arrays," *IEEE Microwave and Wireless Components Letters*, vol. 31, no. 8, pp. 985–988, Aug. 2021, doi: 10.1109/LMWC.2021.3082987.
[21] J. Wu, Y. J. Cheng, H. Bin Wang, Y. C. Zhong, D. Ma, and Y. Fan, "A Wideband Dual Circularly Polarized Full-Corporate Waveguide Array Antenna Fed by Triple-Resonant Cavities," *IEEE Trans Antennas Propag*, vol. 65, no. 4, pp. 2135–2139, Apr. 2017, doi: 10.1109/TAP.2016.2631953.
[22] R. V. Gatti and R. Rossi, "A Dual-Polarization Slotted Waveguide Array Antenna with Polarization-Tracking Capability and Reduced Sidelobe Level," *IEEE Trans Antennas Propag*, vol. 64, no. 4, pp. 1567–1572, Apr. 2016, doi: 10.1109/TAP.2016.2526645.
[23] Q. Ren, A. U. Zaman, and J. Yang, "Dual-Circularly Polarized Array Antenna Based on Gap Waveguide Utilizing Double-Grooved Circular Waveguide Polarizer," *IEEE Trans Antennas Propag*, vol. 70, no. 11, pp. 10436–10444, Nov. 2022, doi: 10.1109/TAP.2022.3195458.
[24] S. G. Zhou, G. L. Huang, and T. H. Chio, "A Lightweight, Wideband, Dual-Circular-Polarized Waveguide Cavity Array Designed with Direct Metal Laser Sintering Considerations," *IEEE Trans Antennas Propag*, vol. 66, no. 2, pp. 675–682, Feb. 2018, doi: 10.1109/TAP.2017.2751644.
[25] M. Del Mastro *et al.*, "Ultra-Low-Profile Continuous Transverse Stub Array for SATCOM Applications," *IEEE Trans Antennas Propag*, vol. 70, no. 6, pp. 4459–4471, Jun. 2022, doi: 10.1109/TAP.2022.3142369.
[26] T. Zhang, R. Tang, L. Chen, S. Yang, X. Liu, and J. Yang, "Ultra-Wideband Full-Metal Planar Array Antenna with a Combination of Ridge Gap Waveguide and E-Plane Groove Gap Waveguide," *IEEE Trans Antennas Propag*, vol. 70, no. 9, pp. 8051–8058, Sep. 2022, doi: 10.1109/TAP.2022.3165655.

[27] M. Huang, Y. Lu, Q. You, J. Xu, and J. Huang, "High-Efficiency Full-Metal Planar Slot Array Antenna with Over 60% Bandwidth," *IEEE Antennas Wirel Propag Lett*, vol. 22, no. 5, pp. 1124–1128, May 2023, doi: 10.1109/LAWP.2023.3234558.
[28] M. A. Joyal and J. J. Laurin, "Analysis and design of thin circular polarizers based on meander lines," *IEEE Trans Antennas Propag*, vol. 60, no. 6, pp. 3007–3011, 2012, doi: 10.1109/TAP.2012.2194659.
[29] P. Fei, Z. Shen, X. Wen, and F. Nian, "A single-layer circular polarizer based on hybrid meander line and loop configuration," *IEEE Trans Antennas Propag*, vol. 63, no. 10, pp. 4609–4614, Oct. 2015, doi: 10.1109/TAP.2015.2462128.
[30] P. Naseri, S. A. Matos, J. R. Costa, C. A. Fernandes, and N. J. G. Fonseca, "Dual-Band Dual-Linear-to-Circular Polarization Converter in Transmission Mode Application to Band Satellite Communications," *IEEE Trans Antennas Propag*, vol. 66, no. 12, pp. 7128–7137, Dec. 2018, doi: 10.1109/TAP.2018.2874680.
[31] M. Del Mastro, M. Ettorre, and A. Grbic, "Dual-Band, Orthogonally-Polarized LP-to-CP Converter for SATCOM Applications," *IEEE Trans Antennas Propag*, vol. 68, no. 9, pp. 6764–6776, Sep. 2020, doi: 10.1109/TAP.2020.2989868.
[32] Y. Chen, G. Zhai, S. Wang, J. Gao, and J. Ren, "Dual-Band Single-Layered Linear-to-Dual-Circular Polarization Converter with High Angle Stability for Satellite Communication," *IEEE Antennas Wirel Propag Lett*, vol. 22, no. 8, pp. 2017–2021, Aug. 2023, doi: 10.1109/LAWP.2023.3271775.
[33] A. K. Fahad, C. Ruan, R. Nazir, T. U. Haq, and W. He, "Dual-Band Ultrathin Meta-Array for Polarization Conversion in Ku/Ka-Band with Broadband Transmission," *IEEE Antennas Wirel Propag Lett*, vol. 19, no. 5, pp. 856–860, May 2020, doi: 10.1109/LAWP.2020.2982281.
[34] H. Bin Wang and Y. J. Cheng, "Single-Layer Dual-Band Linear-to-Circular Polarization Converter with Wide Axial Ratio Bandwidth and Different Polarization Modes," *IEEE Trans Antennas Propag*, vol. 67, no. 6, pp. 4296–4301, Jun. 2019, doi: 10.1109/TAP.2019.2905962.
[35] M. Ferrando-Rocher, J. I. Herranz-Herruzo, A. Valero-Nogueira, and M. Baquero-Escudero, "Dual-Band Single-Layer Slot Array Antenna Fed by K/Ka-Band Dual-Mode Resonators in Gap Waveguide Technology," *IEEE Antennas Wirel Propag Lett*, vol. 20, no. 3, pp. 416–420, Mar. 2021, doi: 10.1109/LAWP.2021.3054408.
[36] Y. Dong, R. Xu, Y. H. Yang, and S. G. Zhou, "Compact Shared-Aperture Dual-Band Dual-Circularly-Polarized Waveguide Antenna Array Operating at K/Ka-Band," *IEEE Trans Antennas Propag*, vol. 71, no. 1, pp. 443–449, Jan. 2023, doi: 10.1109/TAP.2022.3213425.
[37] J. Ran, Y. Wu, C. Jin, P. Zhang, and W. Wang, "Dual-Band Multipolarized Aperture-Shared Antenna Array for Ku-/Ka-Band Satellite Communication," *IEEE Trans Antennas Propag*, vol. 71, no. 5, pp. 3882–3893, May 2023, doi: 10.1109/TAP.2023.3248445.
[38] M. Ferrando-Rocher, J. I. Herranz-Herruzo, A. Valero-Nogueira, and B. Bernardo-Clemente, "Full-Metal K-Ka Dual-Band Shared-Aperture Array Antenna Fed by Combined Ridge-Groove Gap Waveguide," *IEEE Antennas Wirel Propag Lett*, vol. 18, no. 7, pp. 1463–1467, Jul. 2019, doi: 10.1109/LAWP.2019.2919928.
[39] M. Ettorre, F. F. Manzillo, M. Casaletti, R. Sauleau, L. Le Coq, and N. Capet, "Continuous Transverse Stub Array for Ka-Band Applications," *IEEE Trans*

Antennas Propag, vol. 63, no. 11, pp. 4792–4800, Nov. 2015, doi: 10.1109/TAP.2015.2479243.

[40] Q. You, Y. Lu, Y. Wang, J. Xu, J. Huang, and W. Hong, "Hollow-Waveguide Tri-Band Shared-Aperture Full-Corporate-Feed Continuous Transverse Stub Antenna," *IEEE Trans Antennas Propag*, vol. 70, no. 8, pp. 6635–6645, Aug. 2022, doi: 10.1109/TAP.2022.3161265.

[41] M. Śmierzchalski *et al.*, "A Novel Dual-Polarized Continuous Transverse Stub Antenna Based on Corrugated Waveguides-Part I: Principle of Operation and Design," *IEEE Trans Antennas Propag*, vol. 69, no. 3, pp. 1302–1312, Mar. 2021, doi: 10.1109/TAP.2020.3028236.

[42] M. Śmierzchalski *et al.*, "A Novel Dual-Polarized Continuous Transverse Stub Antenna Based on Corrugated Waveguides-Part II: Experimental Demonstration," *IEEE Trans Antennas Propag*, vol. 69, no. 3, pp. 1313–1323, Mar. 2021, doi: 10.1109/TAP.2020.3037809.

[43] Y. Hu, Y. Lu, Q. You, K. Wang, Y. Wang and J. Huang, "K-/Ka-Band Dual-Polarized Differential Series-Fed Waveguide Slot Array Antenna With Enhanced Boresight Radiation Bandwidth," *IEEE Trans Antennas Propag*, vol. 72, no. 12, pp. 9516-9521, Dec. 2024.

[44] D. Rostyslav, A. S. Andy, E. Saleh, R. C. Jones, R. S. Donnan, C. J. Tuck, "Additive manufacturing of a terahertz back-to-back horn antenna for use in life sciences," *IEEE Trans. Compon. Packag. Manuf. Techn.*,vol. 12, no. 4, pp. 595-601, April 2022.

[45] A. Gonzalez, K. Kaneko, and S. Asayama, "Recent work on (sub-) mm-wave ultra-wideband corrugated horns for radio astronomy," in *Proc. IEEE 11th Eur. Conf. Antennas Propag.*, 2017, pp. 3327–3331.

[46] Y. Beniguel, A. Berthon, C. V. Klooster and L. Costes, "Design realization and measurements of a high performance wide-band corrugated horn," *IEEE Trans. Anten. Propag.*, vol. 53, no. 11, pp. 3540-3546, Nov. 2005.

[47] H. Kang, K. Kaneko, R. Sakai, and A. Gonzalez, "A Wideband Millimeter-Wave Corrugated Horn at 30-50 GHz Taking Advantage of All-Metal 3-D Printing Fabrication," *IEEE Antennas Wireless Propag. Lett*., vol. 22, no. 6, pp. 1446-1450, June 2023.

[48] T. Skaik, M. Salek, P. Hunyor, P. Huggard, H. Wang and P. Wilson, Y. Wang, "Evaluation of 3D Printed Monolithic G-band Waveguide Components," *IEEE Trans. Compon. Packag. Manuf. Techn*., 13(2), pp. 240-248, Feb. 2023.

[49] Y. Yu, Y. Wang, T. Skaik, T. Starke, X. Shang, M. Lancaster, P. Hunyor, P. Huggard, H. Wang, M. Harris, M. Beardsley, Q. Cheng, "D-band Waveguide Diplexer Fabricated Using Micro Laser Sintering," *IEEE Trans. Compon. Packag. Manuf. Techn*., vol. 12, no. 9, pp. 1446 – 1457, Sept. 2022.

[50] T. Skaik, Y. Wang, M. Salek, P. Hunyor, H. Wang, P. G. Huggard, T. Starke, M. Attallah and R. Martinez, "A 3D Printed 300 GHz Waveguide Cavity Filter by Micro Laser Sintering", *IEEE Trans. Terahertz Sci. Techn*., vol. 12, no. 3, pp. 274-281, May 2022.

CHAPTER 3: WIDEBAND DUAL-POLARIZED HOLLOW-WAVEGUIDE SLOT ARRAY ANTENNA

Qingchun You, Yi Wang, Mingjian Huang, Jifu Huang, Ziwei Zheng and Yunlong Lu

Yi Wang proposed, organized, and oversaw the entire study, taking the lead on the project. Qingchun You originated the design concept, conducted the theoretical modeling, analysis, simulations, carried out the experiments, interpreted the results, and drafted the manuscript. Jifu Huang, Ziwei Zheng, and Yunlong Lu offered advice and guidance throughout the project, while Mingjian Huang supported the fabrication. All authors contributed to the writing of the paper and reviewed the final manuscript.

This chapter is based on the following publication: Q. You, Y. Wang, M. Huang, J. Huang, Z. -W. Zheng and Y. Lu, "Wideband Dual-Polarized Hollow-Waveguide Slot Array Antenna," *IEEE Trans Antennas Propag*, vol. 70, no. 10, pp. 9326-9336, Oct. 2022, doi: 10.1109/TAP.2022.3184544.

Abstract

A wideband dual-polarized slot array antenna based on hollow-waveguide is presented in this paper. Its wide bandwidth and high performance are enabled by two separate feeding networks, from the side and the bottom, using square coaxial line and ridge waveguide structures, respectively. The full-corporate-feed networks excite the radiation slots in a one-to-one fashion without using backed cavities. Tight element spacing is made possible, suppressing the grating lobe and maintaining high cross polarization discrimination (XPD) across the wideband. This resolves a usual trade-off between bandwidth and grating lobe. A double-ridge rectangular waveguide cavity is devised as an orthogonal mode splitter for isolation enhancement. Several design features are used to minimize the signal path length and facilitate routing. An 8×8-element prototype in K-band is designed, fabricated, and measured. Experimental results show that the antenna has a wide bandwidth of 23.4% (from 17 – 21.5 GHz) free from grating lobes. More than 25.5 dBi peak gain, higher than 51.2 dB isolation and over 43.6 dB XPD are also obtained for the dual polarizations.

Keywords: Dual-polarization array antenna, waveguide antenna, wideband, high isolation, low cross polarization.

3.1 Introduction

With the emergence of new applications, such as the Internet of Things (IoT) and AR/VR, the demand for wireless communication capacity is rapidly increasing [1]-[3]. Wideband dual-polarized antennas are highly desired, as they can combat multipath fading by polarization diversity and improve channel capacity [4]-[7]. Microstrip lines and substrate-integrated waveguides (SIWs) have been commonly used to realize dual-polarized antennas and arrays, where most work focused on the bandwidth, isolation and cross polarization discrimination (XPD) [8]-[15]. However, these antennas are often limited in their efficiency and gain due to high dielectric loss, especially in a high microwave band. In long-distance wireless communication scenarios, wideband, high-gain and high-efficiency array antennas are required for establishing stable communication links [16]-[18]. Dual-polarized antennas implemented by using low-loss solutions become attractive. Parabolic reflectors and reflectarrays are a common choice because of their advantages of low cost and ease of manufacturing [19]-[24]. However, these types of antennas are generally bulky with a large profile, which is a major shortcoming.

As a competitive alternative, hollow-waveguide (HW) slot array antenna can offer a compact and planar formfactor with high-efficiency [25]-[28]. Some HW-based dual-polarization slot array antennas have been reported [29]-[36]. There are two feeding methods. One is based on the series (or partial series) feed structure. The two typical designs are: (i) to excite orthogonally placed continuous transverse stub array or cross-slot array in series [29]-[31], or (ii) to excite the combination of V-shaped and offset longitudinal slots with partial-series feed network [32]-[34]. The fractional bandwidth (FBW) of this type of dual-polarized antennas is relatively narrow, usually within 10%.

The other method is based on a full-corporate-feed network. There have been some recent examples with impressive performance. Cross-shaped slot, square-shaped slot or magneto-electric (ME) dipole have been used to achieve dual polarization [35]-[37]. To facilitate the layout of the feed network, 1-to-4 backed cavity has been used to excite the 2×2 sub-array in all these works. For the consideration of grating lobe suppression in the E-/H- and diagonal planes, the period between the array elements in the concerned planes should be as small as possible (preferably smaller than one free-space wavelength at the highest operation frequency). To meet this requirement, the backed cavity must be constrained to operating in the fundamental mode to reduce the cavity size. However, this adversely limits the achievable FBW to less than 20% [37]. In addition, the use of common backed cavity [35] to excite two polarizations increases the risk of cross-polarization deterioration. The FBW can be enhanced by increasing the backed cavity size as demonstrated in [37]. The FBW of 26.3% has been obtained. However, an unfavorable consequence is the significantly deteriorated grating lobe level (to about -13 dB) due to the increased space between the radiation elements.

Some efforts have been made to overcome this shortcoming by eliminating the 1-to-4 backed cavity in dual-polarized array antennas [38], [39]. However, the removal of the cavity makes the feed network more complicated, which in turn makes it more difficult to reduce the period between array elements. [39] reported an 8×8 full-corporate-feed dual-polarized slot array antenna without the backed cavities. The antenna has good radiation pattern envelope, low cross-polarization pattern and high isolation. However, due to the

size restriction of the gap ridge waveguide, the space between the adjacent slots is only reduced to about one free-space wavelength at the center frequency. Coupled with the limited bandwidth of the orthogonal mode splitter (based on a coupling slot structure), the FBW of this antenna is only about 5%. How to increase the bandwidth of HW-based dual-polarized array antennas without sacrificing their key performance remains a significant design challenge.

This work aims to tackle this challenge by applying a number of new design features: (i) A new array element structure is proposed, with a stepped square-shaped radiation slot, fed from the side and the bottom, which enables a wideband impedance matching for the dual polarizations. (ii) Double-ridge waveguide cavities are devised to function as the orthogonal mode splitter to improve the port isolation over a wide frequency band. (iii) As the key contribution of this work, two sets of wideband full-corporate-feed networks with different transmission structures (square coaxial line and ridge waveguide, respectively) are used to excite the radiation slots for the two polarizations on a one-to-one basis. This topology eliminates the 1-to-4 backed cavities in the conventional designs, overcoming the performance constraints caused by these cavities, in terms of bandwidth, grating lobes and cross polarization discrimination (XPD). With these new features, the proposed array antenna exhibits wide impedance bandwidth free from grating lobe, high antenna efficiency, high isolation and XPD. The paper is organized as follows: Section II describes the antenna configuration. Section III and IV present the analysis, design, and results followed by conclusion in Section V.

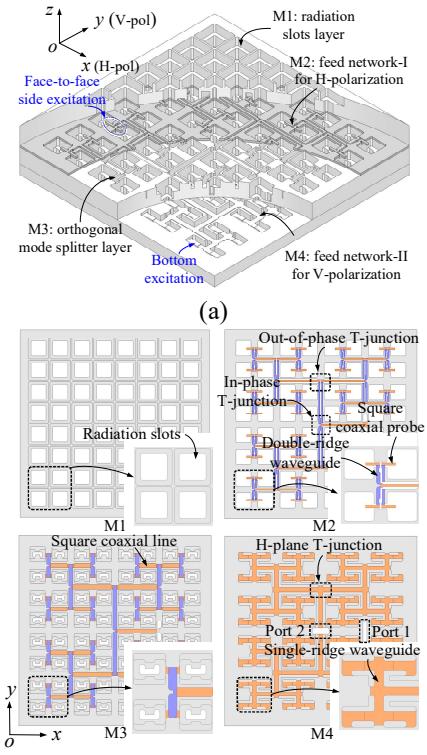


Fig. 3.1. Configuration of the dual-polarized array antenna. (a) 3-D view; (b) separated metal layers.

3.2 Antenna Configuration

Fig. 3.1(a) shows the 3D view of the proposed dual-polarized antenna array. The concerned frequency band is 17- 21.5 GHz. It is based on HW to avoid the dielectric loss. It consists of 8×8 stepped square-shaped radiation slots excited with two separate full-corporate-feed networks. The antenna array is a multilayer structure. Considering the manufacturability, it is divided into four layers. They are the radiation slot layer M1, the first full-corporate-feed network I for H-polarization (H-pol) in M2, the orthogonal mode splitter layer in M3, and the second full-corporate-feed network II for V-polarization (V-pol) in M4. The structure of each layer is shown in Fig. 3.1(b). Note that the feed network-I is a hybrid structure of double-ridge waveguides and square coaxial line, while the feed network-II is only based on the single-ridge waveguide. The 1-to-4 power divider units in the feed networks I and II are discussed in section III-B. Two standard waveguide input ports are located at the back side of the antenna for the two polarizations.

Different from the previous works in [35]-[37], 1-to-4 backed cavity layer is eliminated to avoid its drawbacks as discussed in Introduction. Instead, the radiation slots are excited by the two separate feed networks in a one-to-one correspondence. Compared with the work in [39], the spaces between adjacent elements in *x*- and *y*-directions are reduced. The FBW of the proposed antenna is broadened (See in Section III). All the simulation results are performed by using Ansoft HFSS. The detailed design and analysis of the array element, the 2×2-element sub-array and the whole antenna will be presented in the following sections.

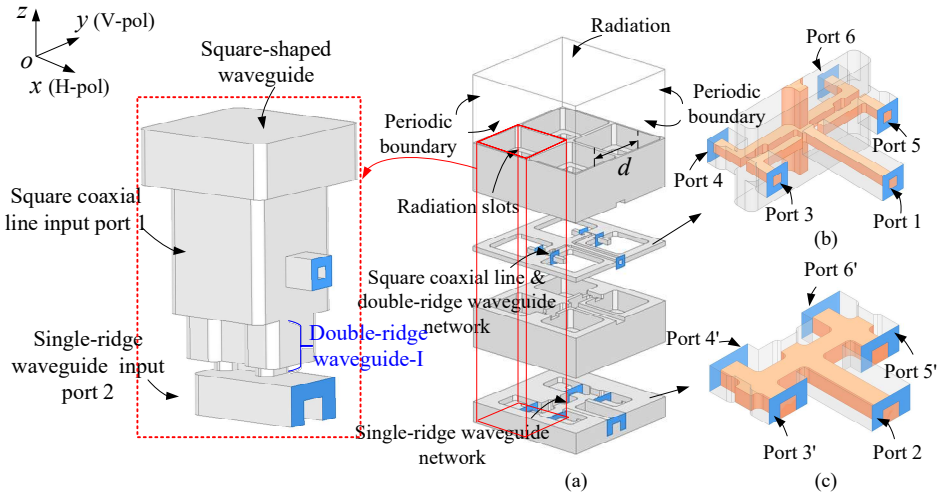


Fig. 3.2. Configuration of the 2×2 dual-polarized sub-array. (a) Whole structure and air model of the OMT ; (b) feed network for H-pol; (c) feed network for V-pol.

3.3 Analysis and Design

The configuration of the 2×2 sub-array, as well as the enlarged view of the corresponding feed networks, are shown in Fig. 3.2. Periodic boundaries are used in the simulations for considering the mutual coupling among the sub-arrays. To avoid the grating lobes in the desired frequency band, the period (*d*) between the adjacent elements along

both *x*- and *y*-directions is less than one free-space wavelength at the highest operating frequency. It is d = 13.8 mm in this design, slightly smaller than the free-space wavelength at 21.5 GHz. As aforementioned, two different feed structures (coaxial line versus waveguide) in different metal layers are employed for the two polarizations. The feed network for the H-pol excites the square-shaped slots from the side, whereas the V-pol feed network excites from the bottom layer. The details of the array element and feed network are discussed in the following section A and B. It is noted that the array element is designed and optimized in the sub-array.

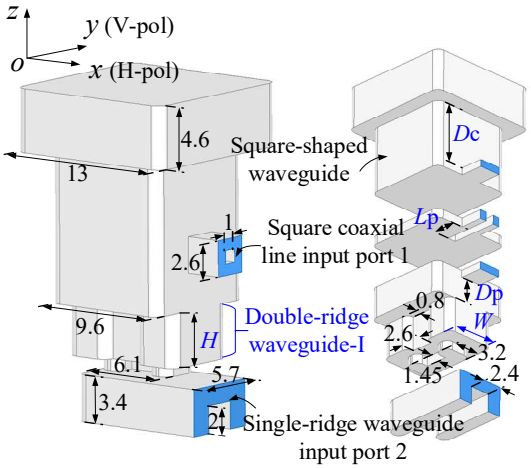


Fig. 3.3. Air model of the array element. All dimensions are given in millimeters

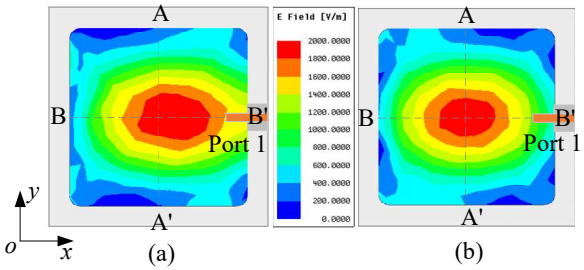


Fig. 3.4. Amplitude distribution of E-field at the radiation slots. (a) D_c= 2.6 mm; (b) D_c=6.6 mm.

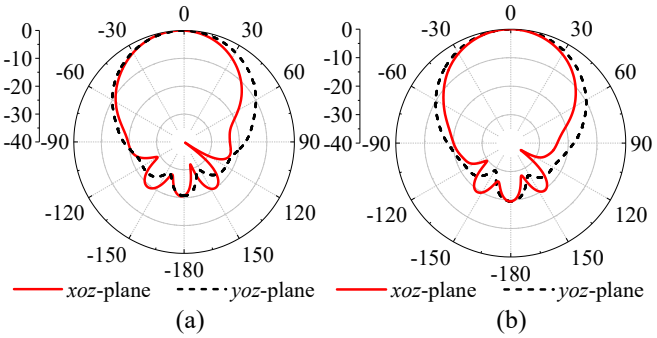


Fig. 3.5. Simulated radiation patterns of the array element with port 1 excitation at 19.5 GHz. (a) D_c= 2.6 mm; (b) D_c=6.6 mm.

3.3.1 Array Element

The array element is a stepped square-shaped radiation slot with two feeding point at the side and bottom, as shown in Fig. 3.3. The stepped square-shaped slot offers the wide

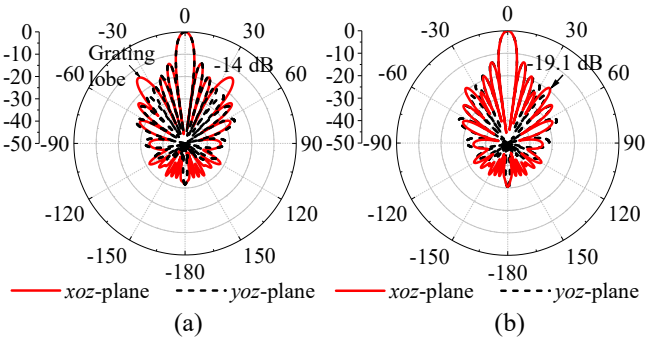


Fig. 3.6. Simulated radiation patterns of the 8×8-element array with port 1 excitation at 19.5 GHz. (a) D_c= 2.6mm; (b) D_c=6.6 mm.

bandwidth and high antenna aperture efficiency. The side-feed (port 1) is based on a square coaxial line to generate the H-pol, while allowing a compact layout of the feed network. D_c is the distance from the feeding position to the top of the smaller square slot. Fig. 3.4(a) shows the amplitude distribution of E-field with D_c = 2.6 mm. The amplitude distribution is symmetrical along the plane B-B', but asymmetrical along the plane A-A' due to the asymmetry of the side feed. The region close to the side with the port 1 has more energy. This uneven amplitude distribution would lead to asymmetry radiation patterns in *xoz*-plane as opposed to the symmetry pattern in *yoz*-plane. The simulated results at 19.5 GHz in Fig. 3.5(a) confirm this phenomenon. Furthermore, this will also cause grating lobes when an array is formed. Fig. 3.6(a) plots the synthesized radiation patterns of a 8×8-element array antenna based on this unit structure (without feed network and with port 2 terminated with 50 Ω load). The grating lobes, with a level of -14 dB, appears at θ=±36° in *xoz*-plane. An effective way to solve this asymmetry problem is to increase D_c so that only the fundamental mode is allowed to propagate while the higher order modes are attenuated. Fig. 3.4(b) shows the amplitude distribution of E-field when the D_c is increased to 6.6 mm. A more symmetric amplitude distribution can be achieved. Fig. 3.5(b) and Fig. 3.6(b) show a more symmetric radiation pattern which is then translated into lower side lobe of under -19.1 dB.

The lower feeding structure for port 2 (V-pol) is based on a single-ridge waveguide. It is transitioned into a vertical double-ridge rectangular waveguide to excite the radiation slots. It is important to note that the double-ridge waveguide-I (as shown in Fig. 3.3) not only serves as an impedance transition from the single-ridge waveguide feed network to the square waveguide of the OMT but also has a significant impact on the isolation between the V-pol and H-pol ports. The impedance matching at port 1 for the array element is realized by adjusting the length (L_p) of the probing tip of the coaxial and the position (D_p) of the feed point. Fig. 3.7 shows the simulated reflection coefficient with different values of L_p and D_p. When L_p = 2.8 mm and D_p = 2.7 mm, reflection coefficient of less than -11.5 dB is obtained from 17 GHz to 21.5 GHz. For port 2, the impedance matching is optimized by adjusting the height (H) and width (W) of the double-ridge waveguide-I. However, these two parameters also affect the isolation between ports 1 and 2. Therefore, a trade-off should be made after comprehensive consideration of both impedance matching and isolation. The parameter analysis on impedance matching and isolation is shown in Fig. 3.8. When W =

6 mm, H = 3.9 mm, the reflection coefficients is less than -13.5 dB and the isolation is better than 38.5 dB from 17 GHz to 21.5 GHz. Fig. 3.9 plots the amplitude of the E-field within the array element when ports 1 and 2 are excited at 19.5 GHz, respectively. It shows how the E-field is coupled from the input port to the radiation slot. It also shows the de-coupling between port 1 and port 2, indicating a good port isolation.

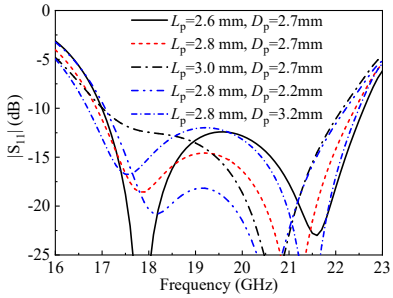


Fig. 3.7. Simulated $|S_{11}|$ of port 1 with different values of L_p and D_p.

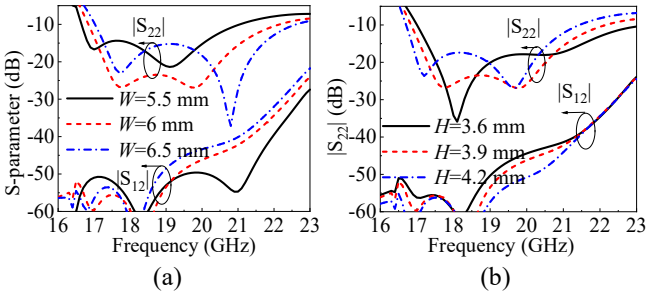


Fig. 3.8. Simulated $|S_{22}|$ of port 2 and isolations with different values of (a) W and (b) H.

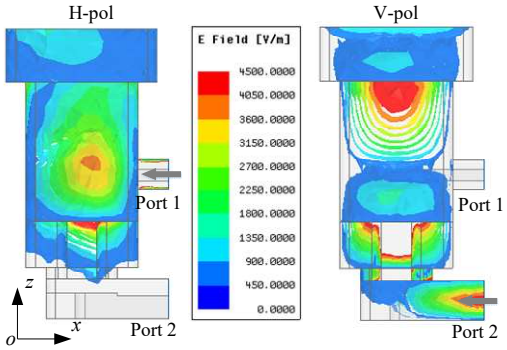


Fig. 3.9. Simulated E-field within the element when port 1 (left) and port 2 (right) is excited at 19.5 GHz.

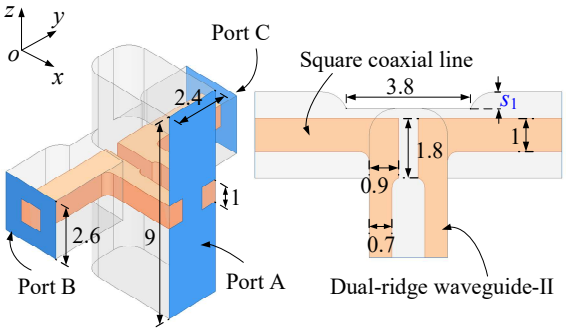


Fig. 3.10. Structure of the modified E-plane T-junction. All dimensions are given in millimeters.

3.3.2 Feed networks in Sub-array

3.3.2.1 H-pol feed network

Due to the limited distance between adjacent array elements, it is difficult to place a full-corporate feed network excited from the same side. To overcome this issue, the array elements are excited back-to-back along *x*-direction based on a hybrid structure of the double-ridge waveguide and square coaxial line, as shown in Fig. 3.2(b). However, due to this mirror excitation, there is a 180° phase difference between the two back-to-back elements. To compensate for this phase difference, instead of using a coaxial junction (even mode), an E-plane double-ridge waveguide is used at the T-junction (odd mode) without requiring extra phase shifter. This is an important design feature. An enlarged view of this junction is further shown on Fig. 3.10. At the input (Port A) is a double-ridge waveguide. The outputs (Port B and C) are coaxial. Their center conductors are tapped to the two ridges, forming a transition from one TE10 to the two coaxial TEM modes. The tapped structures also serve to support the otherwise suspended center conductor. Based on the optimized dimensions shown in Fig. 3.3, Fig. 3.10 and Fig. 3.11 plots the electromagnetic (EM) modes of all feeding waveguides, including square-shaped waveguide, single-ridge waveguide, double-ridge waveguide-I, square coaxial line in array element, and double-ridge waveguide-II in the H-pol feed network. The square-shaped waveguide has the narrowest fundamental mode bandwidth, but still well beyond the desired frequency band. The impedance matching is mainly achieved by adjusting the space between the inner and outer conductors in the coaxial branch. A parameter analysis of space S_1, defined in Fig 10, is shown in Fig. 3.12(a). $|S_{11}|$ is under -15 dB over 17-21.5 GHz, when S_1= 0.5 mm. Fig. 3.12(b) plots the simulated amplitude and phase responses of the final E-plane T-junction. The reflection coefficients for all ports are less than -15 dB, and a balanced division of -3±0.2 dB is obtained. The phase difference between the output ports is 180°±0.4°.

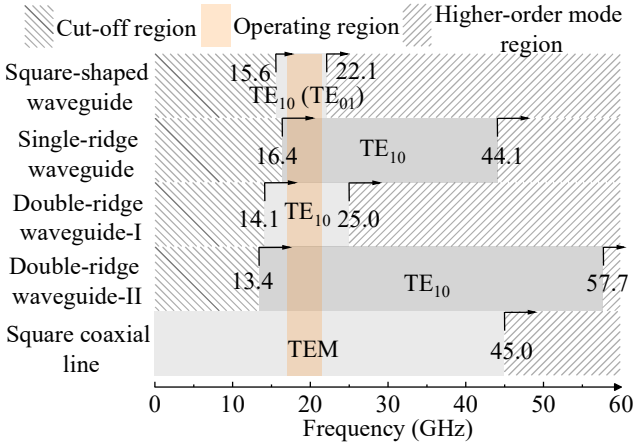


Fig. 3.11. Cut-off frequencies of all the involved transmission structures.

Next, we will look at the main junction for the 1-to-4 divider as shown in Fig. 3.14. The input is a square coaxial line, whereas the outputs are connected to the double-ridge waveguide shown in Fig. 3.11. The inner conductor of coaxial line is attached to the centre of the junction for fixing. The impedance is matched by the stepped transformer structure. Fig. 3.14(a) shows the simulated reflection coefficient with different widths (w_1), defined

in Fig. 3.13(b). An optimal impedance matching can be realized when w_1= 4.15 mm. The simulated amplitude and phase responses are plotted in Fig. 3.14(b). The reflection coefficients are all below -18 dB. The power division is -3±0.1 dB and output phase difference is ±1°.

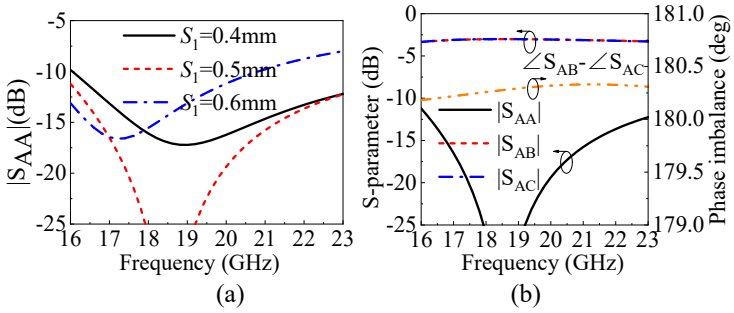


Fig. 3.12. Modified E-plane T-junctions. (a) |S11| with different values of S_1; (b) amplitude and phase responses of the final model.

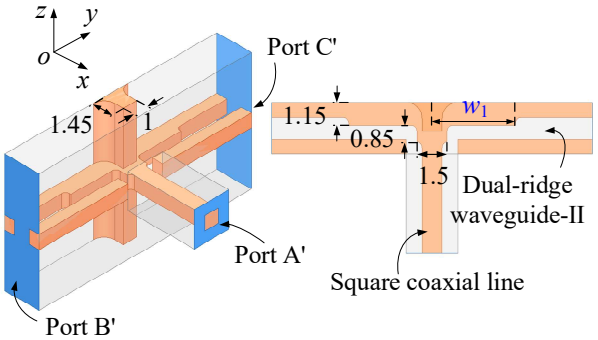


Fig. 3.13. Structure of the equal and in-phase T-junction. All dimensions are given in millimeters.

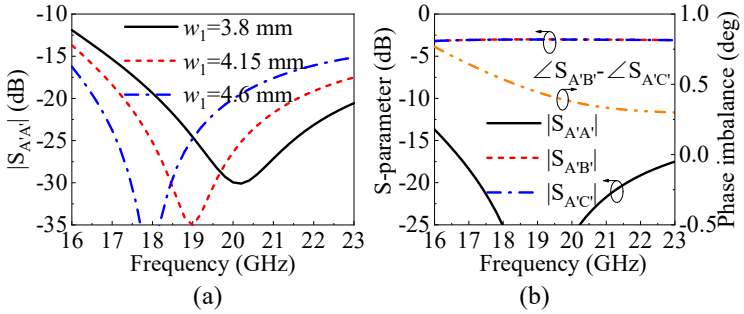
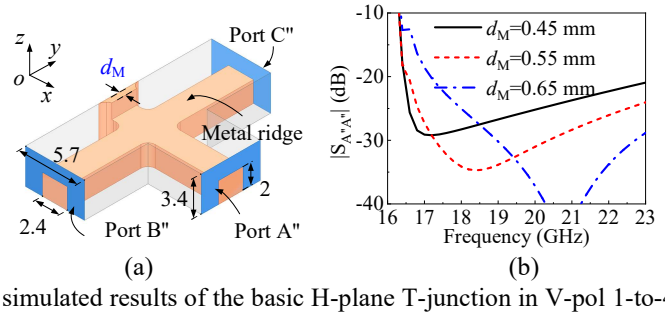


Fig. 3.14. The equal and in-phase T-junction. (a) |S11| with different values of w_1; (b) amplitude and phase responses of the final model.



(a) (b)

Fig. 3.15. Structure and simulated results of the basic H-plane T-junction in V-pol 1-to-4 power divider. (a) Structure; (b) Simulated |SA''A''| with different values of d_M. All dimensions are given in millimeters.

3.3.2.2 V-pol feed network

The V-pol 1-to-4 power divider, shown in Fig. 3.2(c) is more straightforward in design. The output ports are all equal-amplitude and in-phase. The feed network is composed of three single-ridge H-plane T-junctions. The cut-off frequencies of all the involved transmission structures are shown in Fig. 3.11. Compared with the double-ridge waveguide-II and the square coaxial line, the single-ridge waveguide has higher cut-off frequency. To minimize the size, the starting frequency of the concerned frequency band in this design is chosen to be as close to this highest cut-off frequency as possible. The basic junction is shown in Fig. 3.15(a). The impedance can be matched by adjusting the thickness (d_M) of the loaded metal plate at the center of the T-junction. Fig. 3.15(b) shows the optimal performance can be achieved when $d_M = 0.55$ mm.

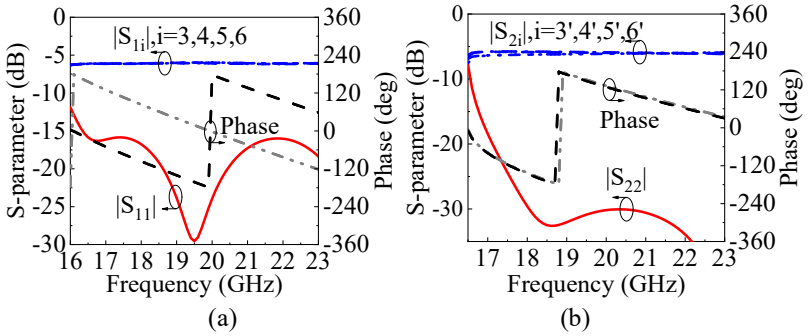


Fig. 3.16. Simulated S-parameters of (a) H- and (b) V-pol 1-to-4 power dividers.

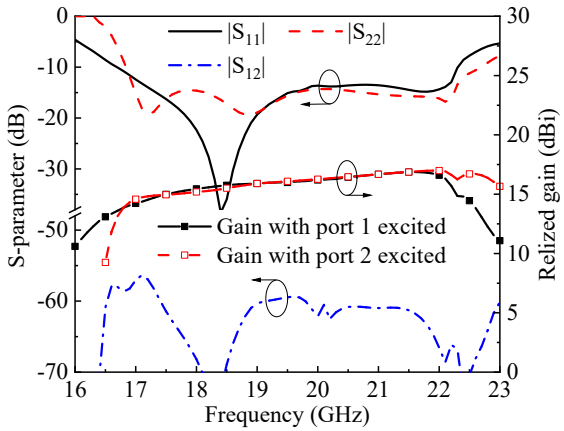


Fig. 3.17. Simulated S-parameters and peak gain of the optimized element for different polarizations.

The simulated S-parameters of the whole H- and V-pol 1-to-4 power dividers are illustrated in Fig. 3.16. Refer to Fig. 3.2 for the definition of port numbers 3(3'), 4(4'), 5(5') and 6(6'). Desired amplitude and phase distributions are achieved. Fig. 3.17 shows the simulated S-parameters and peak gains of the optimized sub-array for different polarizations. In the desired frequency range of 17- 21.5 GHz, the reflection coefficients are below -12.4 dB and the isolation is better than 55 dB. The peak gains are consistent between the two polarizations and vary from 14.2 dBi to 16.8 dBi for H-pol and V-pol, respectively. Fig. 3.18 shows the simulated radiation patterns at 17, 19.5 and 21.5 GHz.

The patterns for H-pol and V-pol match each other in the operating frequency band. They are symmetric both in *xoz*- and *yoz*-planes. The XPD of the sub-array is more than 34 dB.

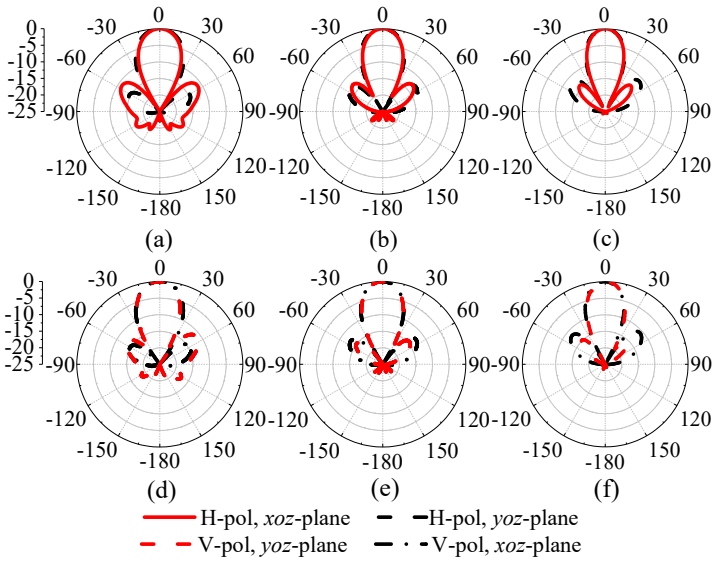


Fig. 3.18. Simulated radiation patterns of the optimized sub-array. (a) 17 GHz, H-pol; (b) 19.5 GHz, H-pol; (c) 21.5 GHz, H-pol; (d) 17 GHz, V-pol; (e) 19.5 GHz, V-pol; (f) 21.5 GHz, V-pol.

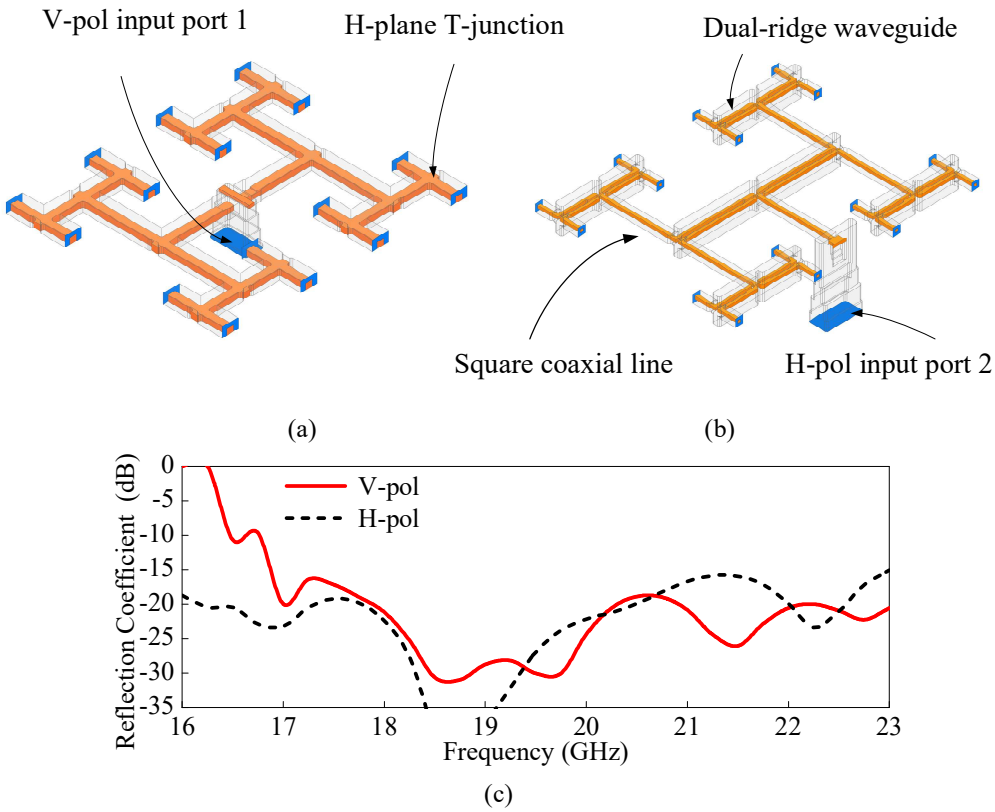


Fig. 3.19. Structure of (a) 1-to-16 feeding networks for V-pol and (b) 1-to-16 feeding networks for V-pol, and (c) Simulated reflection coefficient of both feeding networks.

3.3.2.3 Complete Array Antenna

The entire 8×8-element array antenna is composed of 16 sub-arrays. The two feed networks extend from their respective power dividers within each sub-array, as shown in Fig. 3.19(a) and Fig. 3.19(b). Fig. 3.19(c) presents the simulated results of the two polarization feed networks, where the reflection coefficients for both polarization channels remain below -18 dB. The inputs utilize standard WR-51 waveguides, necessitating transition structures to the square coaxial line for H-polarization and the single-ridge waveguide for V-polarization. These transitions are implemented using multi-stepped rectangular waveguide transformers, as illustrated in Fig. 3.20. The simulated reflection and transmission coefficients are plotted in Fig. 3.21, demonstrating good impedance matching and low insertion loss.

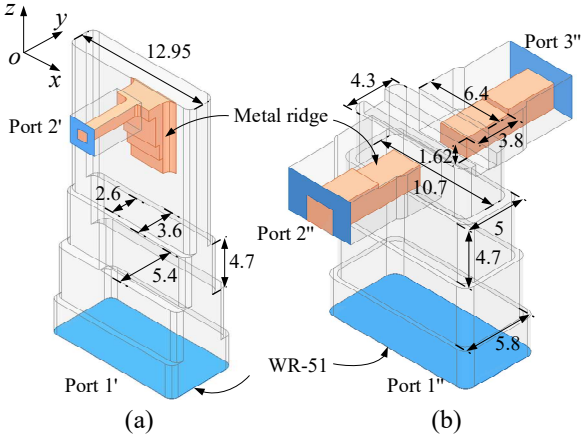


Fig. 3.20. Transition structures from standard WR-51 waveguide port to (a) square coaxial line and (b) single-ridge waveguide. All dimensions are given in millimeters.

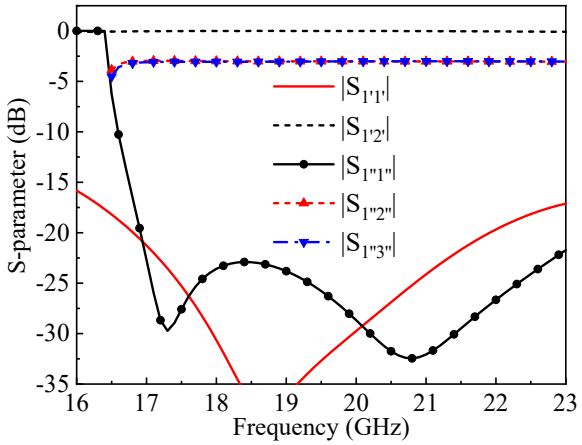


Fig. 3.21. Simulated S-parameters of the two transition structures in Fig. 3.19.

3.4 Experimental verification

The prototype is manufactured out of four metal layers, as marked out in Fig. 3.1. The blocks M1, M3 and M4 are CNC milled from aluminum-magnesium alloy with a tolerance

of 20 μm. The type of the involved aluminum-magnesium alloy is 6061, and the nominal conductivity of 3.8×10^7 S/m is used in the simulation. The thin layer M2 is cut by laser based on the same aluminum-magnesium alloy. Plenty of metal screws are installed around the feeding and radiating parts to ensure tight contact and suppress electromagnetic leakage. The separate metal blocks, the assembled dual-polarized antenna and the test environment are shown in Fig. 3.22. The prototype is 120 mm ×120 mm × 26.2 mm in size (with an aperture of 109.6 mm × 109.6 mm). The radiation measurement is conducted by using a near-field vertical planar scanner system from NSI-MI Technologies. The reflection coefficient and isolation are taken from an Agilent E8361C network analyzer.

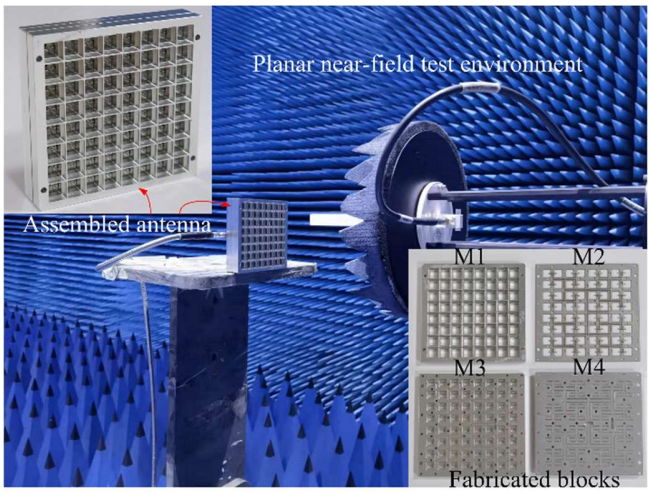


Fig. 3.22. Photographs of fabricated blocks, assembled antenna and test environment.

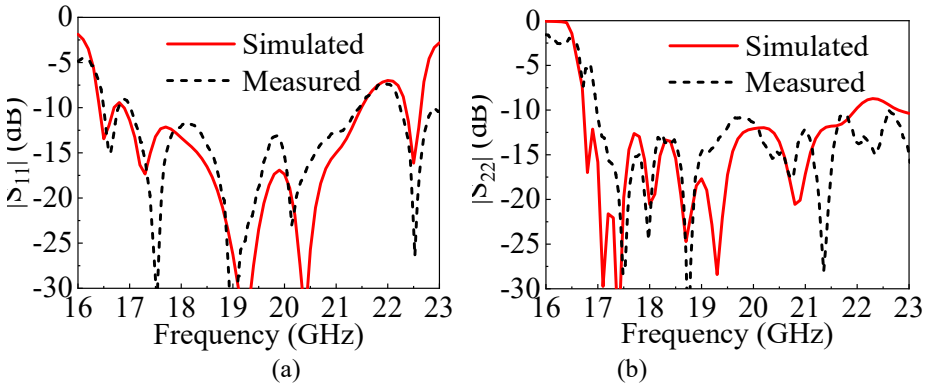
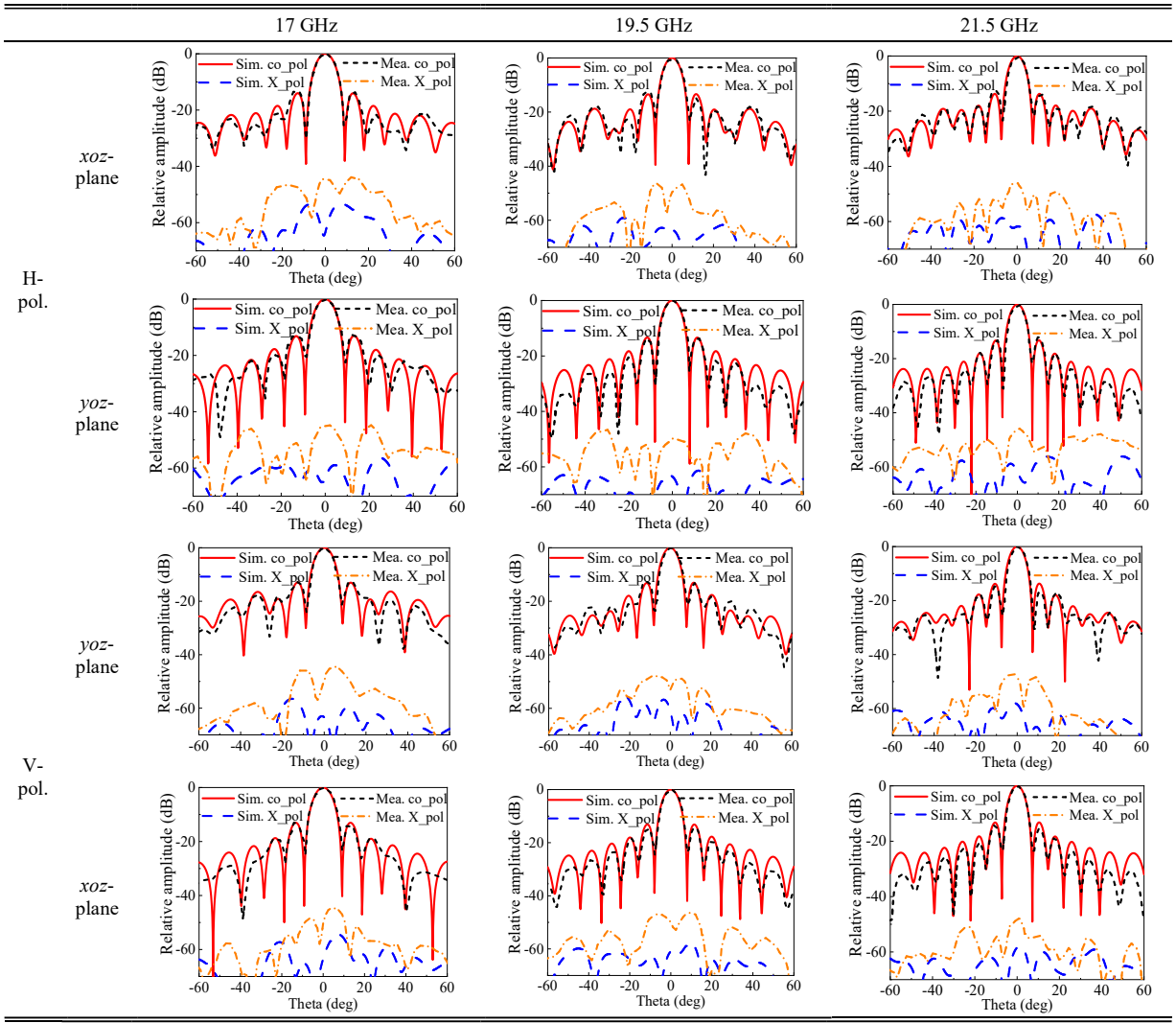


Fig. 3.23. Simulated and measured reflection coefficients. (a) H-pol; (b) V-pol.

3.4.1 Reflection Coefficient and Isolation

The simulated and measured H- and V-pol reflection coefficients are potted in Fig. 3.23(a) and (b). Good agreement has been shown. The simulated fractional bandwidth ($|S_{11}|$<-10 dB) is 24.0% (16.9 – 21.5 GHz) and 27.4% (16.7 – 22.0 GHz) for H- and V-pol, respectively. The measured FBW is 23.4% (17.0 – 21.5 GHz) for H-pol and 25.6 % (17.0 – 22.0 GHz) for V-pol. Fig. 3.24(a) shows the measured isolation is better than 51.2 dB over the desired frequency band. Fig. 3.23(b) shows the measured XPD is better than 43.6 dB.

TABLE I
NORMALIZED RADIATION PATTERNS OF THE DUAL-POLARIZED ARRAY ANTENNA



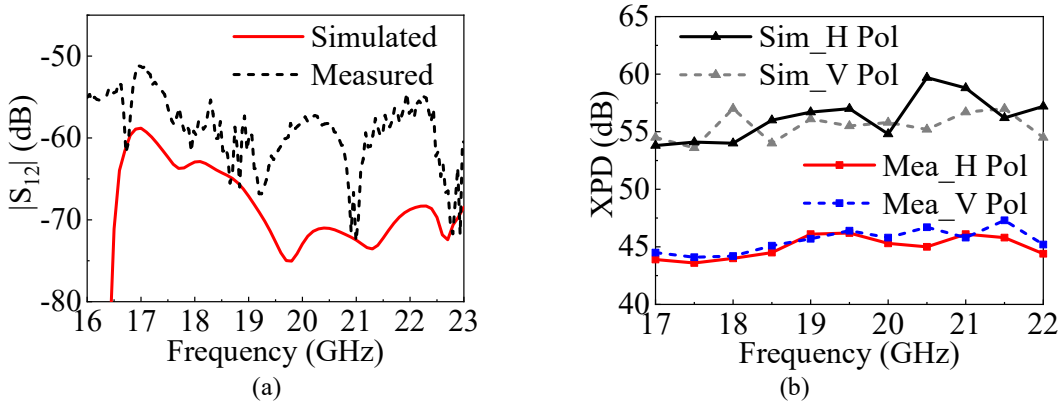


Fig. 3.24. Simulated and measured (a) port isolation and (b) XPD.

3.4.2 Radiation patterns and Efficiency

Table I shows the simulated and measured normalized radiation patterns at 17, 19.5, and 21.5 GHz. The patterns are stable across the frequency band and agree well with the simulation. The characteristics for the two polarizations are consistent. The 3-dB beamwidths in both *xoz*- and *yoz*-planes for H- and V-pol are over 6.4° from 17 GHz to 21.5 GHz. Thanks to the optimized height of the square-shaped slot (discussed in Section II-B), the measured grating lobes in *xoz*-plane for H-pol are suppressed across the same frequency range. The SLLs are around -13.1 dB, which is expected from a square array excited by constant amplitude and phase.

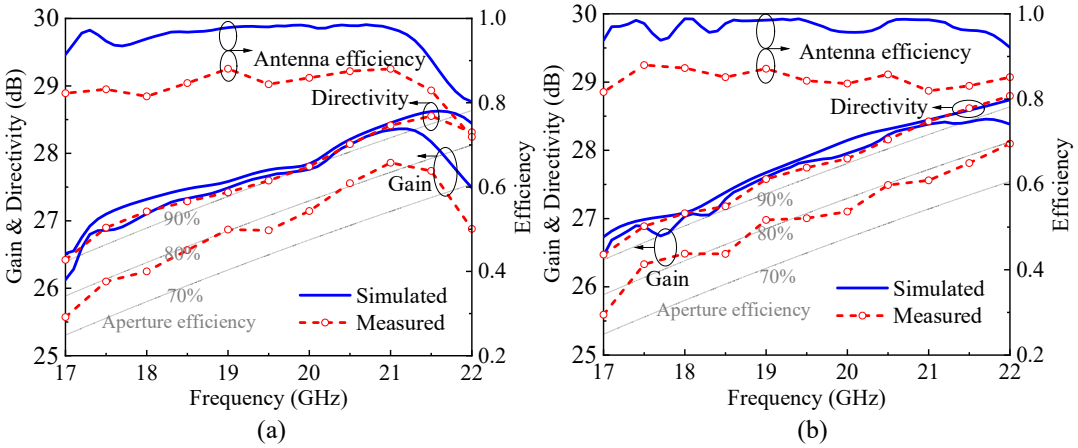


Fig. 3.25. Simulated and measured antenna peak gain and efficiency: (a) H- pol; (b)V-pol.

The simulated and measured peak gain and antenna efficiency are plotted in Fig. 3.25. The measured peak gains vary from 25.6 to 27.9 dBi and 25.5 to 27.8 dBi for H- and V-pol, while the simulated values are within the range of 26.1 - 28.4 dBi and 26.4 - 28.5 dBi. The small difference of about 0.6 dB is mainly caused by the fabrication tolerance, assembly and measurement errors. The measured directivities are 26.4 – 28.6 dBi and 26.5 – 28.8 dBi for H-pol and V-pol. The measured antenna and aperture efficiencies are better than 81.5% and 90.0% for both polarizations. The measured antenna efficiency and aperture efficiency are calculated by using the following equations:

$$\eta_{mea_an} = \frac{G_{mea}}{D_{mea}} \tag{1-1}$$

$$\eta_{mea_ap} = \frac{D_{mea}\lambda^2}{4\pi A} \tag{1-2}$$

where, η_{mea_an} is the measured antenna efficiency, η_{mea_ap} is the measured aperture efficiency, G_{mea} is the measured peak gain, D_{mea} is the measured directivity, λ is the free-space wavelength corresponding to the operating frequency, A is the aperture area of the antenna. Both the measured peak gain and directivity can be directly obtained by using a near-field vertical planar scanner system from NSI-MI Technologies.

3.4.3 Comparison

Table II compares this work with other published HW-based dual-polarized antennas. [35]-[37] employed 1-to-4 backed cavity to excite their 2×2 sub-arrays. Although [37] achieved an extended bandwidth of 26.3%, unwanted high grating lobe occurred. Only

TABLE II
PERFORMANCE COMPARISON OF HW-BASED FULL-CORPORATE-FEED DUAL-POLARIZED ANTENNAS

Ref.	Element type	Number of slots	Center frequency (GHz)/ FBW (%)	Gain (dBi)	Antenna efficiency (%)	Aperture efficiency (%)	XPD (dB)	Isolation (dB)	Aperture size (λ_0^2) [1]	Grating lobe suppression
[35]	Cross-shaped slot	16×16	62/10.9	32.2	80	90	-28	50	12.9×12.9	-20
[36]	Square-shaped slot	16×16	13.5/17.1	30.5	70	--	-28	39.5	11.3×11.3	-20
[37]	ME dipole	8×8	33.5/26.3	26.5	90	60	-30	36	8.6×8.6	-13
[39]	Circular-shaped slot	8×8	30.25/5.0	27.2	80	--	-50	50	--	--
This work	Square-shaped slot	8×8	19.25/23.4	26.8	83	90	-43.6	51.2	7.0×7.0	-18.1

[1] λ_0 is the free space wavelength at the center frequency of each passband.

16% bandwidth achieved with high level of grating lobe suppression. [39] removed the backed cavity layer and achieved a good radiation performance. However, due to relatively large space between the radiation slots, the FBW is only about 5%. With the new array topology and wideband response of the feed network, this work exhibits the largest FBW of 23.4% with grating lobe suppression. The antenna also shows stable radiation patterns, high antenna efficiency and low XPD within the frequency band.

3.5 Conclusion

In this paper, a HW-based wideband high-performance dual-polarized slot array antenna was demonstrated. Two sets of wideband full-corporate-feed networks are implemented for dual-polarization using two different structures. The upper feed network adopted a hybrid power division network of coaxial and double-ridge waveguide using both in-phase and out-of-phase T-junctions. The lower feed network, based on double-ridge waveguide structure instead, also serves as the orthogonal model splitter for isolation enhancement. This novel feeding topology facilitates the routing of the feeding network, thereby minimizing the distance between radiation slots to less than one free-space wavelength at the highest operating frequency. A prototype is implemented by using CNC milling and laser cutting. Measurement agrees well with the simulation, validating the design concept. Experimental results show that the peak gain is better than 25.5 dBi and antenna efficiency is higher than 81.5% over the frequency range of 17-21.5 GHz. The isolation and XPD are over 51.2 dB and 43.6 dB across the same frequency band. The wideband and dual-polarization make this design a good candidate for high data rate wireless applications such as satellite and 5G millimeter-wave communications.

Reference

[1] L. Chettri and R. Bera, "A comprehensive survey on internet of things (IoT) toward 5G wireless systems," *IEEE Internet Things J*, vol. 7, no. 1, pp. 16-32, Jan. 2020.

[2] A. Taha, Q. Qu, S. Alex, P. Wang, W. L. Abbott and A. Alkhateeb, "Millimeter wave MIMO-based depth maps for wireless virtual and augmented reality," *IEEE Access*, vol. 9, pp. 48341-48363, 2021.

[3] C. Deng et al., "IEEE 802.11be Wi-Fi 7: New challenges and opportunities," *IEEE Commun. Surveys Tuts.*, vol. 22, no. 4, pp. 2136–2166, 4th Quart., 2020.

[4] L. H. Ye, Y. F. Cao, X. Y. Zhang, Y. Gao and Q. Xue, "Wideband dual-polarized omnidirectional antenna array for base-station applications," *IEEE Trans. Antennas Propag.*, vol. 67, no. 10, pp. 6419-6429, Oct. 2019.

[5] Y. Liu, Z. Yue, Y. Jia, Y. Xu and Q. Xue, "Dual-band dual-circularly polarized antenna array with printed ridge gap waveguide," *IEEE Trans. Antennas Propag.*, vol. 69, no. 8, pp. 5118-5123, Aug. 2021.

[6] Y. Cai et al., "Dual-band circularly polarized transmitarray with single linearly polarized feed," *IEEE Trans. Antennas Propag.*, vol. 68, no. 6, pp. 5015-5020, Jun. 2020.

[7] L. Shen, H. Wang, W. Lotz and H. Jamali, "Compact dual polarization 4×4 MIMO multi-beam base station antennas," in *Proc. IEEE Int. Symp. Antennas Propag. USNC/URSI Nat. Radio Sci. Meeting*, 2018, pp. 1291-1292

[8] W. Sun, Y. Li, L. Chang, H. Li, X. Qin and H. Wang, "Dual-band dual-polarized microstrip antenna array using double-layer gridded patches for 5G millimeter-wave applications," *IEEE Trans. Antennas Propag.*, vol. 69, no. 10, pp. 6489-6499, Oct. 2021.

[9] A. Li and K. Luk, "Millimeter-wave dual linearly polarized endfire antenna fed by 180° hybrid coupler," *IEEE Antennas Wireless Propag. Lett.*, vol. 18, no. 7, pp. 1390-1394, Jul. 2019.

[10] C. Sim, C. Chang and J. Row, "Dual-feed dual-polarized patch antenna with low cross polarization and high isolation," *IEEE Trans. Antennas Propag.*, vol. 57, no. 10, pp. 3321-3324, Oct. 2009.

[11] P. Kumar, S. Dwari, R. K. Saini and M. K. Mandal, "Dual-band dual-sense polarization reconfigurable circularly polarized antenna," *IEEE Antennas Wireless Propag. Lett.*, vol. 18, no. 1, pp. 64-68, Jan. 2019.

[12] W. Li, X. Tang and Y. Yang, "Design and implementation of SIW cavity-backed dual-polarization antenna array with dual high-order modes," *IEEE Trans. Antennas Propag.*, vol. 67, no. 7, pp. 4889-4894, Jul. 2019.

[13] G. Srivastava and A. Mohan, "A differential dual-polarized SIW cavity-backed slot antenna," *IEEE Trans. Antennas Propag.*, vol. 67, no. 5, pp. 3450-3454, May 2019.

[14] P. Li, S. Liao, Q. Xue and S. Qu, "60 GHz dual-polarized high-gain planar aperture antenna array based on LTCC," *IEEE Trans. Antennas Propag.*, vol. 68, no. 4, pp. 2883-2894, Apr. 2020.

[15] W. Zhao, X. Li, Z. Qi and H. Zhu, "Broadband and high gain dual-polarized antenna array with shared vias feeding network for 5G applications," *IEEE Antennas Wireless Propag. Lett.*, vol. 20, no. 12, pp. 2377-2381, Dec. 2021.

[16] L. Zhang et al., “Wideband 45° linearly polarized slot array antenna based on gap waveguide technology for 5G millimeter-wave applications,” *IEEE Antennas Wireless Propag. Lett.*, vol. 20, no. 7, pp. 1259-1263, Jul. 2021.
[17] Y. You, Y. Lu, T. Skaik, Y. Wang and J. Huang, “Millimeter-wave 45° linearly polarized corporate-fed slot array antenna with low profile and reduced complexity,” *IEEE Trans. Antennas Propag.*, vol. 69, no. 9, pp. 6064-6069, Sep. 2021.
[18] M. Ferrando-Rocher, J. I. Herranz-Herruzo, A. Valero-Nogueira and B. Bernardo-Clemente, “Dual circularly polarized aperture array antenna in gap waveguide for high-efficiency Ka-band satellite communications,” *IEEE Open J. Antennas Propag.*, vol. 1, pp. 283-289, 2020.
[19] G. Mishra, S. K. Sharma, J. -C. Chieh, R. Olsen and P. Nguyen, “Ku-band dual linear polarized parabolic-cylindrical reflector antenna with beam steering performance,” in International Applied Computational Electromagnetics Society Symposium (ACES), Monterey, CA, 2020, pp. 1-2
[20] Z. Zhang, Y. Zhao, N. Liu, L. Ji, S. Zuo and G. Fu, “Design of a dual-beam dual-polarized offset parabolic reflector antenna,” *IEEE Trans. Antennas Propag.*, vol. 67, no. 2, pp. 712-718, Feb. 2019.
[21] S. Mener, R. Gillard, R. Sauleau, A. Bellion and P. Potier, “Dual circularly polarized reflectarray with independent control of polarizations,” *IEEE Trans. Antennas Propag.*, vol. 63, no. 4, pp. 1877-1881, Apr. 2015.
[22] C. S. Geaney, M. Hosseini and S. V. Hum, “Reflectarray antennas for independent dual linear and circular polarization control,” *IEEE Trans. Antennas Propag.*, vol. 67, no. 9, pp. 5908-5918, Sep. 2019.
[23] J. Yin, Q. Lou, H. Wang, Z. N. Chen and W. Hong, “Broadband dual-polarized single-layer reflectarray antenna with independently controllable 1-bit dual beams,” *IEEE Trans. Antennas Propag.*, vol. 69, no. 6, pp. 3294-3302, June 2021.
[24] D. R. Prado, M. Arrebola, M. R. Pino and G. Goussetis, “Contoured-beam dual-band dual-linear polarized reflectarray design using a multiobjective multistage optimization,” *IEEE Trans. Antennas Propag.*, vol. 68, no. 11, pp. 7682-7687, Nov. 2020.
[25] M. Akbari, A. Farahbakhsh and A. Sebak, “Ridge gap waveguide multilevel sequential feeding network for high-gain circularly polarized array antenna,” *IEEE Trans. Antennas Propag.*, vol. 67, no. 1, pp. 251-259, Jan. 2019.
[26] M. Akbari et al., “Highly efficient 30 GHz 2x2 beamformer based on rectangular air-filled coaxial line,” *IEEE Trans. Antennas Propag.*, vol. 68, no. 7, pp. 5236-5246, July 2020.
[27] M. Farahani, M. Akbari, M. Nedil, A. -R. Sebak and T. A. Denidni, “Millimeter-wave dual left/right-hand circularly polarized beamforming network,” *IEEE Trans. Antennas Propag.*, vol. 68, no. 8, pp. 6118-6127, Aug. 2020.
[28] M. Sano, J. Hirokawa and M. Ando, “Single-layer corporate-feed slot array in the 60-GHz band using hollow rectangular coaxial lines,” *IEEE Trans. Antennas Propag.*, vol. 62, no. 10, pp. 5068-5076, Oct. 2014.
[29] T. Lou, X. Yang, H. Qiu, Z. Yin and S. Gao, “Compact dual-polarized continuous transverse stub array with 2-D beam scanning,” *IEEE Trans. Antennas Propag.*, vol. 67, no. 5, pp. 3000-3010, May 2019.

[30] M. Śmierzchalski et al., “A novel dual-polarized continuous transverse stub antenna based on corrugated waveguides—part II: experimental demonstration,” *IEEE Trans. Antennas Propag.*, vol. 69, no. 3, pp. 1313-1323, Mar. 2021.
[31] X. Lu, H. Zhang, S. Gu, H. Liu, X. Wang and W. Lu, “A dual-polarized cross-slot antenna array on a parallel-plate waveguide with compact structure and high efficiency,” *EEE Antennas Wireless Propag. Lett.*, vol. 17, no. 1, pp. 8-11, Jan. 2018.
[32] Y. Chen and R. G. Vaughan, “Dual-polarized L-band and single-polarized X-band shared-aperture SAR array,” *IEEE Trans. Antennas Propag.*, vol. 66, no. 7, pp. 3391-3400, Jul. 2018.
[33] J. Lu et al., “Broadband dual-polarized waveguide slot filtenna array with low cross polarization and high efficiency,” *IEEE Trans. Antennas Propag.*, vol. 67, no. 1, pp. 151-159, Jan. 2019.
[34] M. Chen, X. -C. Fang, W. Wang, H. -T. Zhang and G. -L. Huang, “Dual-band dual-polarized waveguide slot antenna for SAR applications,” *IEEE Antennas Wireless Propag. Lett.*, vol. 19, no. 10, pp. 1719-1723, Oct. 2020.
[35] D. Kim, M. Zhang, J. Hirokawa and M. Ando, “Design and fabrication of a dual-polarization waveguide slot array antenna with high isolation and high antenna efficiency for the 60 GHz band,” *IEEE Trans. Antennas Propag.*, vol. 62, no. 6, pp. 3019-3027, Jun. 2014.
[36] S. Zhou, G. Huang, T. Chio, J. Yang and G. Wei, “Design of a wideband dual-polarization full-corporate waveguide feed antenna array,” *IEEE Trans. Antennas Propag.*, vol. 63, no. 11, pp. 4775-4782, Nov. 2015.
[37] F. Sun et al., “A millimeter-wave wideband dual-polarized antenna array with 3-D-printed air-filled differential feeding cavities,” *IEEE Trans. Antennas Propag.*, vol. 70, no. 2, pp. 1020-1032, Feb. 2022.
[38] I. Nistal-González et al., “Planar phased array antenna for nomadic satellite communication in Ka-band,” in *Proc. 11th Eur. Radar Conf.*, Oct. 2014, pp. 396–399.
[39] M. Ferrando-Rocher, J. I. Herranz-Herruzo, A. Valero-Nogueira, B. Bernardo-Clemente, A. U. Zaman and J. Yang, “8×8 Ka-band dual-polarized array antenna based on gap waveguide technology,” *IEEE Trans. Antennas Propag.*, vol. 67, no. 7, pp. 4579-4588, Jul. 2019.

CHAPTER 4: 3D-PRINTED WIDEBAND DUAL-POLARIZED HOLLOW-WAVEGUIDE ANTENNA ARRAY WITH DUAL-MODE BACK CAVITY

Qingchun You, Lu Qian and Yi Wang

Yi Wang proposed, organized, and oversaw the entire study, taking the lead on the project. Qingchun You originated the design, conducted the modelling, analysis, simulations, carried out the experiments, interpreted the results, and drafted the manuscript. Lu Qian offered advice throughout the project. All authors contributed to the writing of the paper and reviewed the final manuscript.

This chapter is based on the following paper which is under revise after major revision: Q. You, L. Qian and Y. Wang, "3D-Printed Wideband Dual-Polarized Hollow-Waveguide Antenna Array with Dual-Mode Back Cavity," *IEEE Trans Antennas Propag*, Submit in August. 2024, Under revise, after major revision.

Abstract

This paper presents a novel wideband dual-polarized hollow-waveguide antenna array, designed for manufacturing using stereolithography (SLA) 3D printing technology and metallized by copper plating. By replacing the conventional single-mode back cavity with a dual-mode (TE120/TE210 and TE140/TE410 modes) back cavity, a wider radiation bandwidth is achieved. A diamond-shaped radiation slot was employed to enhance the stability of the radiation pattern and mitigate gain drop-off at higher frequencies. Two different types of feeding networks were used for the two polarizations. For the vertical polarization, a novel, highly compact differential feed network was devised under severe space constraint while allowing the ease of printing and plating. The fabricated antenna array prototype achieves an impedance bandwidth of 30.2% (10.7-14.5 GHz), with measurements confirming high aperture efficiency (AE > 72%) and high port isolation (>48 dB). Detailed design principles, manufacturing processes, and measurements are presented, demonstrating a compact, lightweight, and high-performance antenna array using a new and alternative manufacture technology

Keywords: Wideband antenna array, dual-polarized antenna array, waveguide slot antenna, 3D printed antenna.

4.1 Introduction

Dual-polarized antennas (DPAs) are extensively used in modern wireless systems to enhance channel capacity and improve communication reliability [1], [2], [3]. In satellite communications, dual polarization has been used to synthesize arbitrary linear polarization, crucial for maintaining reliable tracking during movement [4], [5]. A key technical specification for the DPA is its effective radiating bandwidth as it is highly related to the communication capacity. For instance, high-throughput satellites typically operate in the Ku or Ka bands. The Ku band includes a receive band from 10.7 to 12.75 GHz and a transmit band from 13.75 to 14.5 GHz, covering a total span of 10.7–14.5 GHz with a fractional bandwidth of 30.2%. The Ka band is split between a receive band from 17.7 to 21.2 GHz and a transmit band from 27.5 to 31 GHz, resulting in an overall span of 17.7–31 GHz and a bandwidth of 53% [6].

DPAs have been realized using various technologies, from air-filled waveguides [7], [8], [9] microstrip lines [10], [11], [12] to substrate-integrated waveguides (SIW) [13], [14], [15]. Dielectric loss is often a concern as it increases antenna noise temperature, which negatively impacts the signal-to-noise ratio (SNR) of the receiving system. Air-filled hollow waveguide dual-polarized array antennas offer low-loss transmission, leading to higher gain and improved SNR [16], [17], [18], [19], [20], [21]. However, such hollow waveguide antennas come with certain implementation challenges, especially in their manufacture and assembly. They often need high-precision CNC machining to achieve intricate and accurate geometries, which increases the cost and accumulates assembly errors.

Recently, the rapid development of 3D printing technology has opened new opportunities for the manufacture of air-filled waveguide arrays [22]. Printing complex structures in one piece not only reduces the assembly need but also mitigates the leakage from contact interfaces. Direct Metal Laser Sintering (DMLS) [22], [23], [24] and stereolithography (SLA) [25], [26], [27] are two mainstream 3D printing techniques that have been utilized in manufacturing waveguide devices. SLA technology, using polymer materials, typically offers higher dimensional accuracy, lower surface roughness and lighter weight [25], which is highly desired for portable stations for SATCOM. However, metal plating on the inner surfaces of multi-layer complex arrays is non-trivial. This difficulty is exacerbated in broadband array antennas, because they usually use single-ridge waveguides or waveguide-coaxial as the feed networks. It would be hugely beneficial for the 3D printing process if the feed network structure can be simplified preferably with rectangular waveguide as the main transmission media.

Air-filled waveguide slot array antennas typically employ a 1-to-4 back cavity structure to avoid grating lobes. To optimize the performance, these antennas feature radiation slots in various shapes - cross [20], square [19], or circle [28]. Generally, dual-polarized slot antennas with single-mode back cavity have achieved limited bandwidths of no more than 19% [29]. Recent innovations have shown various improvements. A dual-mode back cavity structure operating in TE320/TE230 and TE140/TE410 modes achieves a 22.8% impedance bandwidth [25]. However, the design faced challenges in space constraints requiring non-uniform periodic arrangements, which results in elevated sidelobe levels of -10 dB. The antenna structure is too complex for monolithic 3D printing. It had to be printed in three-piece parts, plated separately before assembly. Building on these advancements, [24] proposed a tri-mode back cavity antenna operating in TE210/TE120,

TE320/TE230, and TE410/TE140 modes, further increasing the bandwidth to 26.3%. This antenna was monolithically printed using the DMLS process. However, this design faced

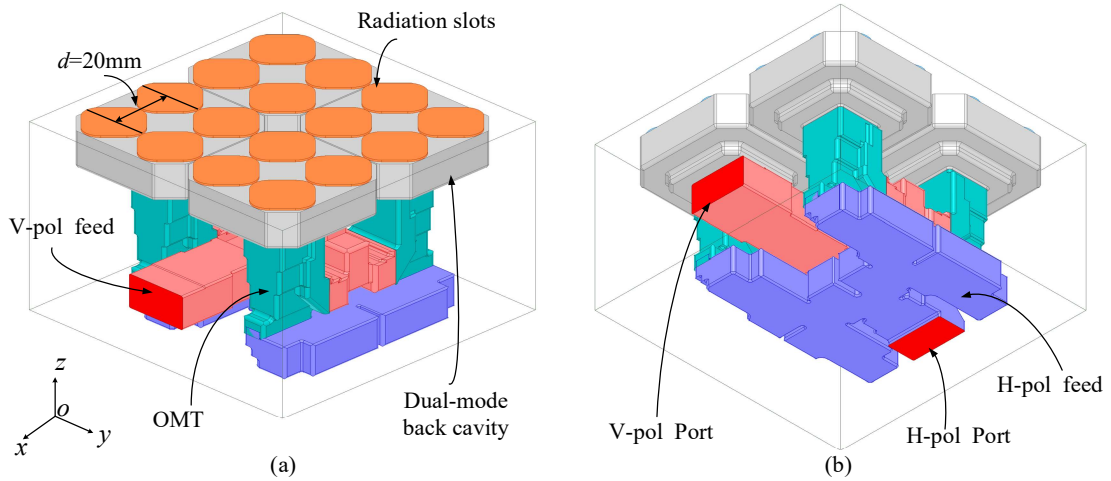


Fig. 4.1. Configuration of the proposed 3D-printed DPA. (a) View from the radiator side; (b) View from the feed side. For clarity, the antenna array is shown as an air model, and different parts are rendered in different colors.

its own set of challenges. The wavelength of the TE410 mode was smaller than the element period, leading to significant grating lobes at high frequencies. So far, only very few hollow-waveguide dual-polarized antennas can meet the whole Ku-band bandwidth requirements (10.7-14.5 GHz, 30.2%) [9], [16], [30]. They typically use complex feed networks, such as single-ridge waveguides or waveguide-coaxial networks, which poses significant challenges to metal coating after 3D printing. This highlights the intricate balance between design complexity and functional efficiency. The exploration of new fabrication approaches, such as SLA and DMLS, and the use of innovative and, importantly, simplified feed network and multi-mode back cavity designs are essential steps toward overcoming the current limitations and achieving broader bandwidths in dual-polarized antennas.

This paper presents a 3D-printed wideband dual-polarized hollow waveguide antenna array. An innovative dual-mode back cavity operating in TE120/TE210 and TE140/TE410 modes is proposed to address high sidelobe level issues and further increase the radiation bandwidth. A diamond-shaped radiation slot is introduced to replace traditional square and circular slots, effectively improving cross-polarization isolation and reducing high-frequency gain drop-off. The feed network is entirely based on E- and H-plane rectangular waveguides, designed to facilitate not only printing using SLA technology but also the subsequent copper plating. This antenna is lightweight and achieves full Ku-band impedance bandwidth in a compact form, with measurements confirming its high efficiency and stable radiation pattern.

Section II will detail the design principles of the 2×2 sub-array. Section III describes the proposed waveguide differential feed network for the horizontal polarization and the in-phase feed network for the vertical polarization. Section IV describes the manufacturing process, measurements, and related discussions of the dual-polarized antenna array. Finally, Section V concludes the paper.

4.2 Design and Analysis

Fig. 4.1 illustrates the configuration of the proposed Ku-band DPA array in its air model. The antenna operates over 10.7 to 14.5 GHz, a spectrum commonly utilized in satellite communications and radar systems. The array consists of four sub-arrays and two layers of feed networks. Each sub-array is primarily constructed of four diamond-shaped radiation slots, a dual-mode back cavity, and a side-coupled waveguide orthomode transducer (OMT). The thickness of the radiation slot layer is 0.5 mm, optimized to achieve a low radiation quality factor Q_{rad}. This is crucial for meeting the targeted wide radiation bandwidth [31]. Two different feed networks are employed for the vertical and horizontal polarization, respectively. The detailed design and analysis of each component will be presented next.

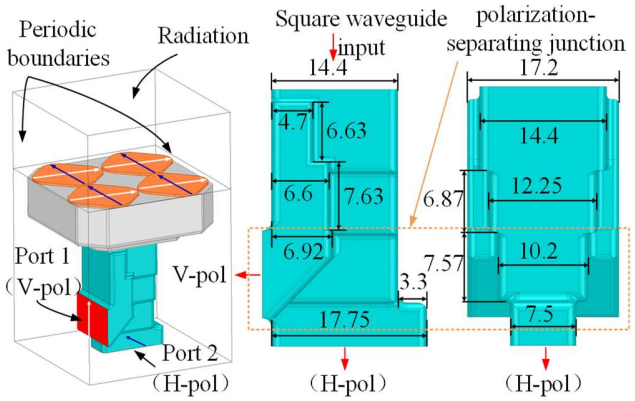


Fig. 4.2. 2×2 sub-array composed of diamond-shaped slots, dual-mode back cavity and OMT. All dimensions are given in millimeters.

4.3 2×2 sub-array

Fig. 4.2 shows the air-model of the 2×2-slot sub-array, with key geometric parameter values denoted in the caption. Periodic Boundary Conditions (PBC) are applied to simulate mutual coupling between array elements. In the sub-array, four diamond-shaped radiation slots are collectively excited by a dual-mode back cavity. To avoid grating lobes in the desired operation band, the period (d) between the adjacent elements along both the x - and y -directions is less than one free-space wavelength at the highest frequency. This is set to be d = 20 mm, slightly less than the free-space wavelength at 14.5 GHz.

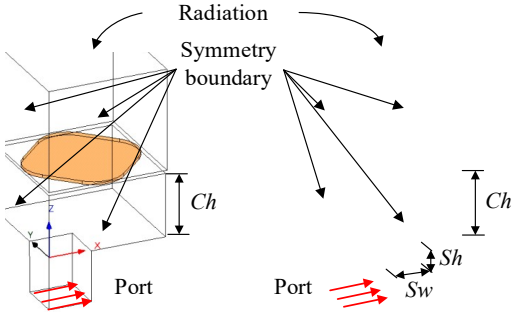


Fig. 4.3. Single-mode versus dual-mode back cavity: (a) Single-mode back cavity; (b) Dual-mode back cavity. Symmetric boundaries are applied

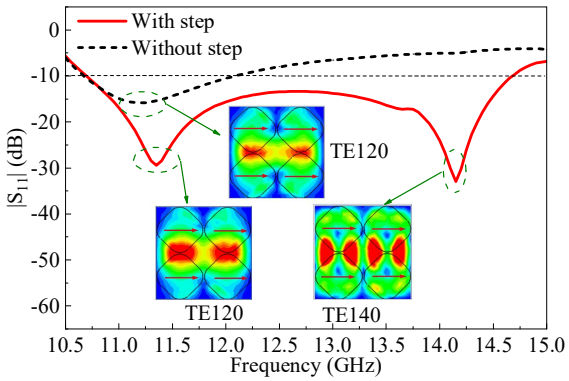


Fig. 4.4. Simulated $|S_{11}|$ of the single-mode and dual-mode back cavity. This is the operating mode when port 1 is excited (Horizontal polarization). When port 2 is exciting, the modes are TE210 and TE410 respectively.

The dual-mode back cavity is fed by a side-coupled OMT, which provides dual-polarization. More details about the back cavities, the slots and the OMT will be provided next.

4.3.1 Dual-mode Back Cavity

A crucial component in the subarray is the dual-mode back cavity, operating in the TE120 and TE140 modes. Fig. 4.3 shows the air model for both a conventional single-mode (TE120) and the proposed dual-mode back-cavity antenna. As can be observed, an extra step transition is introduced to the side wall of the latter. This discontinuity allows an additional TE140 resonance mode to be generated and therefore exciting the four radiation slots. Fig. 4.4 illustrates the simulated return loss for both back cavity antennas, with an inset showing the E-field patterns of the corresponding resonance modes. It is clear that

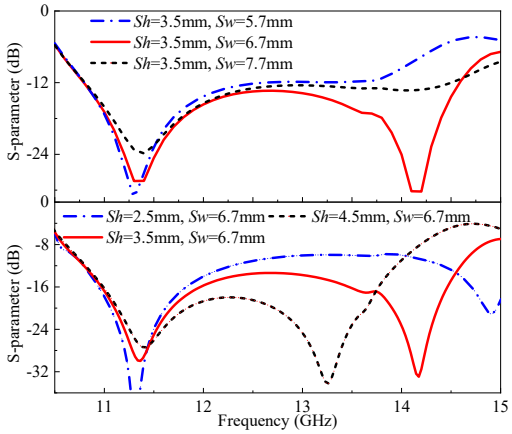


Fig. 4.5. Simulated $|S_{11}|$ of the proposed dual-mode back cavity with a parameter analysis for *Sh* and *Sw*.

one more resonance point appears in the dual-mode back cavity. By inspecting the E-field distribution, we can see that the low-frequency resonance is the classical TE120 mode, while the high-frequency resonance is due to the additional TE140 resonance mode. Moreover, from the direction of the E-field (indicated by the red arrows), all four radiation slots are excited in phase by both modes. Therefore, a wider radiation bandwidth can be achieved. Considering the 10-dB impedance matching bandwidth, there is an improvement of around 200% over the conventional single-mode back cavity. Fig. 4.5 further shows the

parameter analysis for two key dimensions (*Sh* and *Sw*) of the step discontinuity, when *Ch* is fixed to be 10.9 mm. It can be observed that the TE140 mode is efficiently excited as *Sw* increases, while the coupling between the TE120 and TE140 modes can be effectively controlled by adjusting *Sh*.

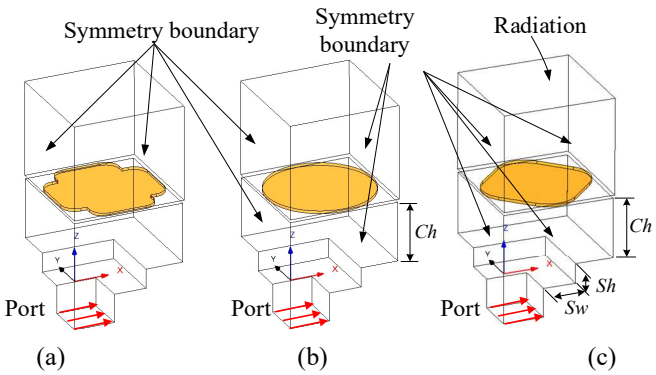


Fig. 4.6. Design variation of the radiating slots. (a) Cross slots; (b) Circular slots; (c) Diamond-shaped slots.

4.3.2 Design Variation of The Radiation slots

Another key feature of the proposed array is the radiating slot. As shown in Fig. 4.2, the four radiating slots are collectively excited by the underlying dual-mode back cavity. Traditionally, these slots are circles or crosses. Their shape is highly related to the E-field distribution of the resonance mode in the feeding back-cavity and significantly influences the radiation performance of the antenna array.

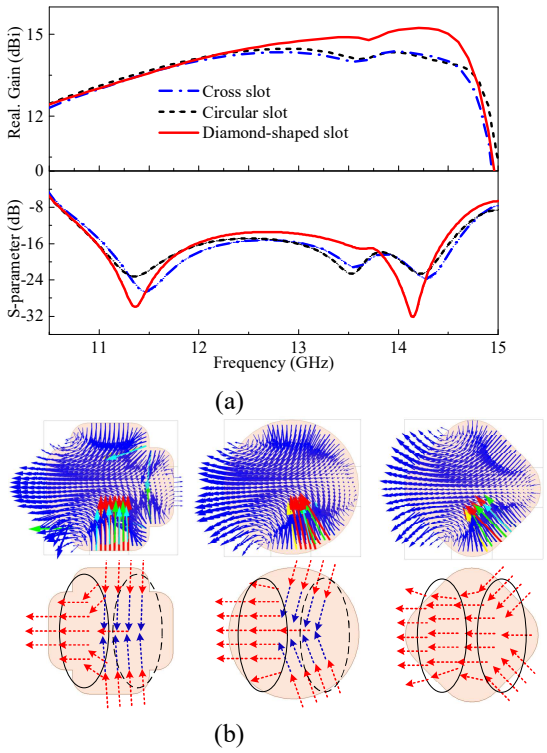


Fig. 4.7. Comparison of the three different types of radiation slots: (a) simulated antenna gain and reflection coefficient; (b) E-field patterns.

Fig. 4.6 shows the air model of three different radiating slots: the cross, the circle, and the proposed diamond-shaped slot. For the sake of comparative analysis, only one radiating unit is considered here, while symmetric boundaries are applied. Fig. 4.7(a) presents the simulated antenna gain and reflection coefficient for the three different slots. It is evident that the diamond-shaped slot exhibits significant advantages over the other two in terms of realized gain. To further investigate the reason behind this, Fig. 4.7(b) shows the simulated E-field distribution within the radiating slots at 14.5 GHz. The E-field vector in the diamond-shaped slot is mainly along the horizontal direction, while its vertical E-field component cancels itself. In contrast, the other two types of slots contain significant amount of unwanted vertical E-field components.

Fig. 4.8(a) further shows the simulated radiating E-field distribution of the sub-array for the three different slots. There is a noticeable depression in the middle of the wavefront for the cross and square radiating slots, while the diamond-shape slots achieve a much more uniform wavefront without middle depression. Therefore, it can realize higher gain than the other two common slots. Another advantage lies in the lower side lobe of the radiation pattern, as presented in Fig. 4.8(b).

An important but readily neglected point is the gain degradation around 13.8 GHz as shown in the simulated gain curve in Fig. 4.7(a). Looking at the E-field distribution in Fig. 4.9, we find that this degradation is caused by the spurious TE320 radiating mode. One

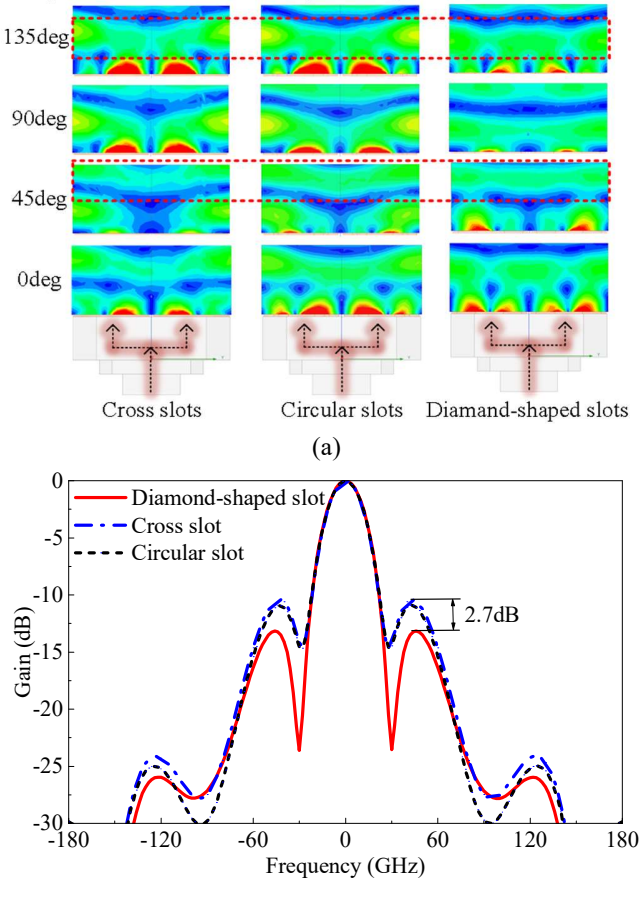


Fig. 4.8. Comparison of the three different types of radiation slots: (a) Simulated radiating E-field distribution; (b) Simulated radiation patterns.

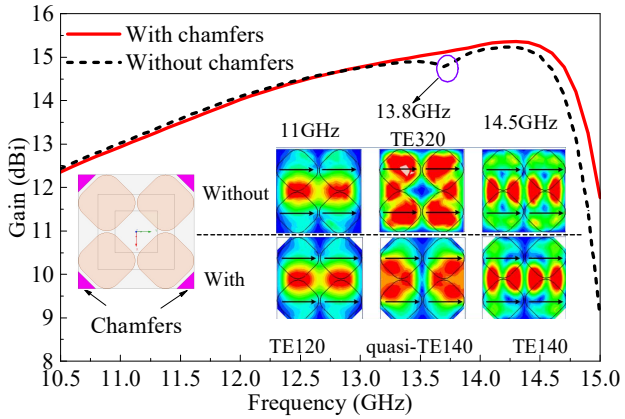


Fig. 4.9. Simulated realized gain of the subarray with or without chamfers and the E-fields distributions at 11 GHz, 13.8 GHz and 14.5 GHz.

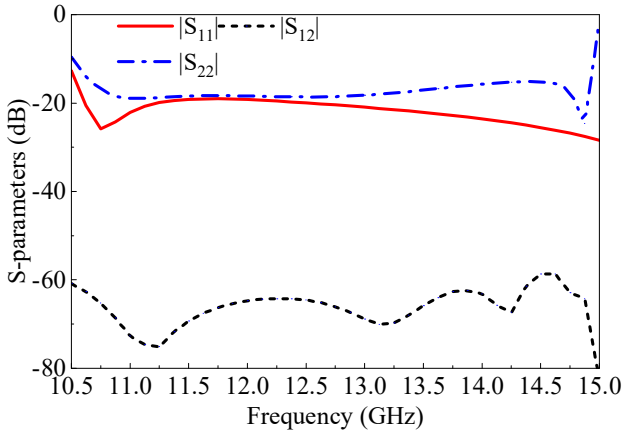


Fig. 4.10. Simulated S-parameters of the wideband waveguide OMT

approach to overcome this is to shift the position of the radiation slots, but this causes a non-uniform period for the array, generating undesired side lobes. Instead, we introduce chamfers into the dual-mode back cavity, as illustrated in Fig. 4.9. In this way, the spurious TE320 radiating mode is suppressed, and the E-field at 13.8 GHz is close to a quasi-TE140 mode, resulting in a smoother gain curve.

4.3.3 Wideband OMT

The proposed design employs a T-junction orthomode transducer (OMT) constructed from an isolated square waveguide, with two orthogonally arranged waveguide ports: Port-1 for H-polarization (aligned along the y-axis) and Port-2 for V-polarization (aligned along the x-axis) as shown in Fig. 4.2. The internal structure of the OMT consists of an input section, a polarization-separating junction, and individual output sections for each polarization. The input section transitions from a square waveguide to a T-shaped waveguide, where the polarization-separating junction directs each polarization along separate paths. V-polarization is extracted through a mitered bend, while H-polarization propagates straight through, minimizing mode conversion. The output transitions employ

stepped impedance matching to improve return loss and reduce reflections. The final optimized dimensions have been detailed in Fig. 4.2, with the OMT common port measuring 14.4 ×14.4 mm and a total height of 28.5 mm. The simulated S-parameters of the OMT are presented in Fig. 4.10, demonstrating excellent impedance matching, with both ports achieving a 10-dB bandwidth exceeding 35%. Additionally, the polarization isolation between the two orthogonal ports reaches 60 dB, ensuring high polarization purity.

4.4 Feeding Network

The feeding networks for the two polarizations are arranged in different layers and using different structures.

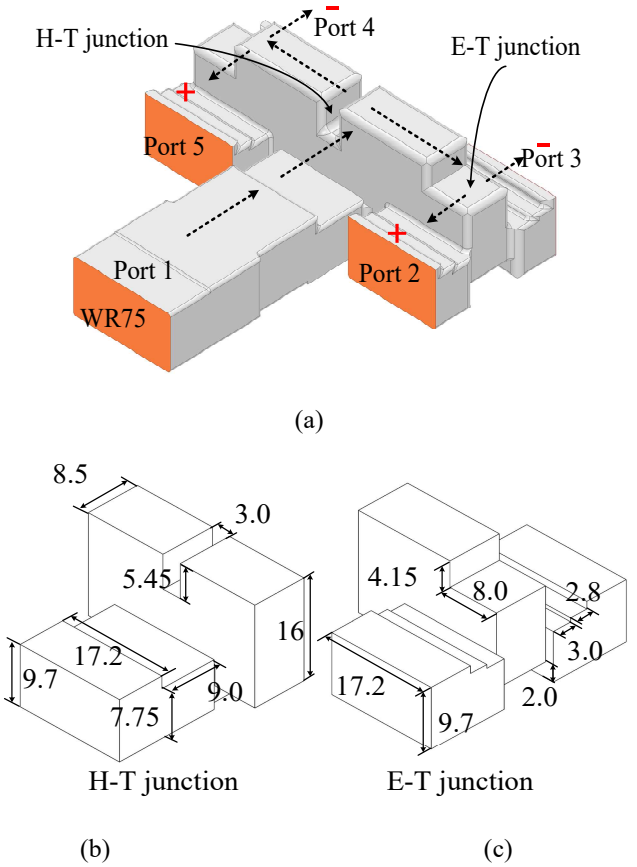


Fig. 4.11. Differential feeding network for the vertical polarization: (a) 3D view; (b) H-T junction; (c) E-T junction.

4.4.1 Differential Feeding Network for Vertical Polarization

The space for the feed network to the vertical polarization is severely constrained. Fig. 4.11(a) shows the 1-to-4 vertical polarization feed network. It consists of successively cascaded H-T junctions and E-T junctions designed to achieve differential feeding at the terminal points. The input is the standard WR75 waveguide, with fundamental mode bandwidth ranging from 10 to 15 GHz. To provide equal-amplitude and in-phase excitation to the four OMTs, the conventional approach is to employ a 1-to-4 power divider using E-

T junctions, feeding the OMTs from the same side. However, this method requires two parallel feed channels passing between the OMTs. This necessitates a narrowing of the E-plane in the feed waveguide. This design choice would contradict the original intent of using large cross-sectional rectangular waveguides, which are preferred for their ease of printing and copper plating.

In this design, a differential feed network based on standard rectangular waveguides is proposed, as depicted in Figure 4.11(b). To shorten the feed network, the H-T junction is bent up by 90°. This modification significantly reduces the network's profile, allowing it to fit within the limited space without sacrificing performance. The H-plane junction further splits into four differential outputs using E-T junctions as shown in Figure 4.11(c). An H-plane corner step is used for impedance matching. This design feature further compactifies the feed network. Fig. 4.12(a) demonstrates that this 1-to-4 feed network maintains equal amplitude and differential phase over the 10 to 15 GHz, with an amplitude imbalance of less than 0.1 dB and a phase imbalance within ±2°.

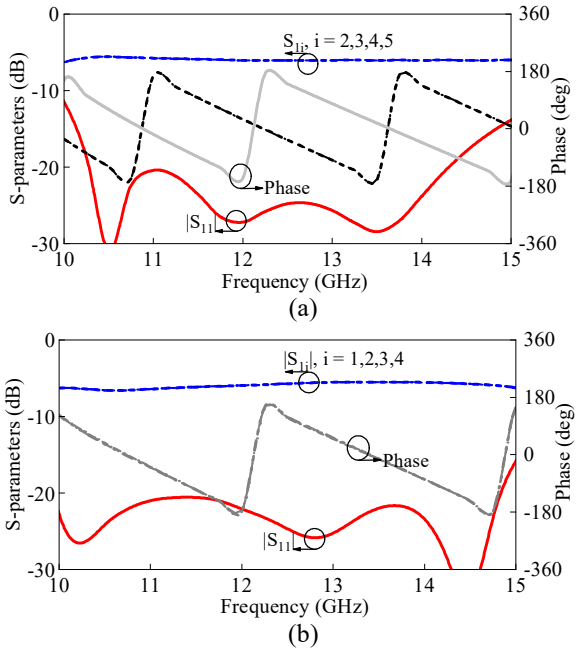


Fig. 4.12. Simulated S-parameters of the feed networks for: (a) Vertical polarization; (b) Horizontal polarization.

4.4.2 In-phase Feeding Network for Horizontal Polarization

Unlike the vertical polarization feeding network, the horizontal polarization feed networks are less constrained by the OMT square waveguides. Consequently, as shown in Fig. 4.13, it employs an equal-amplitude and in-phase feed network constructed with only H-T junctions. This ensures that the signal maintains its integrity and uniformity throughout the transmission path. At the end of the feed network, electromagnetic waves are magnetically coupled into the OMT through multi-step waveguide bend structure. This coupling mechanism is essential for maintaining low-profile. The simulated S-parameters in Fig. 4.12(b) highlight its equal-amplitude, in-phase performance and demonstrate the network's ability to maintain consistent signal strength and phase across the entire operating bandwidth.

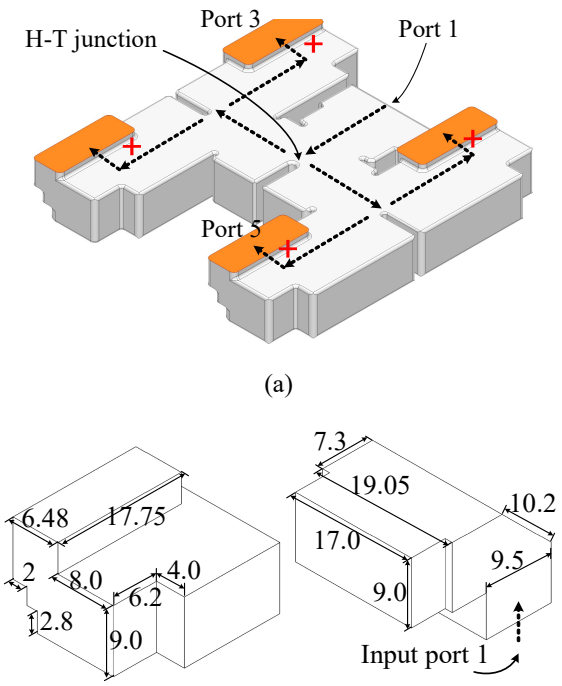


Fig. 4.13. In-phase feeding network for horizontal polarization: (a) 3D view; (b) Side-coupling slot; (c) 90° E-plane bend.

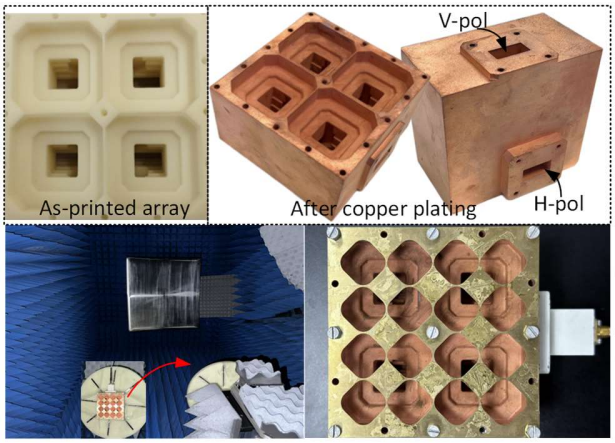


Fig. 4.14. Photographs of the fabricated prototype and testing environment.

4.5 Experimental Results

4.5.1 Manufacturing and Surface Treatment

As discussed earlier, the antenna array has been designed to incorporate a number of features that allow for the ease of 3D printing. However, given that the radiation slot layer is only 0.5 mm in thickness, printing the entire antenna as a single piece is plausible but

presents considerable risks for the structural integrity of the thin sheet radiation slots. Therefore, the radiation layer was fabricated separately from copper foil using laser-cut. The bulk of the antenna array, including the back cavities, OMTs, and feed networks, was manufactured using SLA 3D printing technology with Accura® HPC composite. To avoid internal support structures, the antenna array was tilted with respect to the baseplate during printing. The thinnest wall that has been printed is 0.8 mm. All threaded holes are reinforced with metal inserts to prevent damage from repeated screw removal and insertion.

Before metallization, the as-printed antenna was first surface-etched through mechanical and chemical treatments to enhance adhesion between the polymer and the plating layer. A 10 μm layer of silver and a 20 μm layer of copper were sequentially applied using electroless and electroplating technologies. All internal and external corners of the antenna structure were chamfered with a 0.5 mm radius to eliminate sharp edges that could hinder the plating process. Fig. 4.14 shows a photograph of the as printed and the plated antenna array. The antenna is 90 mm × 90 mm × 53 mm in size (with an aperture of 80 mm × 80 mm). The printing material has a density of 1.8 g/cm³, compared to 2.67 g/cm³ for 6061 aluminum alloy. As a result, the weight of the 3D-printed antenna is only 67% of that of the machined version. The S-parameters are measured using a network analyzer (Agilent E8361C), and the radiation patterns and gains are evaluated with a compact-range antenna testing system in an anechoic chamber.

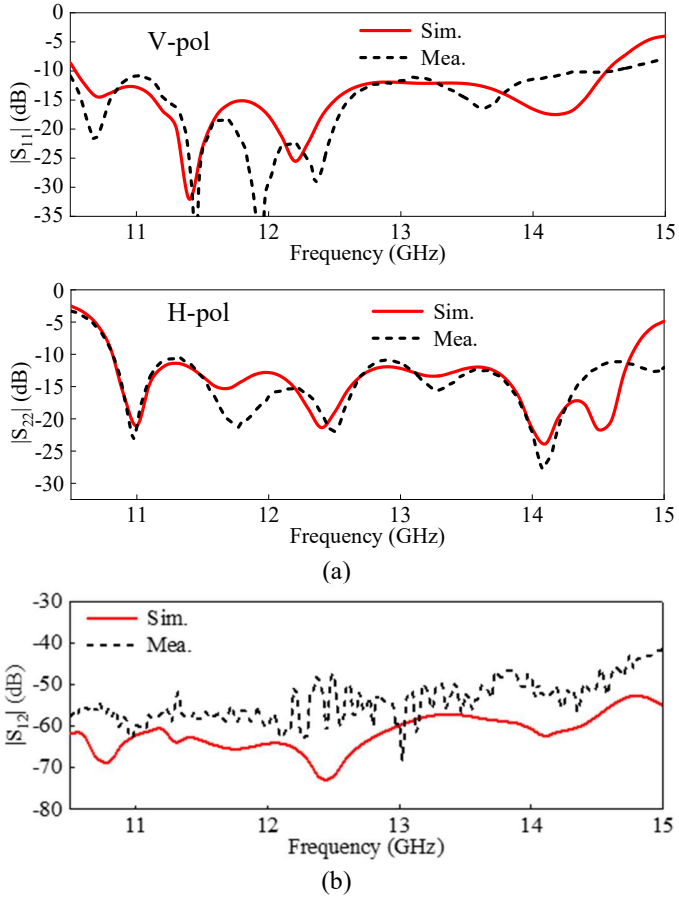


Fig. 4.15. Simulated and measured S-parameters. (a) V-pol $|S_{11}|$ and H-pol $|S_{22}|$; (b) Port-to-port isolation $|S_{12}|$.

4.5.2 S-parameters

Fig. 4.15(a) shows the simulated and measured reflection coefficients for the two polarizations. In the desired frequency range of 10.7-14.5 GHz (fractional bandwidth of 30.2%), the measured reflection coefficients are less than -10.5 dB and -11dB, respectively. The simulation and measurement results show good consistency. Fig. 4.15(b) plots the simulated and measured $|S_{12}|$. Over the same frequency band, the measured port-to-port isolation is higher than 48 dB.

4.5.3 Radiation Performance

Table I summarizes the normalized radiation patterns at 10.7, 12.5, and 14.5 GHz, both in simulation and measurement. These patterns are consistent across the frequency band and align well with the simulated data. Side lobe levels are maintained around -13.2 dB, as expected for a square array driven by constant amplitude and phase excitation. The measured cross-polarization discriminations (XPDs) for the two polarizations are higher than 37 dB. Fig. 4.16 shows the simulated and measured peak gains, antenna efficiencies and aperture efficiencies. The discrepancy between the measured and simulated peak gains is less than 0.5 dB, attributed primarily to fabrication tolerances, assembly, and measurement errors. For both polarizations, the measured antenna and aperture efficiencies exceed 90% and 72%, respectively. The measured antenna efficiency, $\eta_{\text{mea_an}}$, and aperture efficiency, $\eta_{\text{mea_ap}}$, are calculated using the following equations:

$$\eta_{mea_an} = \frac{G_{mea}}{D_{sim}} \tag{1}$$

$$\eta_{mea_ap} = \frac{G_{mea}}{D_{sim}} * \frac{D_{sim}\lambda^2}{4\pi A} \tag{2}$$

where G_{mea} is the measured peak gain, D_{sim} is the simulated directivity, λ is the free-space wavelength at the operating frequency, and A is the aperture area of the antenna.

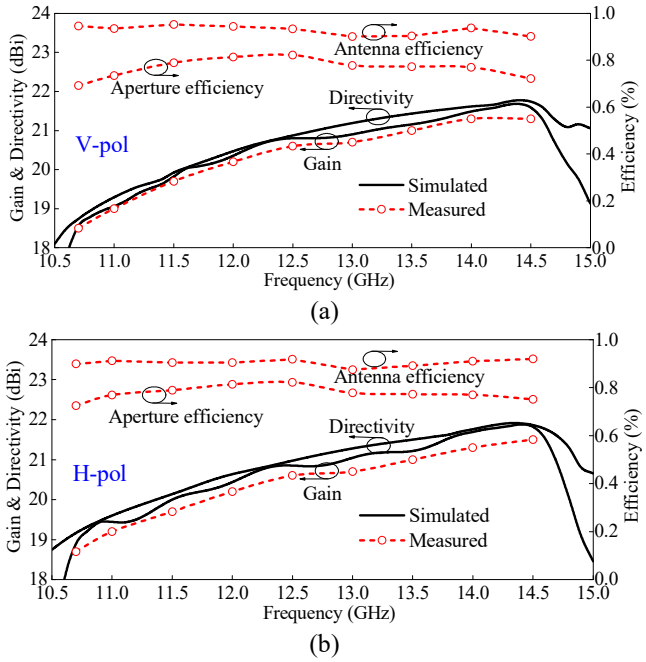


Fig. 4.16. Measured peak gain and calculated antenna efficiency and aperture efficiency: (a) V- pol; (b) H-pol.

TABLE II
PERFORMANCE COMPARISON OF DUAL-POLARIZED ANTENNAS WITH OR WITHOUT BACK CAVITY

Ref.	Element Type	Back Cavity Type	Pol.	Fabrication Technology	Scale	Center freq. (GHz)/ FBW[a] (%)	Gain[b] (dBi)	AE[c]	Isolation (dB)	Cross Pol. (dB)
[9]	Square horn	/	Dual-CP[d]	CNC Milling	4×4	12.5/32	21.2	>79%	>25.0	< -20.0
[16]	Square horn	/	Dual-LP[e]	CNC Milling	8×8	12.5/32				
[18]	Square Slot	Single-mode	Dual-LP	CNC Milling	16×16	13.5/17.1	31.6	>70%	>39.5	< -29.0
[19]	Square slot	Single-mode	Dual-LP	Diffusion bonding	16×16	61.5/14	32.4	>60%	>50.8	< -40.0
[20]	Cross slot	Single-mode	Dual-LP	Diffusion bonding	16×16	62/6.5	32.5	>80%	>50.0	< -25.0
[22]	Square Slot	Single-mode	Dual-CP	DMLS	16×16	13.2/19	32.3	55	>15.0	< -13.0
[23]	Cross slot	Single-mode Single-mode	LP LP	DMLS	4×4	12.26-13.4/8.9 13.72-15/8.9	23.8 26.3	N.a N.a	>32.9 >40.5	< -47.3 < -42.0
[24]	Cross slot	Triple-mode	Dual-LP	DMLS	8×8	34/26.3	28.5	N.a	>36.0	< -30.0
[25]	Circular slot	Dual-mode	Dual-LP	Copper-Plating SLA	4×4	13.0/22.8	21.2	>55%	>40.0	< -35.0
This work	Diamond-shaped slot	Dual-mode	Dual-LP	Copper-Plating SLA	4×4	13.0/30.2	26.5	>72%	>48.0	< -37.0

[a]FBW: fractional bandwidth. [b]The values are obtained peak gain. [c]The AE is aperture efficiency. [d]CP is circular polarization. [e]LP is linear polarization.

4.5.4 Comparison

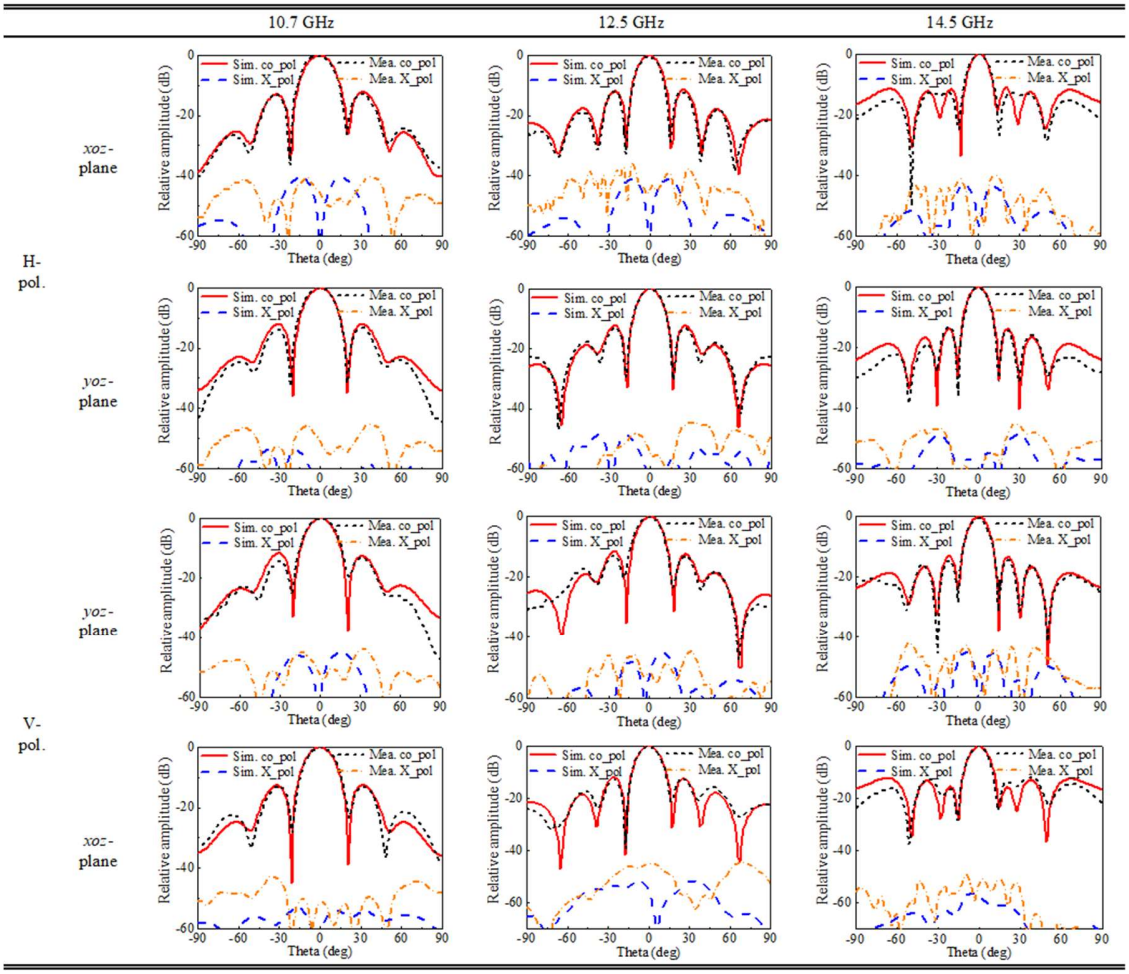
The performance of this antenna is compared with some published dual-polarized antennas in Table II. [9] and [16] reported over 30% relative bandwidth using compact, one-to-one excited radiating elements without backed cavities. However, their feeding networks are complex, relying on waveguide-coaxial transmission lines. [18]-[23] achieved up to 19% impedance bandwidth with single-mode backed cavities. [25] used a dual mode backed cavity operating in TE320/TE230 and TE410/TE140 modes, achieving 22.8% impedance bandwidth. However, its non-uniform distribution of radiating slots introduced grating lobes. [24] designed a tri-mode backed cavity operating in TE210/TE210, TE320/TE230, and TE410/TE140 modes, achieving 26.3% impedance bandwidth. Nevertheless, the large radiating element period for the TE410 mode leads to significant grating lobes at high frequencies.

Multi-mode backed cavities can enhance bandwidth and simplify feeding network design as compared to antennas without a backed cavity. They are also more suitable for 3D printing. For instance, [24] used rectangular waveguides to design a feeding network and achieved 26.3% impedance bandwidth using the DMLS process. [25] used a ridge waveguide, manufactured with the SLA 3D printing process and copper-plating. However, the complexity of the ridge waveguide-based feeding network presented a challenge for copper plating on the internal surfaces. As a result, the antennas were printed in multiple piece parts.

In this work, we present a novel dual mode backed cavity with wideband feeding networks based on standard rectangular waveguides. The structure is printed using the SLA process and copper plated. The design achieves a competitive 30.2% fractional bandwidth (FBW) and effectively suppresses grating lobes. The antenna also demonstrates stable

radiation patterns and high aperture efficiency (>72%) across the frequency band from 10.7 to 14.5GHz.

TABLE I
NORMALIZED RADIATION PATTERNS OF THE DUAL-POLARIZED ARRAY ANTENNA



4.6 Conclusion

This paper presents a novel wideband dual-polarized hollow-waveguide antenna array, showcasing advancements in antenna manufacturing using 3D printing technique. By implementing a dual-mode back cavity operating in TE120/TE210 and TE140/TE410 modes, and incorporating a diamond-shaped radiation slot, the antenna achieves a wide radiation bandwidth and enhanced stability in the radiation pattern. The use of SLA technology for 3D printing and subsequent copper plating facilitates the creation of a compact, lightweight, and high-performance antenna array. Compared to previously published designs, this work proposed a simplified feeding network, under severe space constraint, while still allowing the ease of printing and plating. A design-for-manufacture approach was used throughout the work. Through new design and fabrication techniques, this work paves the way for further advancements in dual-polarized antennas, potentially leading to broader bandwidths and improved performance in waveguide antenna systems.

References

[1] Xu, X. Xia, K.-M. Luk and W. Hong, "Millimeter-wave array antennas using broadband 3D folded strip elements for B5G/6G communications", *IEEE Trans. Antennas Propag*., vol. 70, no. 12, pp. 11569-11581, Dec. 2022.

[2] L. Chettri and R. Bera, "A comprehensive survey on Internet of Things (IoT) toward 5G wireless systems", *IEEE Internet Things J*., vol. 7, no. 1, pp. 16-32, Jan. 2020.

[3] C. Deng et al., "IEEE 802.11be Wi-Fi 7: New challenges and opportunities", *IEEE Commun. Surveys Tuts*., vol. 22, no. 4, pp. 2136-2166, 4th Quart. 2020.

[4] M. A. El Harmil, M. A. Elwahab, R. A. Abdelrassoul, M. S. Zaghloul and M. El Ghamry, "SATCOM on-the-Move Antenna Tracking Survey", *2021 9th International Japan-Africa Conference on Electronics Communications and Computations (JAC-ECC),* pp. 26-29, 2021.

[5] X. Qu, Z. Yang, W. Zong and C. Yu, "Research on Polarization Tracking of SATCOM on the move", *2020 IEEE International Conference on Computational Electromagnetics (ICCEM)*, pp. 162-163, 2020.

[6] Q. You, Y. Lu, Y. Wang, J. Xu, J. Huang and W. Hong, "Hollow-Waveguide Tri-Band Shared-Aperture Full-Corporate-Feed Continuous Transverse Stub Antenna," *IEEE Trans. Antennas Propag*., vol. 70, no. 8, pp. 6635-6645, Aug. 2022

[7] Thai Van Trinh, Jinsu Park, Chan Mi Song, Sungchan Song, Keum Cheol Hwang, "A 3-D Metal-Printed Dual-Polarized Ridged Waveguide Slot Array Antenna for X-Band Applications", *Applied Sciences*, vol.13, no.8, pp.4996, 2023.

[8] Q. You, Y. Wang, M. Huang, J. Huang, Z. -W. Zheng and Y. Lu, "Wideband Dual-Polarized Hollow-Waveguide Slot Array Antenna," *IEEE Trans. Antennas Propag*., vol. 70, no. 10, pp. 9326-9336, Oct. 2022.

[9] Y. Hu, Y. Lu, K. Zhou, Q. You and J. Huang, "Wideband Hollow-Waveguide Dual-Polarized Antenna with Reduced Metal Layers" *IEEE Trans. Antennas Propag*., vol. 72, no. 1, pp. 1027-1032, Jan. 2024.

[10] X. Dai and K. M. Luk, "A wideband dual-polarized antenna for millimeter-wave applications", *IEEE Trans. Antennas Propag*., vol. 69, no. 4, pp. 2380-2385, Apr. 2021.

[11] Q. Chen, J. A. Laurinaho, A. Khripkov, J. Ilvonen, R. Montoya Moreno, V. Viikari, "A Wideband Dual-Polarized Endfire Antenna Array for 5G mm-Wave Smartphones", *IEEE Trans. Antennas Propag*., vol.72, no.2, pp.1118-1127, 2024.

[12] Bing-Jie Xiang, Kwai-Man Luk, "A Wideband Dual-Linearly Polarized Folded ME-Dipole Transmitarray Antenna With Low H/F Ratio",*IEEE Trans. Antennas Propag*., vol.72, no.1, pp.466-475, 2024.

[13] W. Li, X. Tang and Y. Yang, "Design and implementation of SIW cavity-backed dual-polarization antenna array with dual high-order modes", *IEEE Trans. Antennas Propag*., vol. 67, no. 7, pp. 4889-4894, Jul. 2019.

[14] Z. Chen, H. Liu, J. Yu and X. Chen, "High gain broadband and dual-polarized substrate integrated waveguide cavity-backed slot antenna array for 60 GHz band", *IEEE Access*, vol. 6, pp. 31012-31022, 2018.

[15] Q. Zhu, K. Bo Ng, C. Hou Chan and K.-M. Luk, "Substrate-integrated-waveguide-fed array antenna covering 57 – 71 GHz band for 5G applications", *IEEE Trans. Antennas Propag*., vol. 65, no. 12, pp. 6298-6306, Dec. 2017.

[16] Q. You, Y. Lu, M. Huang, J. Xu and J. Huang, “High-efficiency airfilled wideband ±45° dual-polarized slot array antenna,” *IEEE Trans. Antennas Propag*., vol. 71, no. 5, pp. 4582-4587, May 2023.
[17] Yilin Dong, Rong Xu, Yu-Hang Yang, Shi-Gang Zhou, “Compact Shared-Aperture Dual-Band Dual-Circularly-Polarized Waveguide Antenna Array Operating at K/Ka-Band”, *IEEE Trans. Antennas Propag*., vol.71, no.1, pp.443-449, 2023.
[18] S.-G. Zhou, G.-L. Huang, T.-H. Chio, J.-J. Yang and G. Wei, “Design of a wideband dual-polarization full-corporate waveguide feed antenna array”, *IEEE Trans. Antennas Propag*., vol. 63, no. 11, pp. 4775-4782, Nov. 2015.
[19] Y. Wu, J. Hirokawa and T. Tomura,“Dual-Polarized Full-Metal Perpendicular-Corporate-Feed Parallel-Plate Waveguide Slot Array Antenna,” *IEEE Trans. Antennas Propag*., vol. 72, no. 7, pp. 6093-6098, July 2024.
[20] D. Kim, M. Zhang, J. Hirokawa and M. Ando, “Design and Fabrication of a Dual-Polarization Waveguide Slot Array Antenna With High Isolation and High Antenna Efficiency for the 60 GHz Band,” *IEEE Trans. Antennas Propag*., vol. 62, no. 6, pp. 3019-3027, June 2014
[21] K. Wada, T. Tomura and J. Hirokawa, "Dual-polarized 2-D beam mode orthogonal multiplexing antenna system for the nonfar region", *IEEE Trans. Antennas Propag*., vol. 68, no. 9, pp. 6614-6623, Sep. 2020.
[22] S. -G. Zhou, G. -L. Huang and T. -H. Chio, "A Lightweight, Wideband, Dual-Circular-Polarized Waveguide Cavity Array Designed With Direct Metal Laser Sintering Considerations," *IEEE Trans. Antennas Propag*, vol. 66, no. 2, pp. 675-682, Feb. 2018.
[23] J. Zhang, X. Li, Z. Qi, Y. Huang and H. Zhu, “Dual-Band Dual-Polarization Horn Antenna Array Based on Orthomode Transducers with High Isolation for Satellite Communication,” *IEEE Trans. Antennas Propag*., vol. 70, no. 10, pp. 9247-9259, Oct. 2022.
[24] F. Sun, Y. Li, J. Wang, Y. Ma, L. Ge, B. Ai and R.He, “A millimeter-wave wideband dual-polarized antenna array with 3-D-printed air-filled differential feeding cavities,” *IEEE Trans. Antennas Propag*., vol. 70, no. 2, pp. 1020-1032, Feb. 2022.
[25] Y. Cheng and Y. Dong, “Wideband Dual-Polarized Gap Waveguide Antenna Array Based on Novel 3-D-Printed Feeding-Network Topologies,” *IEEE Trans. Antennas Propag.*, vol. 71, no. 2, pp. 1493-1505, Feb. 2023.
[26] A. Palomares-Caballero, A. Alex-Amor, J. Valenzuela-Valdes and P. Padilla, “Millimeter-wave 3-D-printed antenna array based on gap-waveguide technology and split E-plane waveguide,” *IEEE Trans. Antennas Propag*., vol. 69, no. 1, pp. 164-172, Jan. 2021.
[27] G. P. Le Sage, “3D printed waveguide slot array antennas”, *IEEE Access*, vol. 4, pp. 1258-1265, 2016.
[28] C. Dong et al., “Dual Circularly-Polarized Septum Antenna Array Based on an Air-Filled Dual-Mode Feeding Network,” *IEEE Trans. Antennas Propag.*, vol. 72, no. 3, pp. 2938-2943, March 2024.
[29] M. Ferrando-Rocher, A. U. Zaman, J. Yang and A. Valero-Nogueira, "A dual-polarized slotted-waveguide antenna based on gap waveguide technology", *Proc. 11th Eur. Conf. Antennas Propag. (EUCAP),* pp. 3726-3727, Mar. 2017.

[30] Y. Hu, Y. Lu, K. Zhou, Q. You and J. Huang, “Wideband Hollow-Waveguide Dual-Polarized Antenna With Reduced Metal Layers,” *IEEE Trans. Antennas Propag*., vol. 72, no. 1, pp. 1027-1032, Jan. 2024.
[31] Y. Miura, J. Hirokawa, M. Ando, Y. Shibuya and G. Yoshida, “Double-Layer Full-Corporate-Feed Hollow-Waveguide Slot Array Antenna in the 60-GHz Band,” *IEEE Trans. Antennas Propag*., vol. 59, no. 8, pp. 2844-2851, Aug. 2011.

CHAPTER 5: WIDEBAND CORPORATE-FED DUAL-BAND DUAL-POLARIZED LONG SLOT ARRAY ANTENNA FOR SATCOM

Qingchun You, Kai Ye, Lu Qian, Yi Wang and Jifu Huang

Yi Wang proposed, organized, and oversaw the entire study, taking the lead on the project. Qingchun You originated the design, conducted the theoretical modelling, analysis, simulations, carried out the experiments, interpreted the results, and drafted the manuscript. Lu Qian and Jifu Huang offered advice throughout the project, while Kai Ye supported the fabrication. All authors contributed to the writing of the paper and reviewed the final manuscript.

This chapter is based on the following paper which is under revise after major revision: Q. You, K. Ye, L. Qian, Y. Wang and J. Huang, "Dual-band Dual-polarized Waveguide Array Antenna with Flexible Frequency-ratio for SATCOM," *IEEE Trans Antennas Propag*, Submit in July. 2024, Under revise, after major revision.

Abstract

This paper presents a design approach for dual-band dual-polarized (DBDP) waveguide antenna array. A novel transmission network using orthogonal parallel plate waveguide (PPW) is proposed for the excitation of dual polarization. Dual band bandstop structures are incorporated into the PPW feeding network. They suppress the leakage between the two polarizations and improve the transmission efficiency of the network. They also enable a wide range of frequency ratio from 1 to 2.64 between the two bands. A new orthogonal linear signal generator (LSG) enables ultra-wideband, dual-polarized quasi-TEM excitation, ensuring consistent and reliable performance across a broad bandwidth. Fed by four sequentially rotated single-ridge 1-to-4 power dividers, the LSG effectively generates dual-polarized signals. For demonstration, a K/Ka-band shared-aperture dual-polarized array antenna has been designed, analyzed and experimentally verified. The array features a wide impedance bandwidth (17.7 - 21.2 GHz and 27.5 - 31 GHz), high isolation (>50 dB), and excellent cross polarization discrimination (XPD) (>40 dB). The prototype demonstrates high aperture efficiency up to 80% and consistent radiation patterns at both bands, affirming its potential for SATCOM systems.

Keywords: Waveguide antenna array, dual-band shared-aperture, millimeter wave antennas, satellite communication.

5.1 Introduction

Satellite communication (SATCOM) systems employ Ku-, K- and Ka-bands to establish high data rate down- and up-links [1]. To maintain stable communication and improve isolation between transmitted and received signals, high gain antennas supporting dual linear polarizations (LPs) or dual circular polarizations (CPs) at the Ku-band (10.7 - 12.75 GHz, 13.75 - 14.5 GHz) or dual CPs at K- and Ka-bands (17.7 - 21.2 GHz, 27.5 – 31 GHz) are highly demanded.

Active electronically scanned array (AESA) plays an important role in low Earth orbit (LEO) SATCOM systems for their rapid beam-steering capability and programmable sidelobe envelope [2]. However, when applied to geostationary (GEO) SATCOM systems, the requirement for high gain significantly increases the cost and power consumption of AESA. Furthermore, the gain rolls off at higher steering angles, combined with a typical beam-steering range of approximately ±60°, significantly restricts their applicability in GEO SATCOM systems. These limitations result in degraded performance when attempting to achieve wide coverage or high efficiency at extreme off-boresight angles, which are often required for GEO SATCOM applications. For instance, some commercial suppliers employ a hybrid system combining Variable Inclination Continuous Transverse Stub (ViCTS) antennas with AESA on aircraft to support both GEO and LEO satellite communication services [3]. For GEO SATCOM reflector antennas play a very important role due to their simple structure, which allows for multi-band and multi-polarization [4], [5], [6], [7]. They are commonly used in ground gateway stations and SATCOM-on-the-move (SOTM) systems. However, their excessive profile makes them less suitable for airborne and vehicular SOTM systems or portable stations. Low-profile waveguide array antennas have emerged as a competitive alternative [8], [9].

There are three main waveguide based high-gain antenna solutions for SATCOM. The first is a wideband single-polarization array covering both the reception and transmission bands [10], [11], [12], [13]. However, for most satellite communication scenarios, orthogonal polarizations for transmission and reception are needed. One common method to achieve this is by using two separate antennas [14]. This approach, however, results in increased costs and a larger antenna footprint. An alternative is to add a dual circular polarizer to a single-polarization antenna, to achieve mutual orthogonal polarizations in the reception and transmission bands [15], [16], [17], [18]. This is a co-aperture solution, but its bandwidth is limited by that of the polarizer. For example, the continuous transverse stub (CTS) antenna with a circular polarizer in [18] offers limited axial ratio bandwidths over 20.1 - 22.1 GHz and 28.7 – 30 GHz and is not able to cover the entire K-band and Ka-band required for SATCOM.

The second approach involves using wideband dual-polarized arrays [19], [20], [21], [22], [23], [24], [25]. These antennas can operate with dual polarization in both transmission and reception bands. By adjusting the amplitude and phase of the two orthogonal polarizations, they can synthesize any desired polarization direction. This feature is particularly useful for polarization tracking and switching in SOTM (SATCOM On The Move) systems. Typically, these arrays utilize Orthogonal Mode Transducers (OMT) or septum polarizers. A notable example is a broadband dual circular polarized antenna based on septum polarizers, covering 19-30 GHz [25]. Due to the limited impedance bandwidth of the polarizer, this still cannot cover the required K- and Ka-band.

The third solution is the DBDP arrays where radiating elements for different frequencies are consolidated into a single aperture [26], [27], [28], [29]. The added design challenge for the dual-band solution is that the realizable frequency ratio is often constrained by the topological structure, making it difficult to adjust especially for large frequency ratio. In [30], the antenna merges Ku-band linearly polarized elements with Ka-band circularly polarized ones within the same aperture. The frequency ratio is fixed to about 2:1(14.4 - 17.5 GHz，32.5 - 35 GHz), which makes it only partially compatible with the spectrum of SATCOM. A recent advancement is a full-metal dual-band array with orthogonal polarization, where the K-band operates with horizontal polarization and the Ka-band with vertical polarization [31]. This antenna can be considered as an overlap of two single-linearly polarized antennas at different frequencies. It cannot synthesize arbitrary polarization directions through two orthogonal polarization components like a dual-polarized array. So, it fails to meet the requirements for polarization switching and tracking.

CTS antennas, known for their wideband and multi-band capability and high efficiency, have been widely used in high-performance millimeter-wave (mmW) antenna applications [32], [33]. A tri-band shared-aperture single-linearly polarized CTS antenna is reported for Ku-/K-/Ka-band SATCOM by frequency multiplexing in the PPW feed network [34]. However, this antenna only has a single polarization. For dual polarization, cross-connected single-mode traveling-wave CTS arrays are mainly suited for narrowband applications, as reported in [35]and [36]. In [37]and [38], a novel dual-polarized CTS array based on a dual-mode CPPW corporate-feed network was introduced. This array achieves dual-polarized radiation and enables beam scanning along the long slots. Although the bandwidth shows a significant improvement compared to series-fed arrays, it remains limited to 11.6%. This limitation arises because the dual-mode CPPW transmission line operates in both quasi-TEM mode (vertical polarization) and quasi-TE1 mode (horizontal polarization), with the bandwidth primarily constrained by the TE1 mode. If both polarizations operate in TEM mode and a corporate-feed network is used, it could potentially offer a wider bandwidth. However, placing the single-mode corporate-feed CTS arrays orthogonally in a shared aperture for dual polarization is not trivial. Additionally, the dual-band requirement further complicates the design of the feed network.

This work will address this design challenge using orthogonal CST arrays with a dua-band PPW feeding network. We will propose a methodology to suppress the leakage between the two polarizations and to achieve a wide range of frequency ratio up to 2.64:1 by using several bandstop structures. The orthogonally placed CTS arrays also dictate a new orthogonal linear signal generator for the quasi-TEM excitation. We will demonstrate a DBDP array antenna operating at K- and Ka-bands (17.7-21.2 GHz, and 27.5-31 GHz). The rest of the paper is organized as follows: Section II describes the antenna configuration. Sections III and IV present the analysis, design, and results, followed by the conclusion in Section V.

5.2 Overview of Antenna Array Configuration

Fig. 5.1 illustrates the structure of the proposed DBDP waveguide array antenna. The complete 8×8 radiation part is composed of sixteen 2×2 subarrays. Each 2×2 subarray consists of orthogonally intersecting parallel plate waveguide (PPW) power dividers and multi-stage stepped impedance transformers, which are used for impedance matching between the power dividers and free space. A novel dual-polarized PPW parallel feed

network is designed to provide equal-amplitude, in-phase excitation to all subarrays. This PPW feeding network is formed by two orthogonally overlapping single-polarized PPW feeding networks. The incorporation of dual-band bandstop structures within the PPW feeding network effectively suppresses leakage between the two polarizations, enhancing the overall transmission efficiency of the network. A new orthogonal linear signal generator (LSG), placed after the PPW feeding network, enables ultra-wideband, dual-polarized quasi-TEM excitation. The LSG, fed by four sequentially rotated single-ridge 1-to-4 power dividers, effectively generates dual-polarized signals. Finally, each polarized signal is combined by an equal-amplitude in-phase combiner to form horizontal and vertical polarization ports. Additional cascaded waveguide diplexers help separate the receive and transmit signals, forming horizontal and vertical ports for both K-band and Ka-band. This configuration offers increased flexibility for circular polarization synthesis and switching. All simulations were conducted using ANSYS HFSS. Detailed designs of the key constituent parts will be presented in the following sections.

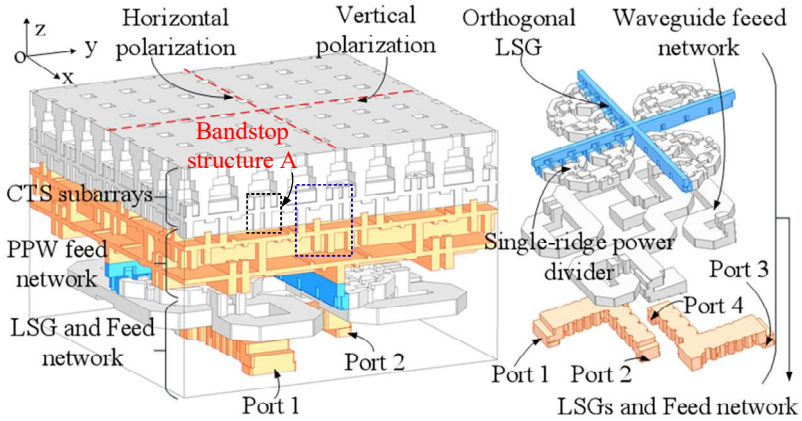


Fig. 5.1. Configuration of the proposed DBDP antenna.

5.3 Evolution and Analysis

5.3.1 Design Evolution (2×2 Array)

The antenna design evolution will be illustrated using a 2× 2 subarray in Fig. 5.2. The initial model is a classic single-polarized CTS array (Subarray I), composed of multi-stage stepped impedance transformers and PPW power dividers. The spacing (p) between adjacent elements is maintained at 9 mm, which is less than the free-space wavelength at the highest operating frequency (31 GHz), thereby preventing the occurrence of grating lobes. Additionally, periodic boundary conditions are added around the subarray to simulate coupling between subarrays in the array.

A simple and straightforward approach to achieving dual polarization is orthogonally combining two single-polarized CTS arrays (Subarray II), as shown in Fig. 5.2(b). However, this approach faces two critical issues that need to be addressed: 1) Energy leakage occurs in the overlapping regions of the two polarizations (blue faces marked in Fig. 5.2(b)); 2) In the non-overlapping regions, energy is radiated into free space through the impedance transformers, where the partial overlap disrupts the quasi-TEM wave propagation, and causes amplitude imbalance, as shown in Fig. 5.3. To address these issues, we first extend the overlapping regions of the PPW power dividers to the periodic

boundaries to mitigate the amplitude and phase imbalance (Subarray III), as shown in Fig. 5.2(c). Then, we introduce dual-band bandstop structures at each leakage face to suppress leakage between two polarizations, ultimately forming the desired Subarray IV, as shown in Fig. 5.2(d). dividers to the periodic boundaries to mitigate the amplitude and phase imbalance (Subarray III), as shown in Fig. 5.2(c). Then, we introduce dual-band bandstop structures at each leakage face to suppress leakage between two polarizations, ultimately forming the desired Subarray IV, as shown in Fig. 5.2(d).

5.3.2 Bandstop structure to suppress leakage between the two polarizations

To better illustrate the working principle of the bandstop structure, we denote the leakage face using a virtual port, labeled as C in Fig. 5.2(e). Here, A represents the incoming signal from the PPW power divider, and B represents the outgoing signal to the impedance

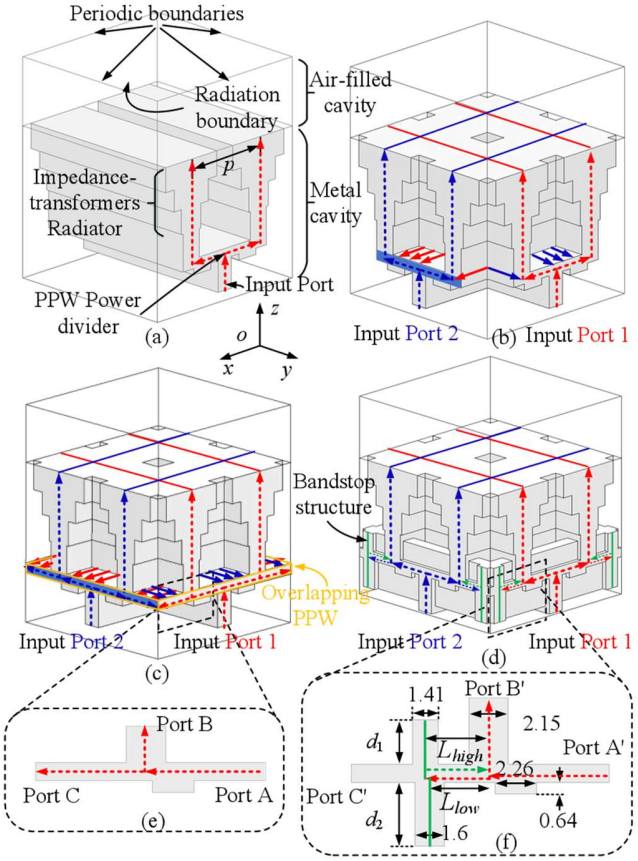


Fig. 5.2. Design evolution of 2×2 sub-arrays. (a) Subarray I: Single-polarized sub-array. (b) Subarray II: orthogonally placed identical single-polarization subarrays. (c) Subarray III: dual-polarized sub-array with extended PPW. (d) Subarray IV: dual-polarized sub-array with bandstop structures. (e) Side view of the power divider in Fig. 5.2(c). (f) Bandstop structure A. All dimensions are given in millimeters.

transformer. To suppress this leakage, we add bandstop structures to the overlapping sections, as shown in Fig. 5.2(f). These short-circuiting stubs are strategically positioned approximately λ/4 distance from the junction to achieve optimal impedance matching. Since the antenna operates over two widely separated frequency bands, a single short-circuit stub is insufficient to separate the bands, resulting in increased insertion loss.

Therefore, a dual-band bandstop structure is proposed to enhance suppression, as illustrated in Fig. 5.2(f). Two short-circuit stubs are placed opposite to each other along the E-plane of the PPW, each functioning as a bandstop resonator. Each stub blocks the leakage of one band, determined by the lengths d_1 or d_2. This bandstop structure allows the crossover of both orthogonal signals through the overlapping PPW with low insertion loss and high port-to-port isolation (over 50 dB), as demonstrated by the simulated transmission, reflection, and isolation performance in Fig. 5.4.

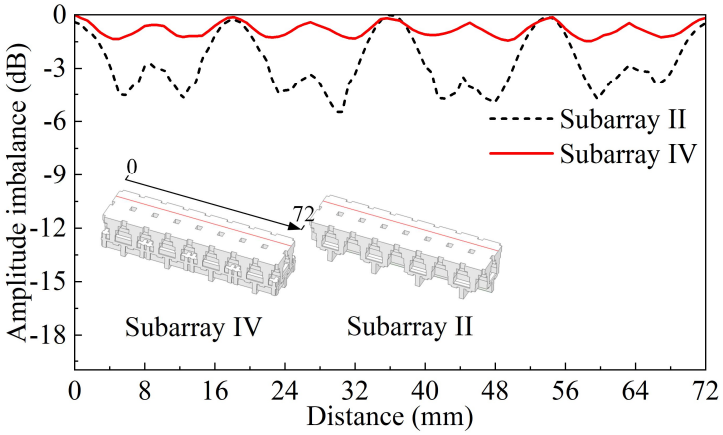


Fig. 5.3. E-field distributions along the PPW slots.

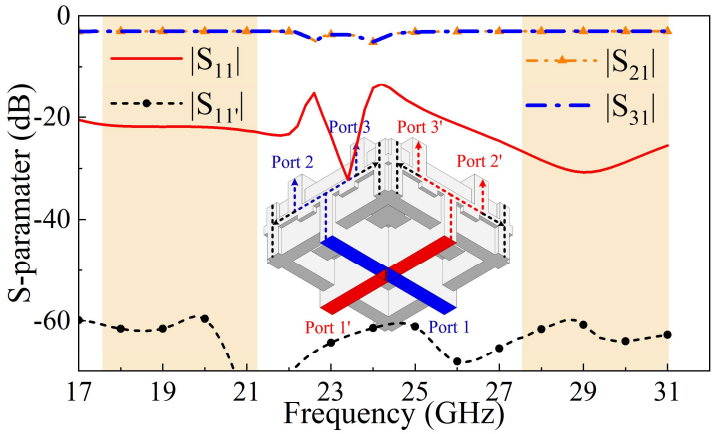


Fig. 5.4. Simulated transmission, reflection and isolation performance of the cross-over structure with bandstop structures.

5.3.3 Evaluation of the maximum allowed frequency ratio

To establish the maximum frequency range enabled by the dual-band bandstop structure under a given array period (d), we set the transmission zero (TZ, between the virtual port A' and C') generated by the high-band bandstop resonator at a highest frequency of 300/d GHz (the grating lobes will appear above this frequency). Both L_{high} and d_1 are set to $\lambda_g/4$, where λ_g represents the guide wavelength in the PPW. Here, L_{high} is the distance from the high-band bandstop resonator to port B', and d_1 is the length of the high-band bandstop resonator.

By adjusting the distance L_{low} of the low-band bandstop resonator to the B' port and its length d_2, the TZ of the low band is changed. According to the reflection matching theory,

when $L_{low}+d_2 = n\cdot\lambda_g/2$ (n = 1, 2, 3...) and $d_2 = n\cdot\lambda_g/4$, the optimal match from A' to B' can be achieved. As $L_{low}+d_2$ increases, the TZ of the low band decreases, thereby expanding the frequency range of the dual-band bandstop structure. Due to the bandwidth limitations of the LSG, we only consider the maximum frequency range under the condition of n = 1. Therefore, under the premise of an equi-period array antenna, the maximum value of L_{low} is half of the radiation period d. By simply adjusting d_2 to align the best impedance matching frequency with the TZ frequency, the maximum frequency ratio can be obtained. Fig. 5.5 shows the variation of the transmission coefficient of the bandstop structure with d_2, given d = 9 mm, L_{high} = 3.2 mm, d_1 = 2.5 mm for high frequency at 33 GHz, and L_{low} = d/2. It can be seen from Fig. 5.5 that when d_2 = 6 mm, L_{low} = 4.5mm, the optimal matching frequency coincides with the optimal blocking frequency at 12.5 GHz. Thus, under the condition where the optimal isolation frequency equals the optimal reflection frequency, the maximum frequency ratio of the bandstop structure is 2.64 (i.e., 33/12.5). In addition, when adjusting d_2, the high-frequency TZ remains stable, whereas additional TZ occur when L_{low} becomes $3\lambda_g/4$. By adjusting L_{low} and d_2, a continuously flexible frequency ratio from 1 to 2.64 can be obtained, shown in Fig. 5.6.

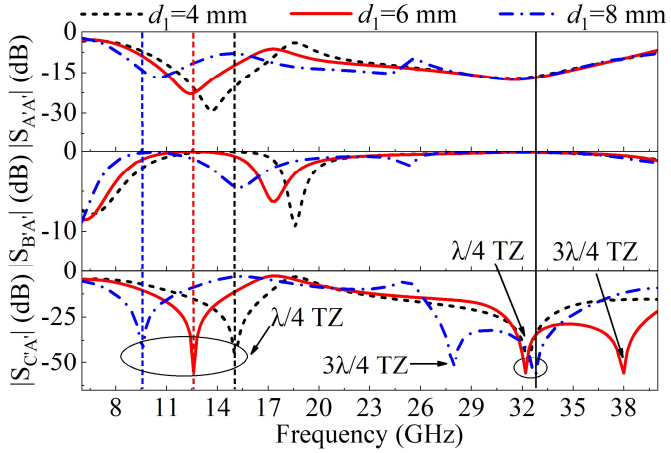


Fig. 5.5. Effect of the bandstop structures: simulated S-parameters at different d_2 with d = 9mm， d_1= 2.5mm, L_{low} =4.5mm and L_{high}=3.2mm.

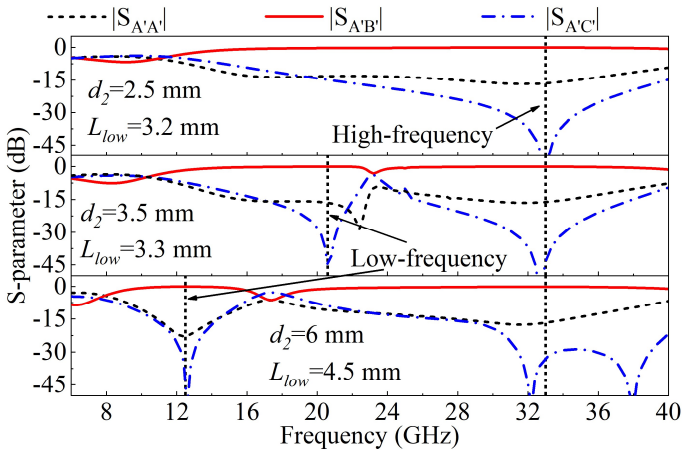


Fig. 5.6. Effect of the bandstop structures: simulated S-parameters at different d_2 and L_{low} with d=9mm， d_1= 2.5mm and L_{high}=3.2mm.

5.4 DESIGN AND SIMULATION

5.4.1 Performance Comparison of the 2×2 Subarrays

Subsequently, based on the analysis, a DBDP waveguide antenna array operating in the K-band (17.7 - 21.2 GHz) and Ka-band (27.5 - 31 GHz) will be designed for SATCOM applications. The antenna element has a periodicity d of 9 mm. The bandstop structure shown in Fig. 5.2(f) is used in the subarray to suppress wave leakage. Fig. 5.7 compares the gain and reflection coefficient of the four subarrays. It is evident that the gain of the dual-polarization Subarray IV nearly matches that of the single-polarization Subarray I, indicating excellent orthogonality due to effective suppression of leakage. On the other hand, Subarray II (without the bandstop structures) exhibits a noticeable decrease in gain. The optimized dimensions of the Subarray IV are: d_1 = 2.05 mm and L_{high} = 3.37 mm for the high band, and d_2 = 3.5 mm and L_{low} = 3.3 mm for the low band, and other details are given in Fig. 5.2(e).

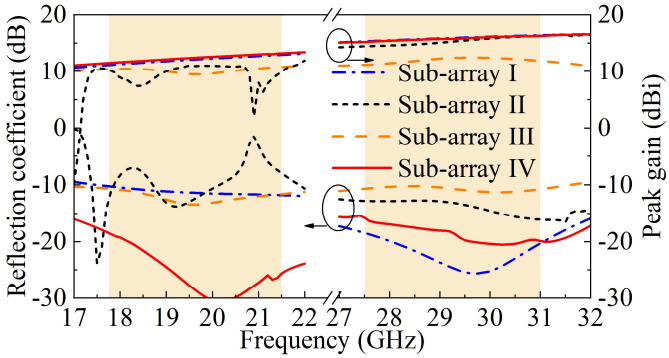


Fig. 5.7. Simulated gain and reflection coefficients of the 4 subarrays in Fig. 5.2.

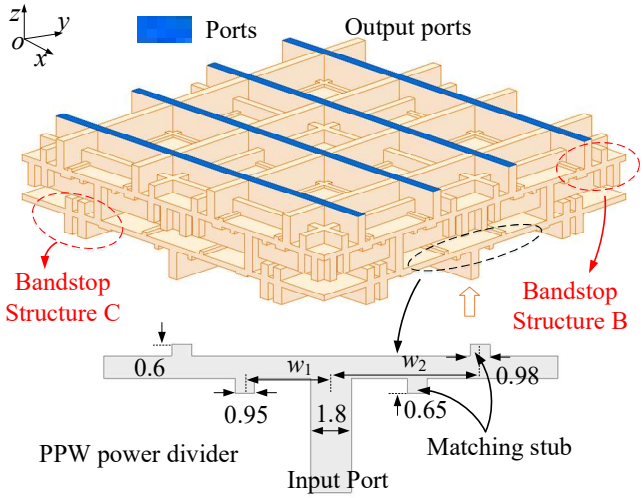


Fig. 5.8. 3D view of the PPW feeding network and a side view of one PPW power divider with matching stubs.

5.4.2 DBDP PPW feeding network

Fig. 5.8 illustrates the overall DBDP PPW feeding network for the 8×8 array, achieved by cascading multiple PPW power dividers into two sets of orthogonal corporate feeding

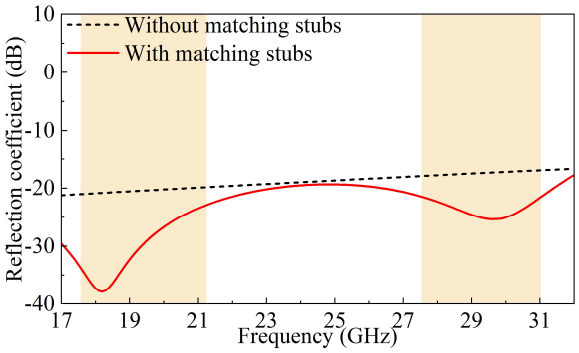


Fig. 5.9. Simulated reflection coefficient of the PPW power divider with/without the small matching stubs.

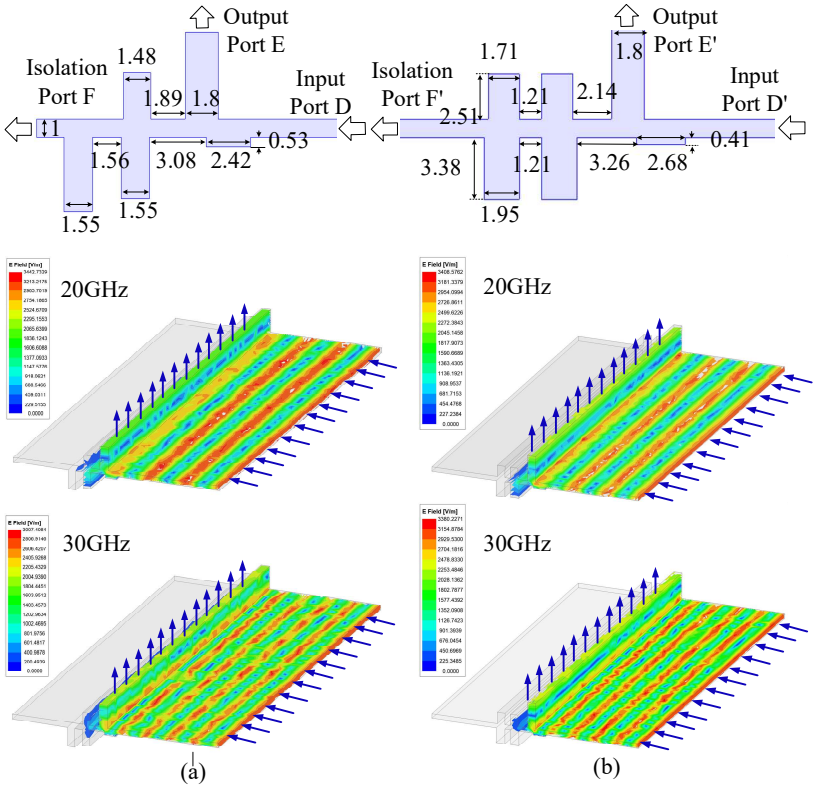


Fig. 5.10. Bandstop structures in the PPW and their electric field distributions at 20 GHz and 30 GHz: (a) Structure B; (b) Structure C.

networks. Each PPW power divider includes two small matching stubs to enhance impedance matching. Fig. 5.9 shows the effect of these stubs, demonstrating that when w_1=3.95 mm and w_2=6.82 mm, the reflection coefficients for both bands are better than -21.4 dB. Fig. 5.10 present two bandstop structures designed to enhance the transmission performance of the dual-polarized PPW feeding network. The electric field distributions at 20 GHz and 30 GHz confirm the effective operation of both bandstop structures. Bandstop structure B differs from bandstop structure A shown in Fig. 5.1, as it uses three stubs to generate more transmission zeros (TZs), thereby enhancing isolation. Bandstop structure C, similar to structure A, employs two identical sets of short-circuit stubs positioned at λ/4 and 3λ/4 from the junction. Although bandstop structure B has better stopband suppression

in the Ka-band, it suffers from higher insertion loss compared to structure C. This is because the second TZ generated by structure C in the Ka-band functions merely as a short-circuit stub and does not meet the optimal reflection matching condition, as demonstrated in the simulation results shown in Fig. 5.11. Bandstop structure B here is used to balance the antenna height. If bandstop structure B were replaced with the design of bandstop structure C, bandstop structures A and B would overlap in the DBDP PPW feeding network (highlighted in the red box in Fig. 5.1). Finally, both methods were used to improve the isolation between the input and isolation ports, which significantly reduces the insertion loss.

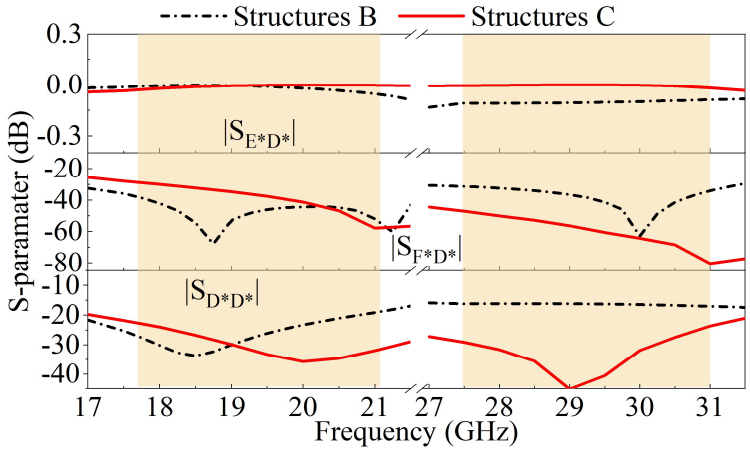


Fig. 5.11. Simulated results of the two bandstop structures in the PPW feeding network.

5.4.3 Orthogonal Line Source Generator (LSG) and in-phase combiners

To excite two orthogonal PPW feeding networks, a cross-orthogonal planar wave source is required. In this design, a multi-port LSG is utilized to generate the planar wave excitation. A conventional approach involves stacking two orthogonally overlapping LSGs to form a cross-polarized planar wave source. However, this would increase the number of feed layers. To achieve a more compact implementation, four multi-port LSGs are sequentially rotated, enabling the realization of an orthogonal dual-polarized feed within a single layer, as illustrated in Fig. 5.12. Each multi-port LSG is excited by a 1-to-4 single-ridge waveguide power divider, where each divider consists of three single-ridge waveguide power dividers. A detailed view of the LSG, including its dimensions, is provided, and the design of the single-polarized LSG has been thoroughly discussed in [12].

When the two diagonal feed networks with the same polarization are simultaneously excited, a quasi-TEM wave will propagate within the PPW, as illustrated in Fig. 5.12(b). A key design consideration is the gap in length L left between the two co-polarized LSGs, which plays a critical role in shaping the amplitude distribution along the line source and influencing the sidelobe level. Fig. 5.13 illustrates the amplitude distribution of the line source and the corresponding radiation patterns at 20 GHz and 30 GHz for different gap lengths. A wider gap enhances port isolation, as demonstrated in Fig. 5.14. However, it also reduces the electromagnetic energy at the center of the line source, which may lead to an increase in sidelobe levels. To achieve an optimal balance between these effects, *L* was set to 4.8 mm.

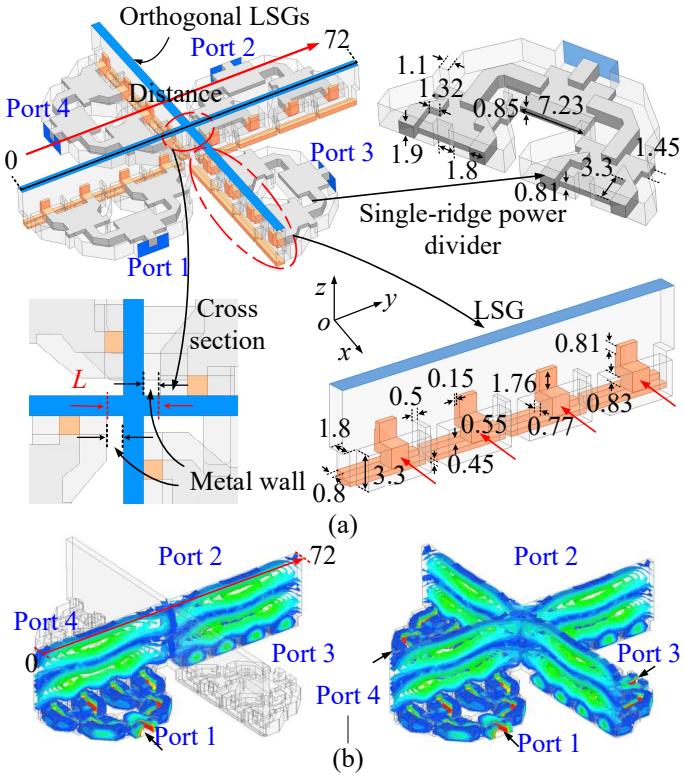


Fig. 5.12. Orthogonal LSGs. (a) 3D view; (b) Simulated quasi-TEM wave propagating in PPWs. All dimensions are given in millimeters.

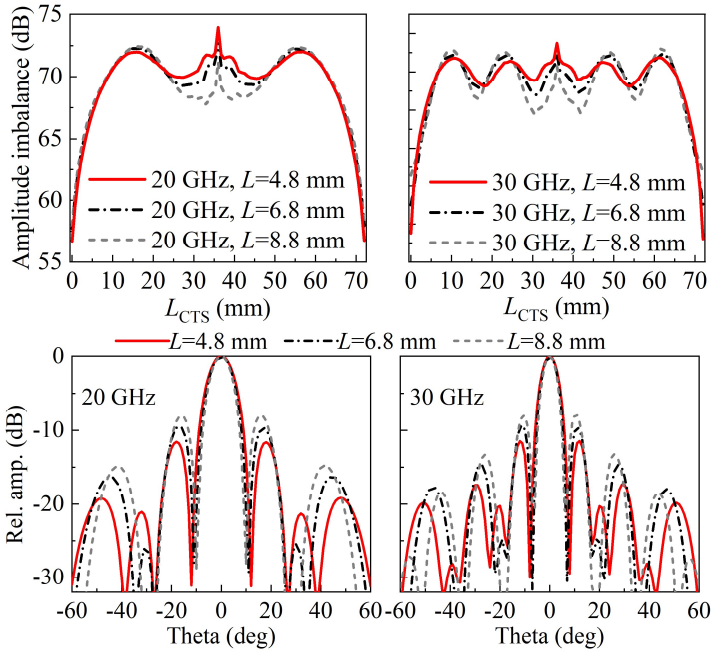


Fig. 5.13. Simulated amplitude distribution along the LSG at 20 and 30GHz with different gap lengths showing different sidelobe characteristics.

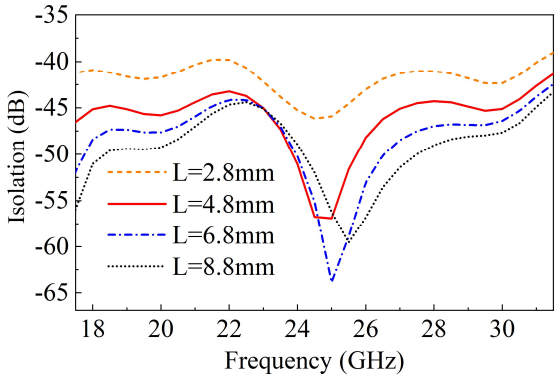


Fig. 5.14. Simulated isolations with different gap lengths.

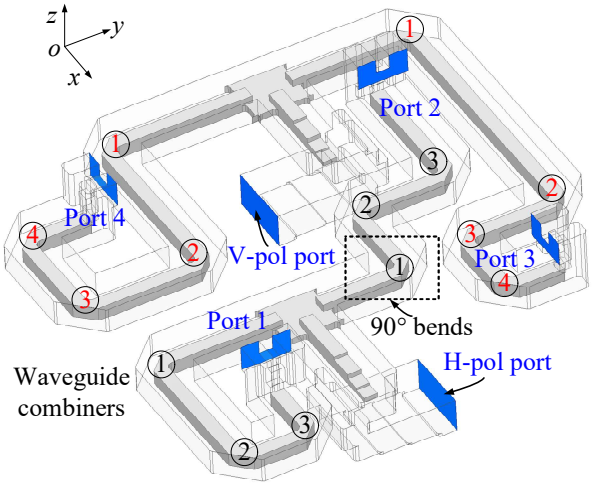


Fig. 5.15. 3D view of the in-phase combiners.

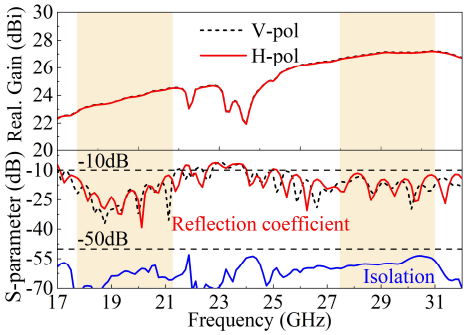


Fig. 5.16. Simulated reflection coefficients and antenna gains of the array

5.4.4 Complete Array Antenna and method for Generating Circular Polarization

The simulated reflection coefficients and gains of the antenna array across both K- and Ka-bands are shown in Fig. 5.16. Across these bands, the reflection coefficients remain below -13 dB, while port isolation exceeds 50 dB. The gain curves for both polarizations are stable within the operating bandwidth, showing no significant fluctuations. For Ka-band SATCOM systems, dual circular polarization (CP) is required. To achieve circular

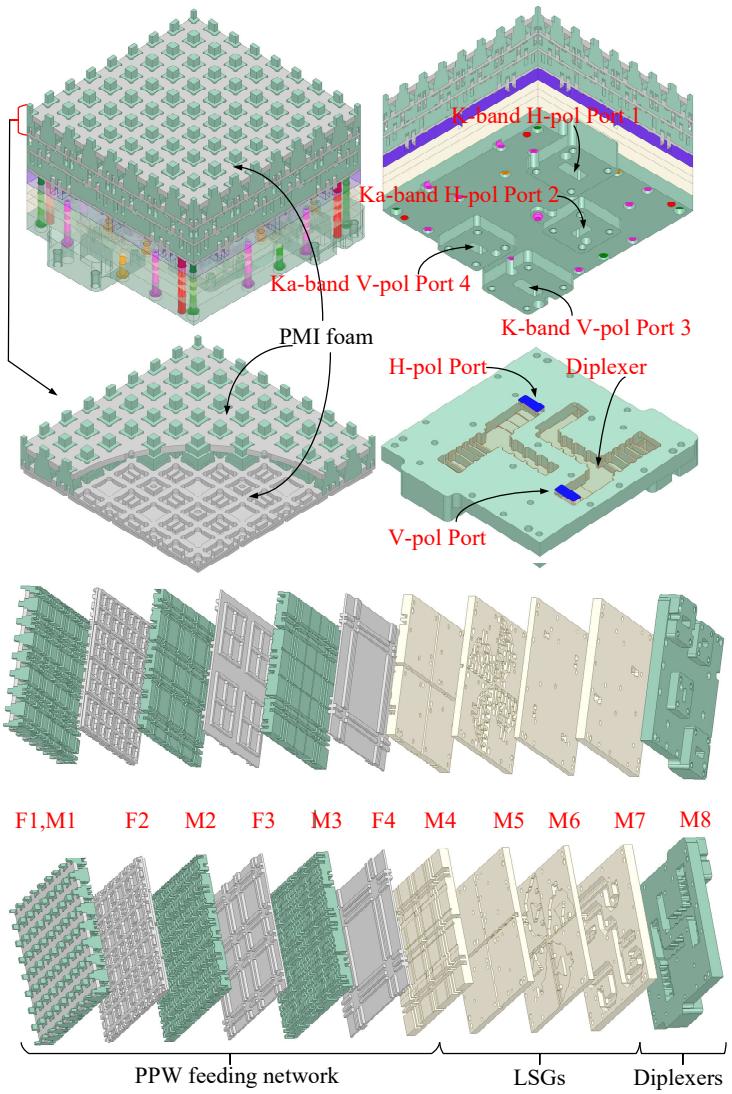


Fig. 5.17. 3D view and exploded view of the antenna assembly, where 'F' stands for the foam interlayer and 'M' for the metal structure.

polarization, a diplexer can be connected at both the horizontal and vertical polarization ports. This setup separates the signals into K- and Ka-bands using WR28 and WR51 standard waveguide ports (Ports 1 to 4), as illustrated in Fig. 5.17. By recombining the Ports 1 and 3 with a 3 dB coupler, circular polarization is generated in the K-band. Similarly, circular polarization for the Ka-band is achieved by cascading a 3 dB coupler after Ports 2 and 4. Since the diplexer is not the primary focus of this work, its detailed analysis will not be included here.

In addition, SATCOM applications require specific radiation masks to avoid interference with other satellites. These masks strictly regulate the radiation pattern envelope. For the antenna presented in this paper, low sidelobe levels in the H-plane and E-plane can be achieved by applying amplitude weighting techniques to the single-ridge waveguide feeding network (H-plane) and the PPW feeding network (E-plane) based on the methods proposed in [39] and [40].

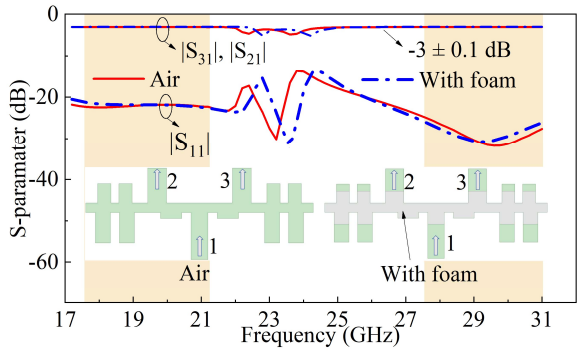


Fig. 5.18. Simulation transmission coefficients with and without PMI foam.

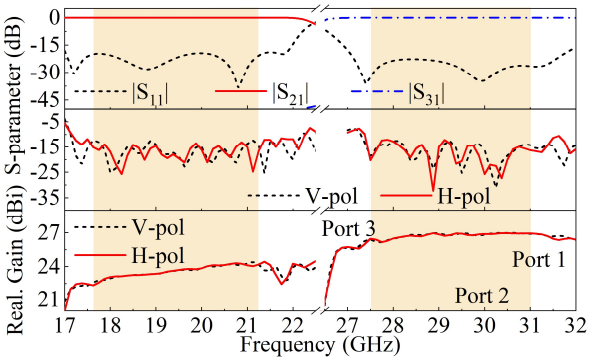


Fig. 5.19. Simulated reflection coefficients and antenna gains of the antenna array cascaded with K/Ka-band duplexers.

The antenna assembly contains multiple layers of suspended structures (PPW feeding networks), as illustrated in Fig. 5.17. CNC-machined low-density PMI foam (ROHACELL® WF71, provided by EVONIK) with locking slots is used not only as structural support but also as a precise alignment mechanism for the layered antenna components. Layers M5 to M8 are assembled using metal screws, while layers M1 to M4 are integrated into a single unit through positioning and assembly using the PMI foam interlayer with locating slots. Finally, these two sections are aligned using locating pins and connected with screws to form the complete structure.

Simulation results show that the PMI foam (with a dielectric constant of 1.05 and a loss tangent of 0.0017) has a negligible effect on the transmission coefficient of the PPW power divider in Fig. 5.18. Fig. 5.19 presents the simulation results for the entire antenna array with diplexers, indicating that the reflection coefficients for all ports are less than -13dB, and the gain varies smoothly with frequency.

5.5 Experimental Verification

This prototype antenna is manufactured out of eight metal layers and four layers of PMI foam, as depicted in Fig. 5.20. Blocks M1 to M8 are CNC milled from 6061 aluminum-magnesium alloy, with a tolerance of 20 μm. In simulations, a nominal conductivity of 3.8×10^7 S/m is applied. Layers F1 to F4 are CNC milled PMI foam. By simulation, Fig. 5.21 illustrates the impact of assembly errors in interlayer spacing of the PPW on insertion loss. It is observed that stable radiation performance can be maintained with an interlayer spacing deviation within ± 200 μm. This tolerance is attributed to the stable impedance-matching performance of the bandstop structures, relaxing the assembly requirements for

the PPW feed network layer. Metal screws have been installed between layers M1 and M4, surrounding the single-ridge waveguide feed network and diplexers, ensuring robust connections. The prototype measures 72 mm × 72 mm × 42 mm. Radiation measurements were carried out using a far-field antenna test system in an anechoic chamber. Reflection coefficients and isolation performance were assessed using an Agilent E8361C network analyzer.

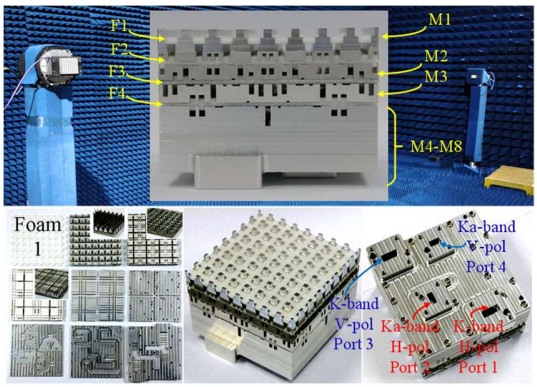


Fig. 5.20. Photographs of fabricated blocks, assembled antenna, and test environment.

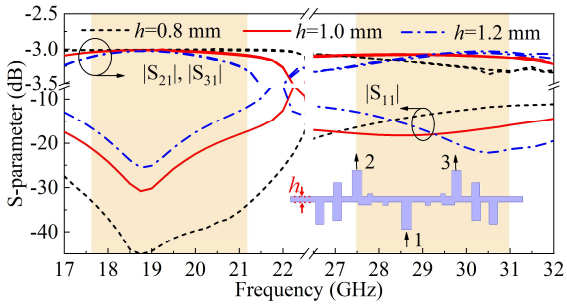


Fig. 5.21. Effect of assembly errors: simulated return loss and insertion loss with different interlayer spacing *h*.

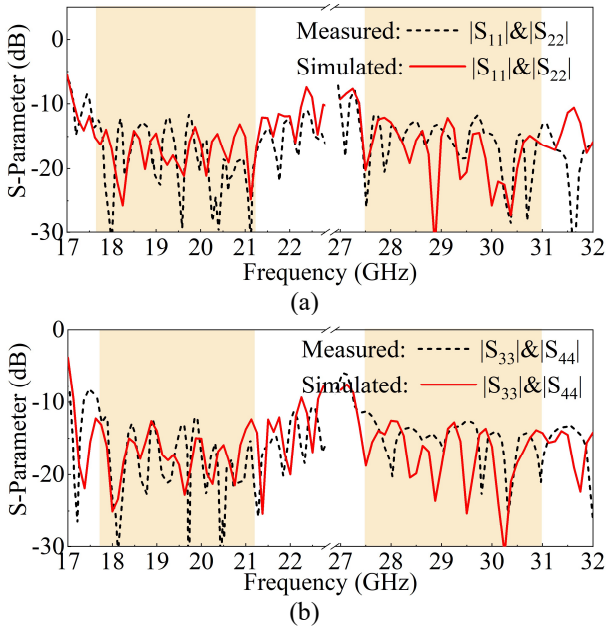


Fig. 5.22. Simulated and measured reflection coefficients. (a) H-pol; (b) V-pol.

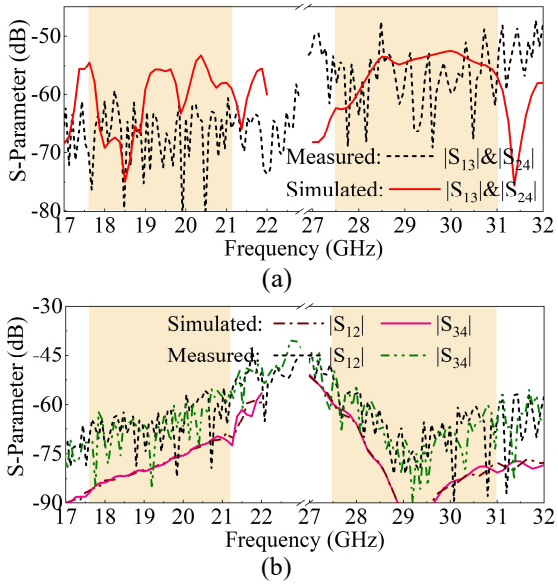


Fig. 5.23. Simulated and measured (a) port isolation between different polarization ports operating at the same frequency; (b) port isolation between same polarization ports operating at different frequencies.

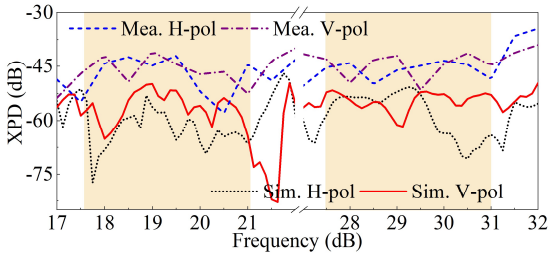


Fig. 5.24. Simulated and measured XPDs.

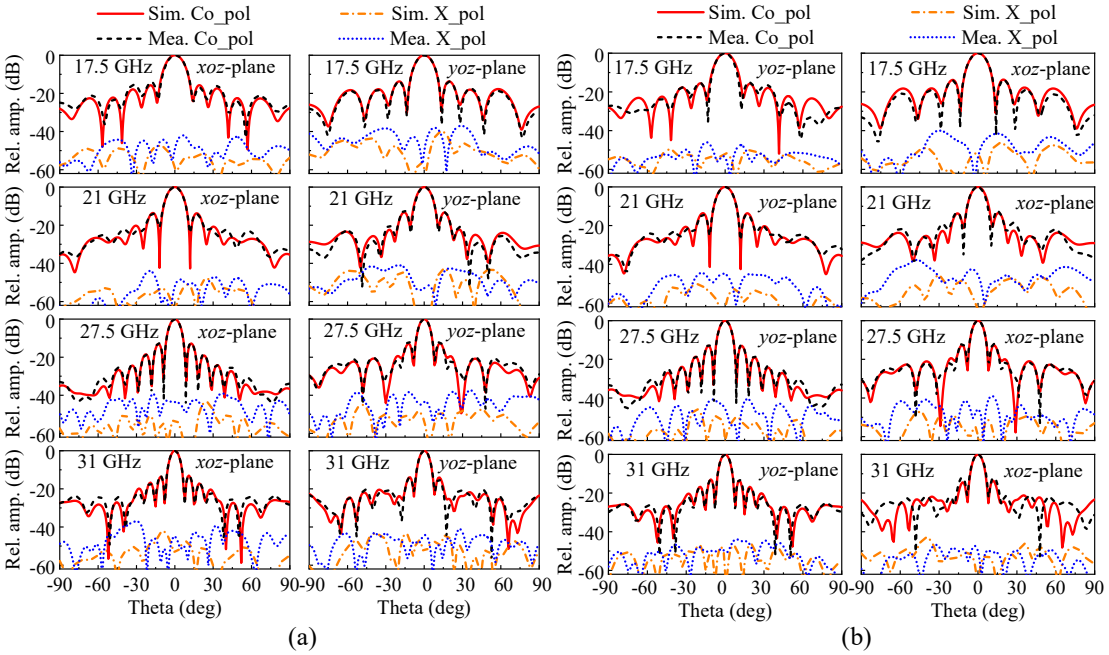


Fig. 5.25. Simulated and measured results: (a) V-pol normalized radiation patterns and (b) H-pol normalized radiation patterns.

5.5.1 Reflection Coefficient and Port Isolation

Port reflection coefficients and transmission coefficients are measured. When two ports are connected for testing, the other two are terminated with matching loads. Fig. 5.21(a) and (b) show the simulated and measured reflection coefficients for the H- and V-polarization. The measured fractional bandwidth is 18% (17.7 – 21.2 GHz) for the K-band and 12% (27.5 – 31.0 GHz) for Ka-band. The simulated and measured data demonstrate good consistency. Fig. 5.23(a) illustrates that the measured isolation between port 1 and port 3, as well as port 2 and port 4, exceeds 45 dB. Furthermore, the port-to port isolation $|S_{21}|$ and $|S_{43}|$ surpass 60 dB in both the K-band and Ka-band, as shown in Fig. 5.23(b). Benefiting from the high polarization isolation of orthogonal PPW, the measured XPDs in both bands are better than 40 dB (Fig. 5.24).

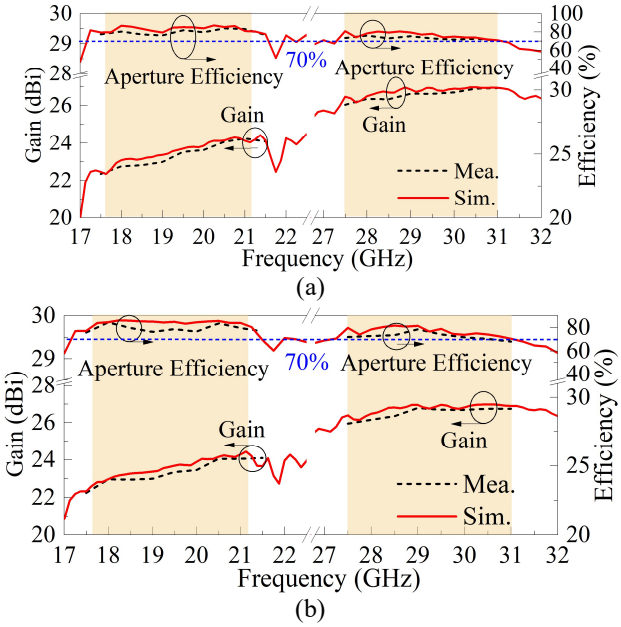


Fig. 5.26. Simulated and measured antenna peak gain and aperture efficiency: (a) H- pol; (b) V-pol.

5.5.2 Radiation patterns and Efficiency

Fig. 5.25 presents the normalized radiation patterns, both simulated and measured, at 17.5GHz，21GHz, 27.5GHz and 31 GHz. These patterns exhibit stability across the entire frequency band and closely align with the simulation results. The first SLLs are around -13.1 dB, which is expected from a square array excited by constant amplitude and phase.

Fig. 5.26 illustrates the simulated and measured peak gain and aperture efficiency. In both H- and V-polarizations, the measured peak gains in the K-band are between 22.3 to 24.2 dBi and 22.2 to 24.1 dBi, while in the Ka-band, they range from 26.0 to 26.9 dBi and 25.9 to 26.8 dBi. The simulated values for the K-band falls within the range of 22.7 - 24.5 dBi and 23.0 - 24.5 dBi, while the Ka-band, ranges from 26.3 - 27.1 dBi and 26.3 - 27.2 dBi. The minor difference of about 0.5 dB is primarily attributed to fabrication tolerances, assembly, and measurement errors. The aperture efficiencies of the two polarizations exceed 78.0% and 70.0% in the K-band and Ka-band, respectively. Notably, the measured

TABLE I
PERFORMANCE COMPARISON OF DUAL-POLARIZED ANTENNAS FOR SATCOM APPLICATIONS

Ref.	Element type	No. Layers	Frequency range (GHz)/ FBW (%)	Polarization	Gain[1] (dBi)	Aperture efficiency (%)	Radiation efficiency (%)	XPD (dB)	Thikness (λ_0^2)	Meet Ka-band Satcom bandwidth requirements
[18]	Corporate feed CTS+polarizer	10	18.7-20.7/9.47 28.2-30/4.42	Orthogonal - circular	16.5 19.7	N. A	50.9 39.9	>35 >30	5.8	No
[25]	Corporate feed Horn	7	19-30GHz / 45%	Dual-circular	27	>80	N. A	>30	4.5	No
[30]	Corporate feed Cross-strips	8	14.4-17.5/19.4 32.5-35/7.4	Dual-linear Dual-circular	18.4 23.4	>60 >50	N. A N. A	>15 >15	4.8	No
[31]	Corporate feed slot	3	19.7-21.5/8.8 29-31/6.7	Orthogonal - linear	26 29.5	N. A	N. A N. A	>30	N. A	No
[36]	Series feed Orthogonal CTS	4	17.5-20/13.3 28.5-30/5.1	Dual-linear Dual-linear	24	>70 >70	>90 >85	>27	1.6	No
This work	Corporate feed Orthogonal CTS	12	17.7-21.2/18 27.5-31/12	Dual-linear Dual-linear	23.8 26.3	>78 >70	>87 >85	>40 >40	3.4	Yes

[1]The values are obtain at the center frequency.[2]The values are obtain at the center frequency.

aperture efficiency η_{mea_ap} is calculated using the following equations:

$$\eta_{mea_ap} = \frac{G_{mea}\lambda^2}{4\pi A}$$

where G_{mea} is the measured peak gain, λ is the free-space wavelength corresponding to the operating frequency, and A is the aperture area of the antenna.

5.5.3 Comparison

Table I shows the comparison between the proposed antenna and other published DBDP waveguide antennas. Most of the designs, such as slot arrays and CTS arrays, are adopted in the design of dual-band arrays. Most of these designs, such as [18]and [31], achieve only one polarization in one frequency band. The design in [25] attempts to use an ultra-wideband dual circularly polarized array to cover the transmit and receive bands. However, its operational bandwidth of 19–30 GHz still falls short of the full bandwidth requirements for Ka-band SATCOM. [30] introduces a novel DBDP waveguide array antenna, which combines a septum polarizer with an OMT to achieve DBDP with a shared aperture. The array spacing in the high-frequency band is about 1.4·λ. Although introducing cross-strip and cross-patch structures improves the sidelobe levels to some extent, the measured aperture efficiency at the high-frequency end is only about 50%. Additionally, all the aforementioned designs are optimized for specific frequency ratios and suffer from relatively large periodic spacing which leads to the emergence of grating lobes. Series-fed dual-band CTS antennas reported in [36] offer a low-profile design with no significant grating lobes. However, the long-line effects caused by dispersion mean these antennas usually operate over a very narrow frequency band.

Compared with the references listed in Table I, the proposed DBDP array has the advantages of dual polarization at both bands, wide bandwidth, no grating lobes, high aperture efficiency, and radiation efficiency, making it highly competitive in SATCOM applications.

5.6 Conclusion

Previous efforts in developing DBDP waveguide antenna arrays for Ku/Ka-band were limited by the bandwidth and the achievable frequency ratio between the dual bands. This work overcomes these limitations using orthogonal CTS arrays with DBDP PPW corporate feeding networks and bandstop structures to suppress the leakage between polarization and to adjust the frequency band ratio (up to to 2.64:1). We have demonstrated a DBDP waveguide array with a fractional bandwidth of over 18% in the K-band and over 12% in the Ka-band. The prototype demonstrates excellent performance in terms of bandwidth, isolation, and XPD. Its high efficiency, stable radiation patterns, and flexible frequency ratio adjustment further enhance its practicality and adaptability for diverse SATCOM applications. The antenna design, validated through both simulation and experimental results, shows great potential for advanced SATCOM systems.

References

[1] C. Granet, J. S. Kot and J. Ness, "Wideband Ka-band SATCOM-on-the-move antenna concept: preliminary design study," in *Proc. 13th Eur. Conf. Antennas and Propagation (EuCAP)*, 2019, pp. 1-5.

[2] T. Chaloun et al., "Electronically Steerable Antennas for Future Heterogeneous Communication Networks: Review and Perspectives," *IEEE Journal of Microwaves*, vol. 2, no. 4, pp. 545-581, Oct. 2022.

[3] "Commercial IFC Antennas," ThinKom, https://www.thinkom.com/commercial-ifc-antennas#ThinAir_Plus (accessed Dec. 7, 2024).

[4] F. Hasselmann and L. Felsen, "Asymptotic analysis of parabolic reflector antennas," *IEEE Trans. Antennas Propag*., vol. 30, no. 4, pp. 677-685, July. 1982.

[5] S. K. Rao, "Parametric design and analysis of multiple-beam reflector antennas for satellite communications," *IEEE Antennas Propag*. Mag., vol. 45, no. 4, pp. 26-34, Aug. 2003.

[6] C. Han, C. Rodenbeck, J. Huang and K. Chang, "A C/Ka dual frequency dual Layer circularly polarized reflectarray antenna with microstrip ring elements", *IEEE Trans. Antennas Propag*., vol. 52, no. 11, pp. 2871-2876, Nov. 2004.

[7] F. Greco, L. Boccia, E. Arnieri, and G. Amendola, "K/Ka-band cylindrical reflector antenna for compact satellite Earth terminals," *IEEE Trans. Antennas Propag*., vol. 67, no. 8, pp. 5662–5667, Aug. 2019.

[8] Z. H. Jiang, T. Yue and W. Hong, "Low-profile and wideband dual-circularly polarized reflect-arrays based on rotated metal-backed dual-polarized aperture-coupled patch elements," *IEEE Trans. Antennas Propag*., vol. 68, no. 3, pp. 2108-2117, Mar. 2020.

[9] V. Ravindra, P. R. Akbar, M. Zhang, J. Hirokawa, H. Saito and A. Oyama, "A Dual-Polarization X -Band Traveling-Wave Antenna Panel for Small-Satellite Synthetic Aperture Radar," *IEEE Trans. Antennas Propag*., vol. 65, no. 5, pp. 2144-2156, May 2017.

[10] Z. Shi-Gang, H. Guan-Long, P. Zhao-hang and L.-J. Ying, "A wideband full-corporate-feed waveguide slot planar array", *IEEE Trans. Antennas Propag*., vol. 64, no. 5, pp. 1974-1978, May. 2016.

[11] T. Zhang, R. Tang, L. Chen, S. Yang, X. Liu and J. Yang, "Ultra-wideband full-metal planar array antenna with a combination of ridge gap waveguide and E-plane groove gap waveguide", *IEEE Antennas Wireless Propag*. Lett., vol. 70, no. 9, pp. 8051-8058, Sep. 2022.
[12] Q. You, Y. Lu, Y. You, Y. Wang, Z.-C. Hao and J. Huang, "Wideband full-corporate-feed waveguide continuous transverse stub antenna array", *IEEE Access*, vol. 6, pp. 76673-76681, 2018.
[13] M. Huang, Y. Lu, Q. You, J. Xu and J. Huang, "High-Efficiency Full-Metal Planar Slot Array Antenna With Over 60% Bandwidth," *IEEE Antennas Wireless Propag*. *Lett*., vol. 22, no. 5, pp. 1124-1128, May. 2023.
[14] J. I. Herranz-Herruzo, A. Valero-Nogueira, M. Ferrando-Rocher, B. Bernardo, A. Vila and R. Lenormand, "Low-Cost Ka-band Switchable RHCP/LHCP Antenna Array for Mobile SATCOM Terminal," *IEEE Trans. Antennas Propag*., vol. 66, no. 5, pp. 2661-2666, May 2018.
[15] P. Naseri, S. A. Matos, J. R. Costa, C. A. Fernandes and N. J. G. Fonseca, "Dual-band dual-linear-to-circular polarization converter in transmission mode application to K/Ka-Band satellite communications," *IEEE Trans. Antennas Propag*., vol. 66, no. 12, pp. 7128-7137, Dec. 2018.
[16] H. B. Wang and Y. J. Cheng, "Single-layer dual-band linear-to-circular polarization converter with wide axial ratio bandwidth and different polarization modes," *IEEE Trans. Antennas Propag*., vol. 67, no. 6, pp. 4296-4301, Jun. 2019.
[17] M. A. Sofi, K. Saurav and S. K. Koul, "Frequency-Selective Surface-Based Compact Single Substrate Layer Dual-Band Transmission-Type Linear-to-Circular Polarization Converter," *IEEE Trans. Microw. Theory Techn*., vol. 68, no. 10, pp. 4138-4149, Oct. 2020.
[18] M. Del Mastro et al., "Ultra-low-profile continuous transverse stub array for SATCOM applications", *IEEE Trans. Antennas Propag*., vol. 70, no. 6, pp. 4459-4471, Jun. 2022.
[19] Y. Cheng and Y. Dong, "Wideband dual-polarized gap waveguide antenna array based on novel 3-D-printed feeding-network topologies," *IEEE Trans. Antennas Propag*., vol. 71, no. 2, pp. 1493-1505, Feb.2023.
[20] Q. You, Y. Wang, M. Huang, J. Huang, Z. -W. Zheng and Y. Lu, "Wideband Dual-Polarized Hollow-Waveguide Slot Array Antenna," *IEEE Trans. Antennas Propag*., vol. 70, no. 10, pp. 9326-9336, Oct. 2022.
[21] Q. You, Y. Lu, M. Huang, J. Xu and J. Huang, "High-efficiency airfilled wideband ±45° dual-polarized slot array antenna," *IEEE Trans. Antennas Propag*., vol. 71, no. 5, pp. 4582-4587, May 2023.
[22] Y. Hu, Y. Lu, K. Zhou, Q. You and J. Huang, "Wideband Hollow-Waveguide Dual-Polarized Antenna With Reduced Metal Layers," *IEEE Trans. Antennas Propag*., vol. 72, no. 1, pp. 1027-1032, Jan. 2024.
[23] Y. Lu, S. Shen, Y. You, J. Xu and J. Huang, "Wideband Dual Linearly Polarized Hollow- Waveguide Septum Antenna Array for Ku-Band Satellite Communications," *IEEE Trans. Antennas Propag*., vol. 71, no. 3, pp. 2433-2442, March 2023.
[24] F. Sun, Y. Li, J. Wang, Y. Ma, L. Ge, B. Ai and R.He, "A millimeter-wave wideband dual-polarized antenna array with 3-D-printed air-filled differential feeding cavities," *IEEE Trans. Antennas Propag*., vol. 70, no. 2, pp. 1020-1032, Feb. 2022.

[25] H. Zhao, P. F. Gu, Z. H. Fan, Z. He, J. Cao, X. Tao, J. X. Wang, D. Z. Ding, "Ultrawideband Dual Circularly Polarized Waveguide Array Antenna for K- and Ka-Bands Satellite Communications", *IEEE Antennas Wireless Propag*. Lett., vol.22, no.8, pp.1808-1812, 2023.
[26] Yilin Dong, Rong Xu, Yu-Hang Yang, Shi-Gang Zhou, "Compact Shared-Aperture Dual-Band Dual-Circularly-Polarized Waveguide Antenna Array Operating at K/Ka-Band", *IEEE Trans. Antennas Propag*., vol.71, no.1, pp.443-449, 2023.
[27] J. Zhang, X. Li, Z. Qi, Y. Huang and H. Zhu, "Dual-Band Dual-Polarization Horn Antenna Array Based on Orthomode Transducers with High Isolation for Satellite Communication," *IEEE Trans. Antennas Propag*., vol. 70, no. 10, pp. 9247-9259, Oct. 2022.
[28] M. Ferrando-Rocher, J. I. Herranz-Herruzo, A. Valero-Nogueira and M. Baquero-Escudero, "Dual-Band Single-Layer Slot Array Antenna Fed by K/Ka-Band Dual-Mode Resonators in Gap Waveguide Technology,|" *IEEE Antennas Wireless Propag*. Lett., vol. 20, no. 3, pp. 416-420, March 2021.
[29] J. F. Zhang and Y. J. Cheng, "Ka-/W-band shared-aperture antenna array based on stacked continuous transverse stub," *IEEE Trans. Antennas Propag*., vol. 70, no. 12, pp. 11665-11674, Dec. 2022.
[30] J. Ran, Y. Wu, C. Jin, P. Zhang and W. Wang, "Dual-Band Multipolarized Aperture-Shared Antenna Array for Ku-/Ka-Band Satellite Communication," *IEEE Trans. Antennas Propag*., vol. 71, no. 5, pp. 3882-3893, May 2023.
[31] M. Ferrando-Rocher, J. I. Herranz-Herruzo, A. Valero-Nogueira and B. Bernardo-Clemente, "Full-metal K-Ka dual-band shared-aperture array antenna fed by combined ridge-groove gap waveguide," *IEEE Antennas Wireless Propag*. Lett., vol. 18, no. 7, pp. 1463-1467, Jul. 2019.
[32] M. Ettorre, F. F. Manzillo, M. Casaletti, R. Sauleau, L. Le Coq, and N. Capet, "Continuous transverse stub array for Ka-band applications," *IEEE Trans. Antennas Propag*., vol. 63, no. 11, pp. 4798–4800, Nov. 2015.
[33] Y. Lu, Q. You, Y. Wang, Y. You, J. Huang and K. Wu, "Millimeter-Wave Low-Profile Continuous Transverse Stub Arrays With Novel Linear Source Generators," *IEEE Trans. Antennas Propag*., vol. 67, no. 2, pp. 988-997, Feb. 2019.
[34] Q. You, Y. Lu, Y. Wang, J. Xu, J. Huang and W. Hong, "Hollow-Waveguide Tri-Band Shared-Aperture Full-Corporate-Feed Continuous Transverse Stub Antenna," *IEEE Trans. Antennas Propag*., vol. 70, no. 8, pp. 6635-6645, Aug. 2022.
[35] J. F. Zhang, Y. J. Cheng and Y. R. Ding, "An S- and V-Band Dual-Polarized Antenna Based on Dual-Degenerate-Mode Feeder for Large Frequency Ratio Shared-Aperture Wireless Applications," *IEEE Trans. Antennas Propag*., vol. 68, no. 12, pp. 8127-8132, Dec. 2020.
[36] Q. -C. Ye, Y. -M. Zhang, J. -L. Li, G. F. Pedersen and S. Zhang, "High-Isolation Dual-Polarized Leaky-Wave Antenna with Fixed Beam for Full-Duplex Millimeter-Wave Applications," *IEEE Trans. Antennas Propag.,* vol. 69, no. 11, pp. 7202-7212, Nov. 2021.
[37] M. Śmierzchalski, F. F. Manzillo, M. D. Mastro, N. Capet, B. Palacin, R. Sauleau and M. Ettorre, "A Novel Dual-Polarized Continuous Transverse Stub Antenna Based on Corrugated Waveguides—Part I: Principle of Operation and Design," *IEEE Trans. Antennas Propag*., vol. 69, no. 3, pp. 1302-1312, March 2021.

[38] M. Śmierzchalski, F. F. Manzillo, M. D. Mastro, N. Capet, B. Palacin, R. Sauleau and M. Ettorre, “A Novel Dual-Polarized Continuous Transverse Stub Antenna Based on Corrugated Waveguides—Part II: Experimental Demonstration,” *IEEE Trans. Antennas Propag*., vol. 69, no. 3, pp. 1313-1323, March 2021.

CHAPTER 6: ULTRA-WIDEBAND LOW-PROFILE WAVEGUIDE ANTENNA ARRAY WITH HIGH APERTURE EFFICIENCY

Qingchun You, Yi Wang

Yi Wang proposed, organized, and oversaw the entire study, taking the lead on the project. Qingchun You originated the design concept, conducted the theoretical modeling, analysis, simulations, carried out the experiments, interpreted the results, and drafted the manuscript. Both authors contributed to the writing of the paper and reviewed the final manuscript.

This chapter is based on the following under-review paper: Q. You and Y. Wang, "Ultra-Wideband, Low-Profile Waveguide Antenna Array with High Aperture Efficiency," *IEEE Trans Antennas Propag*., Submit in February 2025, Under review.

Abstract

This paper presents an ultra-wideband low-profile full metal waveguide antenna array design. The key innovations include the quasi-TEM mode radiators, the ultra-wideband rectangular coaxial-to-ridge waveguide transition, and the in-phase air-filled corporate feed network based on rectangular coaxial lines. The prototype achieves a fractional bandwidth of 105% over the 10–32 GHz range, with an aperture efficiency above 82% and a height of only 0.3 wavelengths at the lowest frequency. The antenna structure is fully metal and manufactured using CNC machining, with laser cutting employed for the coaxial core layer. Experimental results show excellent agreement with simulations. The proposed design can find applications in SATCOM and other wideband point-to-point communication systems.

Keywords: Wideband antenna array, Low profile, High aperture efficiency, Rectangular coaxial line, Quasi-TEM radiator.

6.1 Introduction

With the development of multi-band multi-functional wireless communication systems, antennas are increasingly required to support multiple operating frequency bands. For example, the bands of 6/7/8/11/13/15/18/23/60/70/80 GHz have been allocated to point-to-point backhaul links [1], [2]. Ku (10.7 - 14.5 GHz), K (17.7 - 21.2 GHz) and Ka (27.5 - 31 GHz) bands have already been widely used in SATCOM [3], [4]. Ultra-wideband high-gain antennas with uncompromising efficiency are highly desired for these application scenarios. A low-profile antenna would also be an advantage for SATCOM to integrate it into a variety of moving platforms, such as aircraft and trains.

Microstrip line and substrate-integrated waveguide are the common choice in wideband array antennas [5]-[10]. However, their dielectric losses are significant in the mmW region. This would become unacceptable in the design of high-gain array antennas. Hollow-waveguide (HW) based slot/horn array antenna is a better way to achieve high efficiency and high gain [11]-[19]. To realize the wideband characteristics, a full-corporate-feed structure is usually preferred. There are two approaches to achieving wideband feeding. The first involves using a 1-to-4 cavity-backed structure, as demonstrated in [11]-[16]. For example, in [16], a 3D-printed design using the 1-to-4 cavity-backed structure reached a fractional bandwidth (FBW) of 48%. This is the broadest bandwidth reported so far for slot array antennas with back cavities. However, the large unit cell periodicity used in the array led to grating lobes at higher frequencies. The other approach for corporate-feed slot array antennas removes the cavity-backed layer but uses direct one-to-one connection between the feed network and the radiating slots [17]-[19]. In [17], a gap waveguide-based wideband planar array achieved a FBW of 46.8% by incorporating a one-to-one excited double-ridge radiating slot. However, the unit cell periodicity still introduced grating lobes, reducing the aperture efficiency to only 50% at the higher bands. In [18], a one-to-one exciting array antenna, fabricated using 3D printing, achieved a 51% bandwidth. Nonetheless, grating lobes still presented a problem with the design.

All the published waveguide slot array antennas, representing the state-of-the-art in terms of bandwidth, face the issue of grating lobes and aperture efficiency degradation at higher frequencies. In fact, this stems from an inherent trade-off, because reducing unit cell periodicity (to suppress grating lobes) typically results in increased cutoff frequency of transmission waveguide and radiator, which in turn limits the bandwidth.

Continuous transverse stub (CTS) antennas are very capable of achieving wideband and high-gain characteristics [20]-[27], benefiting from the fact that the transmission mode in their parallel-plate waveguide (PPW) is the TEM mode, with inherently large bandwidth. This avoids the bandwidth limitations imposed by the cutoff frequency of the dominant TE10 mode typically encountered in slot or horn array antennas. In [22], a parabolic reflector-based linear source generator (LSG) was combined with a vertical PPW power divider to realize wideband performance. However, the LSG restricted the FBW to 42%. The amplitude distribution of the generated quasi-TEM wave typically follows a tapering distribution, which also decreases the aperture efficiency. Additionally, the vertical PPW power divider network complicates the array scaling. The antenna profile height reaches $3.5 \cdot \lambda$ at the lowest frequency. An ultra-low-profile CTS array was introduced in [23], where multilayer PCB technology was used, incorporating nine dielectric substrates. The antenna height is approximately $0.3 \cdot \lambda$ at the lowest frequency, with a FBW exceeding 50%. It also provides multibeam radiation for polar angles up to ±22.5° in the H-plane. However, the

dielectric losses reduced its aperture efficiency, which is below 50.9%. More recently, CTS antennas fed by multi-port excited LSGs have demonstrated even wider bandwidth and higher aperture efficiency [25]-[27]. For example, [25] reported a fully corporate-fed, full-metal CTS antenna with an FBW of 62% and an aperture efficiency of over 84%. The antenna height is approximately 1.2·λ at the lowest frequency.

The use of TEM radiators offers wideband capability. This must be matched by the feeding network. TE-mode waveguide feed would curtail the bandwidth. Coaxial lines, however, are superior alternative due to their compact size and broad bandwidth, and particularly suitable for one-to-one excitation. A coaxial based feeding network not only allows for a smaller unit cell period but also extends the cutoff frequency to much lower frequency ranges. However, implementing such a network brings its own set of challenges: e.g. how to transit from the coaxial line to the TEM radiator; and how to implement direct one-to-one excitation.

This paper introduces a novel design concept for ultra-wideband planar antennas, where the corporate feed network directly excites the quasi-TEM radiators in a one-to-one configuration. Three key design features are proposed: (1) a quasi-TEM mode radiator excited by a dual-ridge waveguide; (2) an ultra-wideband rectangular-coaxial-to-ridge-waveguide transition, and (3) an ultra-wideband corporate feed network based on air-filled rectangular coaxial line. The antenna module achieves a bandwidth of 105% (10-32 GHz), an aperture efficiency up to 90%, and a low profile of only 0.3·λ at the lowest frequency.

This paper is organized as follows: Section II presents the antenna architecture, while Section III describes the design details of the Quasi-TEM radiator. Section IV covers the design and performance of the complete antenna array. Section V reports the experimental results. Finally, the conclusions are drawn in Section VI.

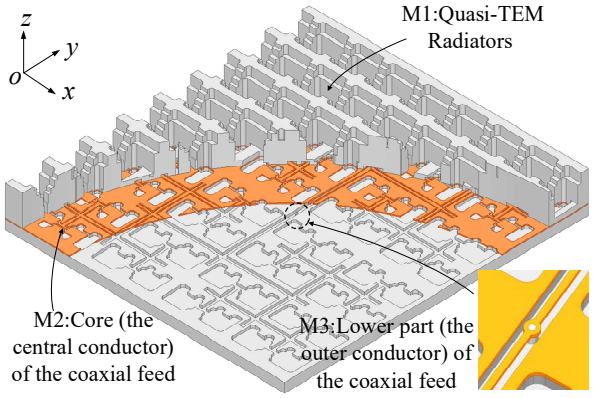


Fig. 6.1 Configuration of the proposed antenna array.

6.2 Overview of Antenna Configuration

Fig. 6.1 shows a schematic of the proposed waveguide antenna array. It has three main sections: the quasi-TEM radiators, the rectangular coaxial-to-double-ridge waveguide transitions, and the corporate feed network. The antenna is fabricated in three layers: M1, M2, and M3. M1 contains the radiating elements and the upper part (the outer conductor) of the coaxial feed, while M2, a 0.2 mm thick layer, forms the core (the central conductor) of the coaxial feed. M3 holds the lower part (the outer conductor) of the coaxial feed and the 50Ω coaxial input port on the backside. Details of the key components will be elaborated next.

6.3 Wideband Antenna Element – Design Theory

This section first details the evolution from traditional TE10 mode radiators to TEM mode radiators, followed by an in-depth analysis of the proposed quasi-TEM mode radiator. The periodicity of the radiating unit cells is determined by analyzing the near-field amplitude distribution. The limiting factors for extending the bandwidth towards lower frequencies at this periodicity are then thoroughly examined, and the tradeoff among bandwidth, profile and aperture efficiency is discussed. Finally, the detailed design process is provided. All analyses are conducted with a preset peak frequency of 31 GHz.

6.3.1 Evolution from TE10 to Quasi-TEM Mode Radiator

In the design of low-profile high-gain array antennas, horn and slot antennas are commonly utilized as radiating elements, as depicted in Fig. 6.2(a). However, their radiation bandwidth is often constrained by the cutoff frequency of the TE_{10} mode. To address this limitation and extend the bandwidth to lower frequencies, ridge waveguides are frequently employed due to their broader dominant mode bandwidth. To achieve impedance matching with free space (377Ω), the ridge waveguide is gradually transitioned into a rectangular waveguide. This transition is essential because the characteristic impedance of a ridge waveguide is significantly lower than that of a rectangular waveguide of the same dimensions. Although incorporating ridge waveguides effectively broadens the bandwidth at the feed port, the overall radiation bandwidth is still limited by the cut-off frequency of radiating elements.

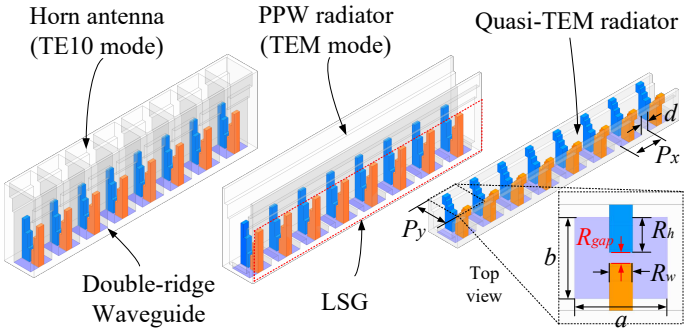


Fig. 6.2 Evolution from TE10 Mode radiator to Quasi-TEM mode radiator. (a) Slot/Horn antenna (FBW:51% [18]); (b) CTS antenna fed by multi-port excited LSG (FBW:62% [25]); (c) Proposed array with Quasi-TEM radiators (FBW:105%, this work).

To further extend the bandwidth, a more advanced approach involves using a LSG structure to convert the TE_{10} mode in a double-ridge waveguide to the TEM mode in a parallel-plate waveguide (PPW). This conversion is followed by a multi-stage impedance transformer [21], which cascaded to the PPW to achieve impedance matching with free space, as shown in Fig. 6.2(b). This method effectively addresses the bandwidth limitations imposed by the cutoff frequency of the radiation slots. However, it introduces challenges for applications requiring low-profile antennas, such as those in aerospace or automotive radar systems, due to the added complexity and potential increase in the profile height.

To reduce the profile, the LSG is integrated with the impedance transformer to form a quasi-TEM radiator, as proposed in this paper and shown in Fig. 6.2(c). This unified

approach not only minimizes the profile height but also enhances impedance-matching bandwidth by enabling smoother transitions within the matching network.

6.3.2 Bandwidth limit factors of the quasi-TEM mode radiator

In array design, a critical consideration is the suppression of grating lobes, which occur when the unit cell period exceeds approximately one wavelength at the operating frequency, assuming plane wave radiation from the elements. However, when slot or horn antennas are used as radiating elements, their aperture field is not an ideal plane wave. Instead, the amplitude variation ΔE across the aperture field determines the sidelobe distribution and aperture efficiency of the array. Therefore, the unit cell period P_x is typically less than one wavelength at the upper frequency.

On the lower frequency side, the bandwidth is determined by the cutoff frequency of the feeding waveguide, which is primarily influenced by the inner cavity dimensions—width a, height b, ridge height R_h, and width R_w, as illustrated in Fig. 2(c). The distance between the feed waveguides is d where $P_x = a + d$. d is chosen to accommodate the feed network and usually set based on fabricating considerations. Therefore, the lower limit of the cutoff frequency is also related to the period P_x. The determination of P_x will be discussed next by analyzing its impact on the amplitude distribution of the aperture field in the H-plane and balancing the bandwidth and aperture efficiency.

6.3.3 Impact of ω/P_x on aperture efficiency and bandwidth

When arranging multiple radiators along the H-plane with a period of P_x, the fields from each element interact, leading to field amplitude fluctuations in the array. The half-power beamwidth ω of each element, which corresponds to the position where the field strength drops to $1/\sqrt{2}$ of its maximum, plays an important role in how these fields coherently combine. This ultimately determines the extent of field fluctuations, which in turn impact the aperture efficiency, η_A. It is defined as as [31]:

$$\eta_A = \frac{(\int |E(x,y)| dxdy)^2}{A\int |E(x,y)|^2 dxdy} \tag{1}$$

where A is the physical aperture area, $E(x,y)$ is the electric field amplitude distribution over the aperture. For an ideal aperture (with uniform electric field distribution), $\eta_A = 1$. Any variations (ripples) in amplitude will reduce efficiency.

Suppose there is an amplitude ripple component ΔE in the aperture over a baseline uniform field E_{uni}. $E(x,y)$ is written as:

$$E(x,y) = E_{uni}\left(1 + \Delta E \cos(kx)\right) \tag{2}$$

where k is the spatial frequency of the ripple, determining its period across the aperture. (1) can be written as:

$$\eta_A = \frac{\left(\int \left|E_{uni}\left(1 + \Delta E \cos(kx)\right)\right| dxdy\right)^2}{A\int \left|E_{uni}\left(1 + \Delta E \cos(kx)\right)\right|^2 dxdy} \tag{3}$$

This can be reduced to:

$$\eta_{\mathrm{A}} = \frac{E_{uni}{}^2 A^2}{A E_{uni}{}^2 A(1+\frac{\Delta E^2}{2})} = \frac{1}{1+\frac{\Delta E^2}{2}} \tag{4}$$

For example, a 3 dB amplitude fluctuation results in an 11.2% decrease in aperture efficiency, while a 1 dB fluctuation only reduces efficiency by 2.1%. Therefore, minimizing the amplitude fluctuation is crucial for aperture efficiency. To further elucidate the relationship between ΔE and ω/P_x, the interference of Gaussian-distributed fields from multiple elements can be modeled. The amplitude distribution $E(x)$ of each element can be approximated by a Gaussian function [32]:

$$E(x) = E_0 \exp(-\frac{(x-x_n)^2}{2\sigma^2}) \tag{5}$$

where E_0 is the peak field amplitude. x_n is the center position of the n-th element. σ is the standard deviation that defines the width of the Gaussian distribution.

When N elements are arranged with the period P_x, the amplitude variation ΔE between the peak field at the center of an element and the trough field at the midpoint between two adjacent elements can be generalized by considering the superposition from all N elements. That is $E_{trough}(0)$ at the midpoint between two adjacent elements can be expressed as:

$$E_{trough}(0) = \sum_{n=-\frac{N-1}{2}}^{\frac{N-1}{2}} E_0 \exp\left(-\frac{(P_x/2-nP_x)^2}{2\sigma^2}\right) \tag{6}$$

At the center of an element (e.g., at $x=-P_x/2$), the total field $E_{peak}(-P_x/2)$ can be approximated as:

$$E_{peak}(-P_x/2) = \sum_{n=-\frac{N-1}{2}}^{\frac{N-1}{2}} E_0 \exp\left(-\frac{(nP_x)^2}{2\sigma^2}\right) \tag{7}$$

The amplitude variation ΔE is therefore:

$$\Delta E = E_{peak} - E_{trough} \tag{8}$$

Substituting the expressions for E_{peak} and E_{trough} and given that:

$$\Delta E = E_0 \sum_{n=-\frac{N-1}{2}}^{\frac{N-1}{2}} \exp\left(-\frac{(nP_x)^2}{2\sigma^2}\right) - E_0 \sum_{n=-\frac{N-1}{2}}^{\frac{N-1}{2}} \exp\left(-\frac{(P_x/2-nP_x)^2}{2\sigma^2}\right) \tag{9}$$

σ is related to the half-power beamwidth ω by:

$$\sigma = \frac{\omega}{2\sqrt{2\ln 2}} \tag{10}$$

(8) can be expressed as:

$$\Delta E = E_0 \sum_{n=-\frac{N-1}{2}}^{\frac{N-1}{2}} \exp\left(-\frac{\ln 2 \cdot (nP_x)^2}{\omega^2}\right) - E_0 \sum_{n=-\frac{N-1}{2}}^{\frac{N-1}{2}} \exp\left(-\frac{\ln 2 \cdot (P_x/2 - nP_x)^2}{\omega^2}\right) \tag{11}$$

This shows that the amplitude variation ΔE depends on the period P_x and the half-power beamwidth ω. As illustrated in Fig. 6.3(a), when the period P_x is fixed, ΔE decreases with increasing beamwidth ω. Conversely, as shown in Fig. 6.3(b), when ω is fixed, ΔE grows with increasing P_x.

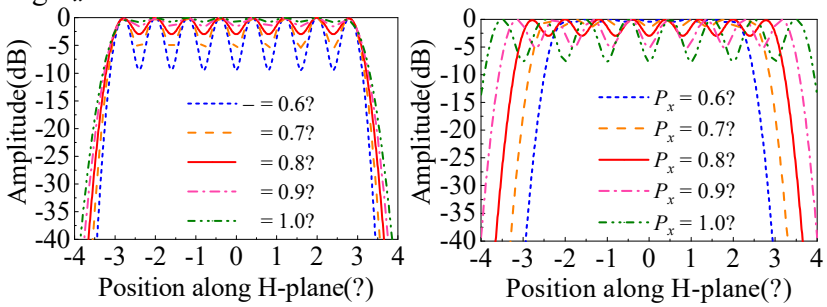


Fig. 6.3 Calculated near-field amplitude distribution of 8-elements array. (a) Different half-power widths (H-plane, $P_x = 0.8\lambda$); (b) Different periods (H-plane, $\omega = 0.8\lambda$)

Equation (11) can be normalized by introducing the variable α ($\alpha = \omega / P_x$):

$$\Delta E = \sum_{n=-\frac{N-1}{2}}^{\frac{N-1}{2}} \left[\exp\left(-\frac{\ln 2 \cdot n^2}{\alpha^2}\right) - \exp\left(-\frac{\ln 2 \cdot (1/2 - n)^2}{\alpha^2}\right)\right] \tag{12}$$

Fig. 6.4(a) shows the variation of ΔE as a function of the ratio ω / P_x for an 8-element array, illustrating how ΔE changes as the beamwidth-to-period ratio varies. Fig. 6.4(b) demonstrates that a larger ω / P_x ratio results in higher aperture efficiency.

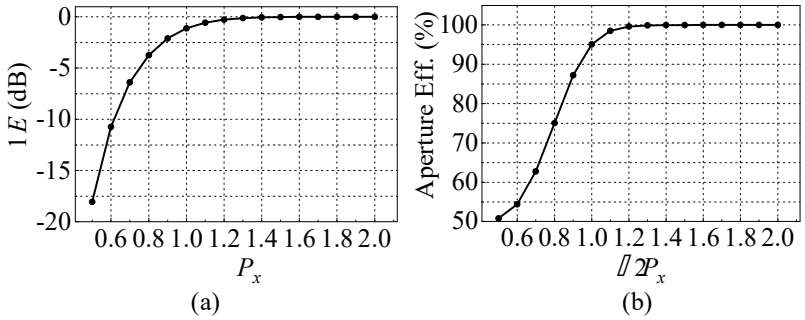


Fig. 6.4 Theoretical analysis of array efficiency. (a) Variation of ΔE; (b) Variation of aperture efficiency, as a function of ω / P_x for an 8-element array.

Compared to rectangular waveguides, double-ridged waveguides exhibit a more concentrated field distribution at the aperture, particularly with higher field strength near the ridges. This leads to a smaller half-power width ω for double-ridged waveguides. It should be noted that in this context, the beamwidth refers to the amplitude distribution in the near field rather than the far-field radiation pattern. By increasing the height of the

quasi-TEM radiator and gradually transitioning to a parallel-plate waveguide, a larger half-power width ω can be achieved.

There is a necessary trade-off between the period P_x and the half-power beamwidth ω in terms of bandwidth, aperture efficiency, and profile height. Increasing the radiation height helps to increase the half-power beamwidth ω, which allows for a larger period P_x. This enables the use of larger double-ridged waveguides, which in turn lowers the cutoff frequency and results in a wider bandwidth. Conversely, achieving a lower profile requires a smaller period P_x, but this comes at the cost of a narrower bandwidth due to a higher cutoff frequency

6.4 Wideband Antenna Element – Design Procedure

6.4.1 Determining the dimensions of double-ridged waveguide

The low-profile requirement necessitates minimizing period P_x, which in turn requires the smallest possible dimensions for the double-ridged waveguide. Since the lower band edge is at 10 GHz, the dimensions of the double-ridged waveguide were determined to have a cutoff at 10 GHz. That is a=6 mm, b=5.3 mm, R_h =2.3 mm, and R_w =1.5 mm. b was chosen to be the half-wavelength at the peak frequency to suppress the propagation of higher-order TE_{01} modes. Considering the manufacturability, the air gap R_{gap} between the ridges was set to be 0.7 mm, leading to an R_h of 2.3 mm. Full-wave simulation confirmed the cutoff frequency of 10 GHz.

6.4.2 Determining the period P_x

Given the requirement for a path for the feed transmission line between the elements, d was set to 2 mm, considering the manufacturing process. The air cavity width of the feed channel is 1 mm, with wall thicknesses of 0.5 mm on each side. Consequently, Px can be determined as $Px = a + d$ resulting in 8 mm.

6.4.3 Transition from double-ridged waveguide to free space

From Fig. 6.4(b), $\alpha = \omega/P_x > 1$ is required to achieve an aperture efficiency greater than 98%. After determining the dimensions of the double-ridged waveguide and P_x, a smooth transition to the free-space wave impedance (377Ω) was first implemented to achieve the wideband and a broader half-power beamwidth ω. The ridge profile was optimized using full-wave simulation, employing a cubic Bézier curve [33], as shown in Fig. 6.5(a). To simplify fabrication, this continuous curve was discretized into multiple steps, as illustrated in Fig. 6.5(b)

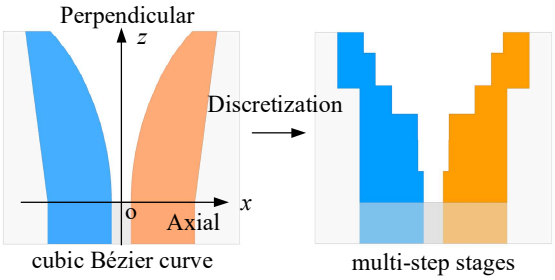


Fig. 6.5 Profile of the ridges. (a) A gradual transition employing a cubic Bézier curve; (b). Discretized into multistep.

6.4.4 Eight-element linear array

In Fig. 6.6, eight radiators are arranged in a linear array along the H-plane. At 31 GHz, the aperture achieves a consistent amplitude distribution with fluctuations of about 1 dB, resulting in an aperture efficiency exceeding 98%.

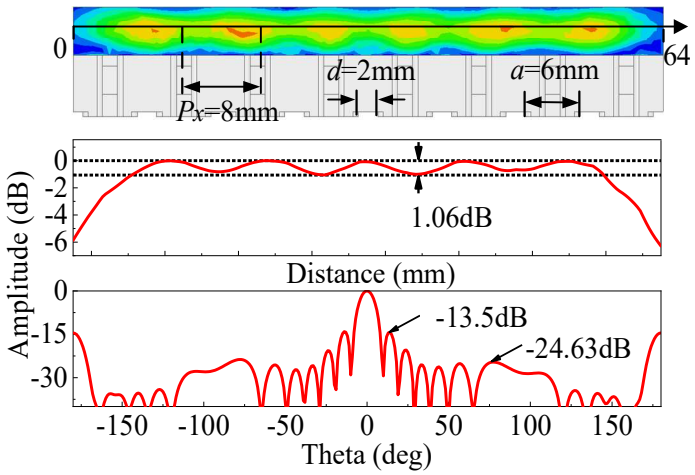


Fig. 6.6 Simulated E-field distribution along the aperture in the H-plane and the corresponding radiation pattern at 31 GHz.

6.5 Array and Feeding Network

A 2×2 sub-array is used as the optimization unit instead of a single element. This is because the element spacing is sufficiently small so that the discontinuities introduced by adjacent elements cannot be neglected. To prevent the occurrence of grating lobes, the periodicity along the y-axis (P_y) is set to 8.5 mm. In the design, periodic boundary conditions (PBC) were incorporated to model the electromagnetic coupling between adjacent elements, as illustrated in Fig. 6.7(a). Each quasi-TEM mode radiator (in Fig. 6.7(b)) is driven by a coaxial-to-ridge waveguide transition (in Fig. 6.7(d)). Four of these transitions are driven by a 1-to-4 rectangular coaxial feed network (in Fig. 6.7(c)) with equal amplitude and phase.

6.5.1 Feeding configuration

Feeding networks also affect the achievable bandwidth. Fig. 6.8(a) illustrates a conventional E-plane feed configuration. All elements are excited from the same side with equal amplitude and phase excitation. However, this configuration requires two feed channels between adjacent elements. This would mean a large period, which narrows the bandwidth and reduces aperture efficiency at higher frequencies.

Fig. 6.8(b) shows an E-plane opposite-side excitation topology. Adjacent elements are fed with opposite phases using a differential feeding structure at the final stage of the network. This eliminates the need for two feed channels between adjacent elements. However, the differential power divider in the final stage is often implemented using an E-plane T-junction, which again limits the bandwidth due to the cutoff frequency.

An H-plane same-side excitation topology was proposed for this design, as illustrated in Fig. 6.8(c). The feeding network is based on rectangular coaxial lines. A transition structure is needed at the feed point of the ridge waveguide.

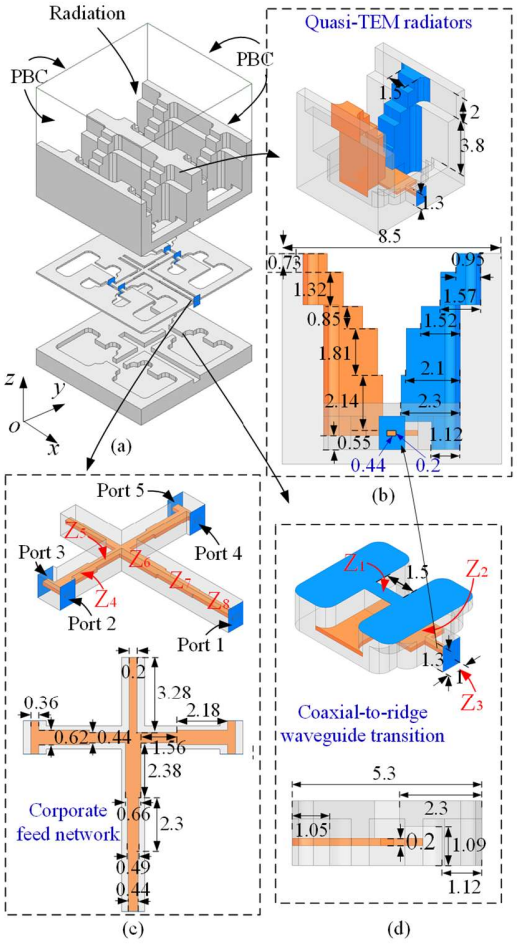


Fig. 6.7. 2×2 subarray: (a) Array structure; (b) Quasi-TEM radiators; (c) 1-to-4 coaxial feed network; (d) rectangular coaxial to ridge waveguide transition. All dimensions are given in millimeters.

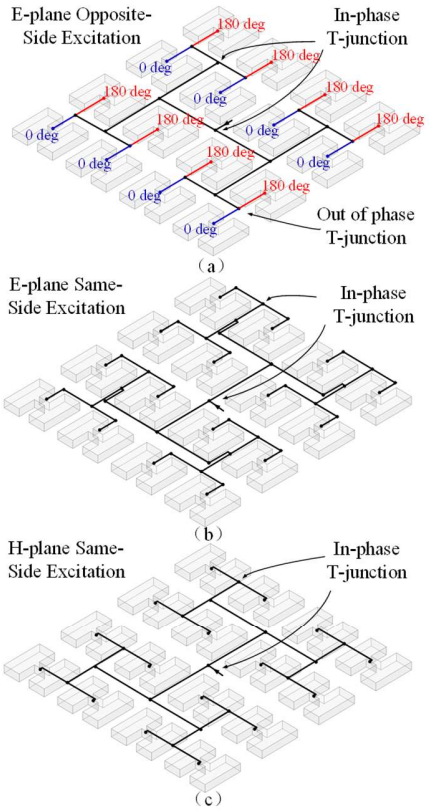


Fig. 6.8. Different feeding configurations. (a) E-plane opposite-side feed; (b) E-plane same-side feed; (c) Proposed H-plane same-side feed.

6.5.2 Rectangular-coaxial-to-ridge-waveguide transition

The transition is shown in Fig. 6.7(d). It has an 'L'-shaped probe, with one end connected to a ridge. The dimensions of the rectangular coaxial line (Z3 marked out in Fig. 6.7(d)) were considered with an emphasis on minimizing transmission loss. The size of the outer conductor was constrained by the available space and the bandwidth of the dominant mode. Considering manufacturing constraints, the inner conductor was specified to be a width of 0.44 mm, and a height of 0.2 mm. Fig. 6.9(a) illustrates the effect of the outer conductor height on the transmission coefficient. With an outer conductor width of 1 mm, increasing its height reduces insertion loss. However, beyond 1.3 mm, the reduction becomes negligible. Therefore, the height was set to 1.3 mm. Fig. 6.9(b) shows the variation in the cutoff frequency of the first higher-order TE11 mode as the inner conductor width increases from 0.4 mm to 0.64 mm, while maintaining an outer conductor size of 1 mm × 1.3 mm and an inner conductor thickness of 0.2 mm. The results indicate that all coaxial configurations used in this work operate within the dominant mode bandwidth and remain well below the first higher-order mode cutoff frequency.

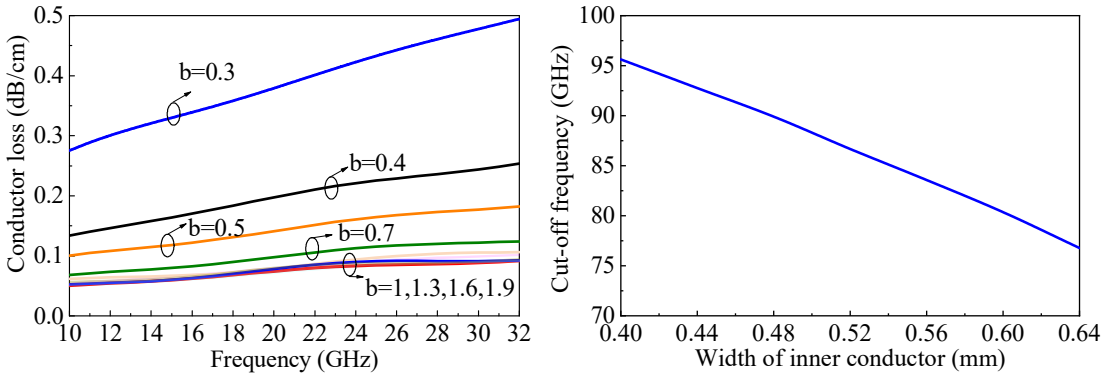


Fig. 6.9 Conductor loss and dominant mode bandwidth of the rectangular coaxial line: (a) conductor loss as a function of outer conductor height and (b) cut-off frequency of TE_{11} mode as a function of inner conductor width.

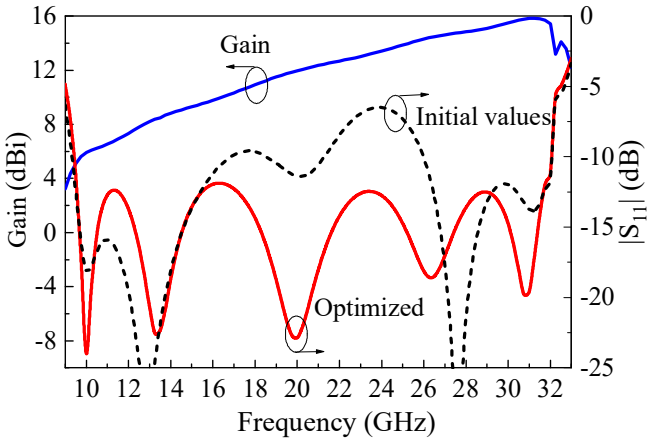


Fig. 6.10 Simulated $|S_{11}|$ of the 2×2-subarray with initial and optimized values and the gain.

6.5.3 1-to-4 feeding network of the 2×2 sub-array

Fig. 6.7(a) shows the 2×2 sub-array and Fig. 6.7(c) is the 1-to-4 feeding network. Each transmission line segment was around a quarter of the wavelength at 31 GHz, which is about 2.4 mm. The initial impedance value of each stage is calculated as the geometric mean of the impedances of the adjacent stages. The impedance Z_1 of the double-ridged waveguide is 100 Ω. Z_3, Z_5 and Z_8 in Fig. 6.7(d), with a line width of 0.44 mm as discussed in the last section, are 70 Ω. Z_2 was calculated to be 83.66 Ω and Z_4 to be 35 Ω with Z4 specifically accounting for the parallel impedance relationship in the T-junction. For Z_5 to Z_8, a fourth-order Chebyshev impedance transformer was employed, where $Z_5/2$ gradually transformed through two stepped stages to Z_8. The calculated values were Z_6 =43.3 Ω and Z_7 =53.5 Ω. These initial values were optimized for the 2×2 subarray. As shown in Fig. 6.10, the subarray achieves an $|S_{11}|$ below -13 dB across the 10-32 GHz band. The close agreement between the simulated results based on the initial and the optimized impedance values indicate the effectiveness of the design method. The optimized dimensions are detailed in Fig. 6.7.

The gain steadily increases from 6 dBi to 15.9 dBi. The radiation pattern shown in Fig. 6.11 is nearly symmetrical about the center with no significant sidelobes, which confirms the wideband radiation capability.

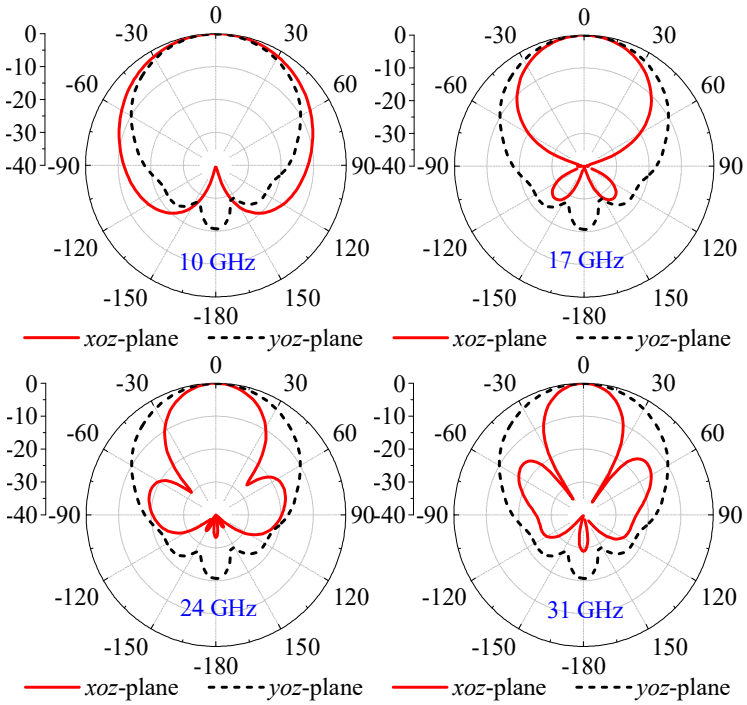


Fig. 6.11 Simulated radiation patterns of the 2×2-element array at 10GHz, 17GHZ, 24GHz and 31GHz.

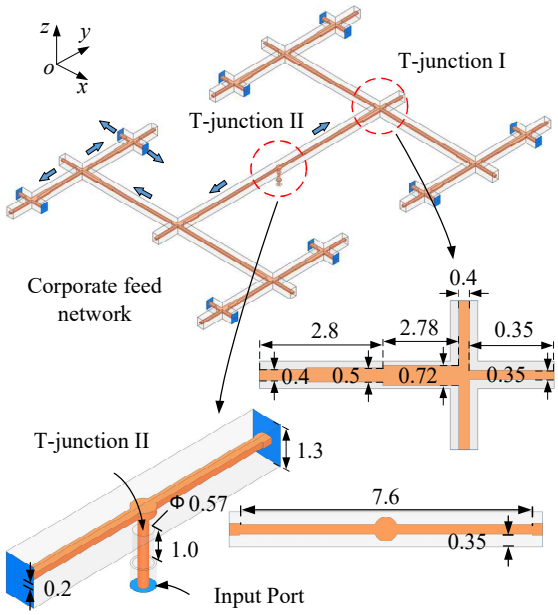


Fig. 6.12 A-to-16 corporate feed network using two types of T-junctions.

6.5.4 1-to-16 corporate feeding network for complete array

A broadband 1-to-16 equal-amplitude, in-phase power divider network was used to form the whole array, as shown in Fig. 6.12. There are several coaxial-line T-junctions. T-junction-I consists of a short-circuited impedance stub and a multi-stage λ/4 impedance transformer. It is equivalent to a fourth-order Chebyshev impedance transformer.

Unlike T-junction-I, T-junction-II is fed from the bottom using a standard 50 Ω coaxial probe for testing purposes. Typically, the probe diameter of a commercial coaxial connector remains fixed, so impedance transformation at the input can only be achieved by adjusting the outer diameter of the coaxial structure. To simplify assembly, a 0.7 mm diameter disc was added to the joint. As shown in Fig. 6.13, both T-junctions achieve an $|S_{11}|$ of less than -19 dB across the 10-32 GHz range. The combined 1-to-16 feed network also achieved excellent matching from 10 to 32 GHz, as shown in Fig. 6.14, with the reflection coefficient below -20 dB.

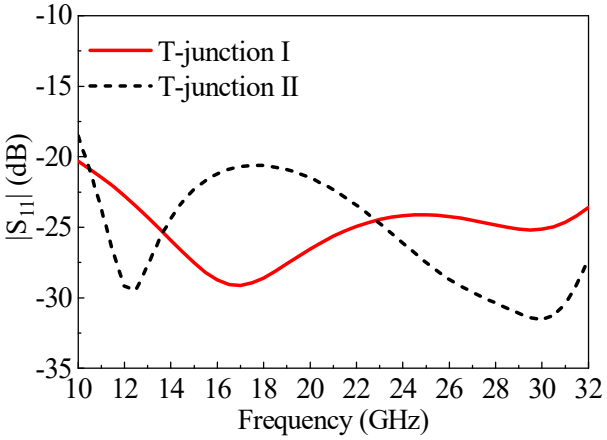


Fig. 6.13 Simulated $|S_{11}|$ of the proposed T-junction I and T-junction II.

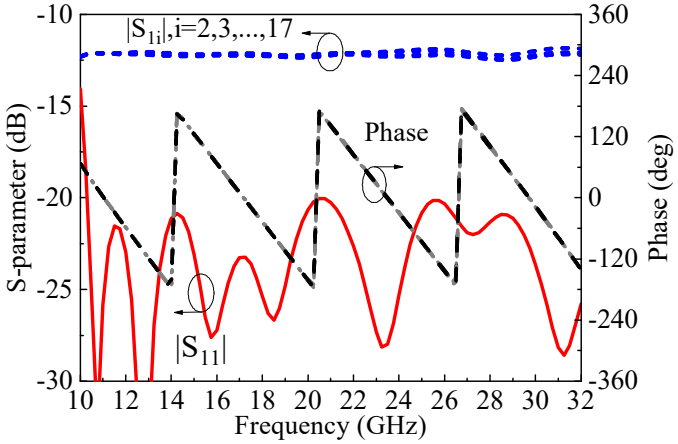


Fig. 6.14 Simulation results of the S-parameters for the one-to-sixteen corporate feed network.

6.6 Experimental Results

The prototype is assembled from three layers, as shown in Fig. 6.15. Layers M1 and M2 are fabricated using CNC machining from 6061 aluminum. The nominal electrical conductivity is 3.8×10^7 S/m, and the surface roughness is 0.8 μm. Layer M3 is manufactured using high-precision laser cutting from stainless steel and is subsequently copper-plated. The dimensions of the antenna are 68 mm × 64 mm × 9 mm (with an aperture of 66.4 mm × 64 mm). The S-parameters are measured using a network analyzer (Agilent E8361C), and the radiation patterns and gains are evaluated with a compact-range antenna testing system.

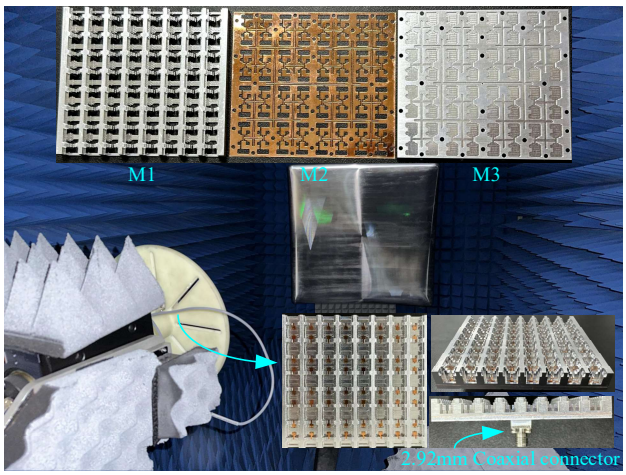


Fig. 6.15 Photographs of the fabricated prototype and testing environment.

6.6.1 S Parameters

Fig. 6.16 shows the simulated and measured reflection coefficients. In the desired frequency range of 10-32 GHz, the measured reflection coefficients are less than -10 dB. The simulation and measurement results show a good agreement.

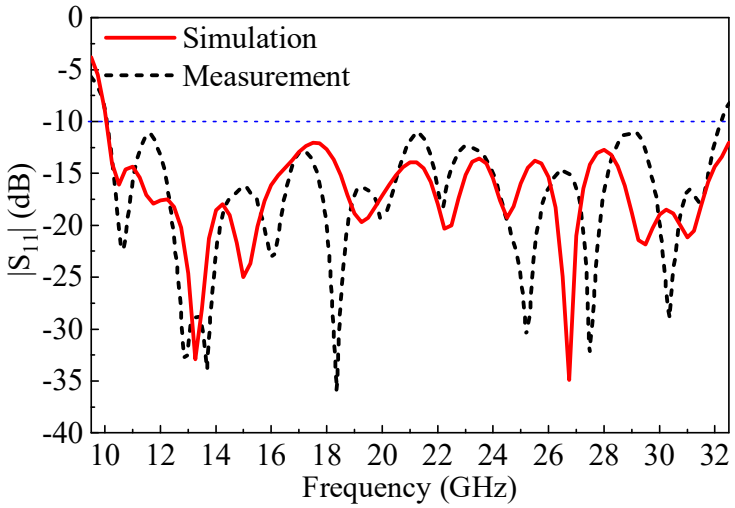


Fig. 6.16 Simulated and measured reflection coefficients.

6.6.2 Radiation Performance

Table I presents the normalized radiation patterns at 10, 21, and 32 GHz, comparing simulation with measurement. They are consistent across the frequency band and show good alignment with the simulated patterns. The side lobe levels are around -13.1 dB, which is expected for a square array driven by constant amplitude and phase excitation. Fig. 6.17 displays the simulated and measured peak gain and aperture efficiency as a function of frequency. The discrepancy between the measured and simulated peak gains is less than 0.4 dB, which is primarily attributed to fabrication tolerances and assembly variations. The measured aperture efficiency exceeding 90% over 10.5–31 GHz. Across the entire band of 10–32 GHz, the efficiency remains above 82%.

The measured aperture efficiency η_{mea_ap} is calculated by using the following equation:

$$\eta_{mea_ap} = \frac{G_{mea}}{D_{ideal}} \cdot \frac{D_{ideal}\lambda^2}{4\pi A} \tag{13}$$

where, G_{mea} is the measured peak gain, D_{ideal} is the calculated theoretical maximum directivity, λ is the free-space wavelength, and A is the aperture area of the antenna.

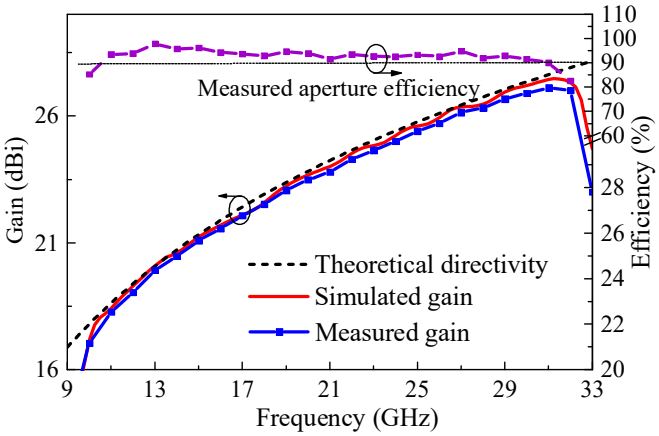
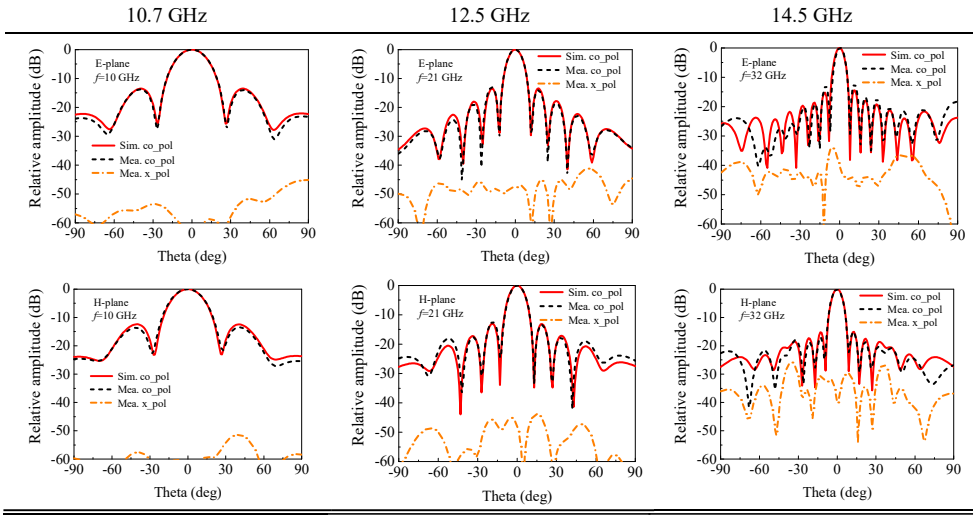


Fig. 6.17 Simulated and Measured peak gain and calculated aperture efficiency.

TABLE I
NORMALIZED RADIATION PATTERNS OF THE ULTRA-WIDEBAND ARRAY ANTENNA



6.6.3 Comparison

The performance of this work is compared with several published linearly polarized wideband waveguide antenna arrays, as summarized in Table II. The extension of the lower frequency range in [15] was constrained by the slot's cutoff frequency. It also has grating lobes at higher frequencies. [17] utilized ridge gap waveguides (RGW) and E-plane groove gap waveguides (E-GGW). Their large unit cell resulted in grating lobes at higher frequencies. [18] employed a one-to-one excitation. Still it suffered from grating lobes. These designs showed the upper limit of bandwidth performance for air-filled slot-based array antennas.

[21] and [26] utilized parallel-plate waveguides (PPW) radiators, achieving wider bandwidth without grating lobes. However, it has high profile due to the use of multi-layer PPW power dividers. Our work presents the widest reported bandwidth (105%) and the

TABLE II
PERFORMANCE COMPARISON OF LINEAR POLARIZED WIDEBAND WAVEGUIDE ANTENNA ARRAY

Ref.	Element Type	Fabrication technology	No. layers	Scale	Freq. Band (GHz)	FBW (%)	Thickness (λ_{min}[a])	Aperture efficiency	Gain (dBi)	Grating Lobes
[15]	Slot	CNC milling	3	8×8	10.24-14.87	36.9	1.17	60%~82%	23.4~26.3	Yes
[17]	Ridge WG	CNC milling	3	8×8	18.8-30.3	46.8	1.23	40%~89%	14.3~27.7	Yes
[18]	Slot	3D printing	1	16×16	24.2-41.2	52	1.6	N.a	N.a	Yes
[21]	CTS	CNC milling+ PCB	10	16×1	26.5-40	42	3.5	~40%	28.87	No
[26]	CTS	CNC milling	18	64×1	17-31	58	4.3	43%~61%	30.8~32.7	No
This work	Quazi-TEM radiator	CNC milling	3	8×8	10-32	105	0.3	82%~95%	17.2~27.3	No

[a]λ_{min} is the wavelength at the lowest frequency

lowest profile height (0.3λ) among full-metal air-filled waveguide arrays to date. The aperture efficiency is also among the highest. in the widest reported bandwidth (105%) and the lowest profile height (0.3λmin) among full-metal air-filled planar waveguide antennas to date.

6.7 Applications for SATCOM and mmWave backhaul

Modern SATCOM terminal antennas need to support wide bandwidths and multiple polarizations to meet the demands of high-throughput satellite systems.

In K/Ka band SATCOM, transmit and receive bands typically utilize two orthogonal circular polarizations, which are essential for mitigating multipath effects and eliminating polarization distortion. One effective method to achieve multi-band, multi-polarization functionality on a single aperture is to integrate a wideband linearly polarized array with dual-band orthogonal linear-to-circular polarization converters (LCPCs) [22]. This approach is particularly well-suited for lightweight, high-gain applications, such as communication on-the-move (COTM) systems on vehicles or aircraft, as well as for portable stations

6.8 Conclusion

This paper presents an ultra-wideband planar waveguide array that achieves an 105% fractional bandwidth across the 10 to 32 GHz frequency range, with an aperture efficiency reaching up to 95%. The design features a corporate feed network that directly excites quasi-TEM radiators in a one-to-one configuration, significantly enhancing both bandwidth and efficiency while maintaining a compact, low-profile form factor. This design approach overcomes key constraints of the bandwidth from the cut-off of the radiators as well as from the feeding networks. The demonstrated high performance of the wideband antenna array could have applications in point-to-point communications and SatCom systems, where wide bandwidth and high gain are highly desired. This design also offers a promising and scalable solution for antenna systems requiring low-profile, high-gain, and wideband.

Reference

[1] Z. Siddiqui et al., "Dual-Band Dual-Polarized Planar Antenna for 5G Millimeter-Wave Antenna-in-Package Applications," in *IEEE Trans. Antennas Propag*, vol. 71, no. 4, pp. 2908-2921, April 2023.

[2] Ericsson, October 2016, Ericsson Microwave Outlook report 2016, https://www.ericsson.com/assets/local/microwave-outlook/documents/ ericsson-microwave-outlook-report-2016.pdf

[3] J. Xu, W. Hong, Z. H. Jiang, H. Zhang, and K. Wu, "Low profile wideband vertically folded slotted circular patch array for Ka-band applications," *IEEE Trans. Antennas Propag.*, vol. 68, no. 9, pp. 6844 – 6849, Sep. 2020.

[4] C. Granet, J. S. Kot and J. Ness, "Wideband Ka-band SATCOM-on-the-move antenna concept: preliminary design study," 13*th European Conference on Antennas and Propagation (EuCAP)*, Krakow, Poland, 2019, pp. 1-5.

[5] G. Sun and H. Wong, "A planar millimeter-wave antenna array with a pillbox-distributed network," *IEEE Trans. Antennas Propag.*, vol. 68, no. 5, pp. 3664-3672, May 2020.

[6] Z. Hao, Q. Yuan, B. Li and G. Q. Luo, "Wideband W-band substrate-integrated waveguide magnetoelectric (ME) dipole array antenna," *IEEE Trans. Antennas Propag.*, vol. 66, no. 6, pp. 3195-3200, Jun. 2018.

[7] M. Yang, Y. Pan, Y. Sun and K. Leung, "Wideband circularly polarized substrate-integrated embedded dielectric resonator antenna for millimeter-wave applications," *IEEE Trans. Antennas Propag.*, vol. 68, no. 2, pp. 1145-1150, Feb. 2020.

[8] X. Wang, Y. Cheng and Y. Dong, "A wideband PCB-stacked air-filled luneburg lens antenna for 5G millimeter-wave applications," *IEEE Antennas Wireless Propag. Lett.*, vol. 20, no. 3, pp. 327-331, Mar. 2021.

[9] X. Dai and K. M. Luk, "A wideband dual-polarized antenna for millimeter-wave applications," *IEEE Trans. Antennas Propag.*, vol. 69, no. 4, pp. 2380-2385, Apr. 2021.

[10] J. Wang et al., "A low-profile vertically polarized magneto-electric monopole antenna with a 60% bandwidth for millimeter-wave applications," *IEEE Trans. Antennas Propag.*, vol. 69, no. 1, pp. 3-13, Jan. 2021.

[11] Y. Miura, J. Hirokawa, M. Ando, Y. Shibuya and G. Yoshida, "Double-layer full-corporate-feed hollow-waveguide slot array antenna in the 60-GHz band," *IEEE Trans. Antennas Propag.*, vol. 59, no. 8, pp. 2844-2851, Aug. 2011.

[12] T. Tomura, J. Hirokawa, T. Hirano, and M. Ando, "A 45° linearly polarized hollow-waveguide 16×16-slot array antenna covering 71 – 86 GHz band," *IEEE Trans. Antennas Propag.*, vol. 62, no. 10, pp. 5061 – 5067, Oct. 2014.

[13] S. Zhou, P. Dong, G. Huang, C. Sim and J. Li, "Wideband antenna array with full metal structure and air-filled microstrip feeding network," *IEEE Trans. Antennas Propag.*, vol. 65, no. 6, pp. 3041-3048, June 2017.

[14] A. Farahbakhsh, D. Zarifi and A. U. Zaman, "A mmWave wideband slot array antenna based on ridge gap waveguide with 30% bandwidth," *IEEE Trans. Antennas Propag.*, vol. 66, no. 2, pp. 1008-1013, Feb. 2018.

[15] Z. Shi-Gang, H. Guan-Long, P. Zhao-hang and L. Ying, "A wideband full-corporate-feed waveguide slot planar array," *IEEE Trans. Antennas Propag.*, vol. 64, no. 5, pp. 1974-1978, May 2016.

[16] F. Sun, Y. Li, X. Wang, J. Wang, L. Ge and B. Ai, “A Millimeter-Wave 48% Bandwidth High-Gain 3-D-Printed Antenna Array Using T-Junctions With Multiple Reflection Nulls,” *IEEE Trans. Antennas Propag.*, vol. 71, no. 9, pp. 7273-7284, Sept. 2023.
[17] T. Zhang, R. Tang, L. Chen, S. Yang, X. Liu and J. Yang, “Ultra-Wideband Full-Metal Planar Array Antenna with a Combination of Ridge Gap Waveguide and E-Plane Groove Gap Waveguide,” *IEEE Trans. Antennas Propag.*, vol. 70, no. 9, pp. 8051-8058, Sept. 2022.
[18] X. Wang, Y. Li, F. Sun, J. Wang, L. Ge and B. Ai, “A Millimeter-Wave 51% Bandwidth High-Gain 3-D-Printed Antenna Array Based on Optimized Multistage Phase Cancellation in Feed Network,” *IEEE Trans. Antennas Propag.*, vol. 71, no. 12, pp. 10003-10008, Dec. 2023.
[19] P. Liu, G. F. Pedersen and S. Zhang, “Wideband slot array antenna fed by open-ended rectangular waveguide at W-band,” *IEEE Antennas Wireless Propag. Lett.*, vol. 21, no. 4, pp. 666-670, Apr. 2022.
[20] W. W. Milroy, “Compact, ultrawide-band antenna feed architecture comprising a multistage, multilevel network of constant reflection coefficient components,” U.S. Patent 6 075 494, 2000.
[21] M. Ettorre, F. F. Manzillo, M. Casaletti, R. Sauleau, L. Le Coq and N. Capet, “Continuous Transverse Stub Array for Ka-Band Applications,” *IEEE Trans. Antennas Propag.*, vol. 63, no. 11, pp. 4792-4800, Nov. 2015.
[22] M. Del Mastro et al., “Ultra-Low-Profile Continuous Transverse Stub Array for SATCOM Applications,” *IEEE Trans. Antennas Propag.*, vol. 70, no. 6, pp. 4459-4471, June 2022.
[23] T. Potelon et al., “A low-profile broadband 32-slot continuous transverse stub array for backhaul applications in E-Band,” *IEEE Trans. Antennas Propag.*, vol. 65, no. 12, pp. 6307-6316, Dec. 2017.
[24] Q. You, Y. Lu, Y. You, Y. Wang, Z. Hao and J. Huang, “Wideband full-corporate-feed waveguide continuous transverse stub antenna array,” *IEEE Access*, vol. 6, pp. 76673-76681, 2018.
[25] M. Huang, Y. Lu, Q. You, J. Xu and J. Huang, “High-efficiency full-metal planar slot array antenna with over 60% bandwidth”, *IEEE Antennas Wireless Propag. Lett.*, vol. 22, pp. 1124-1128, 2023.
[26] A. Mahmoud, M. Ettorre and R. Sauleau, “High-Gain Tapered Long Slot Array for SATCOM Applications in PCB Technology with Folded Corporate Feed Network,” *IEEE Trans. Antennas Propag.*, vol. 72, no. 1, pp. 343-355, Jan. 2024.
[27] Q. You, Y. Lu, Y. Wang, J. Xu, J. Huang and W. Hong, “Hollow-Waveguide Tri-Band Shared-Aperture Full-Corporate-Feed Continuous Transverse Stub Antenna,” *IEEE Trans. Antennas Propag.*, vol. 70, no. 8, pp. 6635-6645, Aug. 2022.
[28] M. Sano, J. Hirokawa and M. Ando, “A Hollow Rectangular Coaxial Line for Slot Array Applications Fabricated by Diffusion Bonding of Laminated Thin Metal Plates,” *IEEE Trans. Antennas Propag.*, vol. 61, no. 4, pp. 1810-1815, April 2013.
[29] M. Sano, J. Hirokawa and M. Ando, "Single-layer corporate-feed slot array in the 60-GHz band using hollow rectangular coaxial lines", IEEE Trans. Antennas Propag., vol. 62, no. 10, pp. 5068-5076, Oct. 2014.

[30] Y. Lu, S. Shen, Y. You, J. Xu and J. Huang, "Wideband Dual Linearly Polarized Hollow- Waveguide Septum Antenna Array for Ku-Band Satellite Communications," *IEEE Trans. Antennas Propag.*, vol. 71, no. 3, pp. 2433-2442, March 2023.
[31] C. A. Balanis, Antenna Theory: Analysis and Design, 3rd ed. Hoboken, NJ: John Wiley & Sons, 2005.
[32] Mailloux, R. J. Phased Array Antenna Handbook, 2nd Edition, Artech House, 2005.
[33] M. Gerber, J. W. Odendaal and J. Joubert, "Ridge Profile Optimization of DRGH Antenna," *2018 IEEE Radio and Antenna Days of the Indian Ocean (RADIO)*, Wolmar, Mauritius, 2018, pp. 1-3.

CHAPTER 7: SUB-TERAHERTZ MONOLITHIC METAL 3D-PRINTED CORRUGATED HORN ANTENNA WITH HIGH CROSS-POLAR DISCRIMINATION

Qingchun You, Talal Skaik, Peter Young, Nathan Miller, Peter Hunyor, Peter Huggard, Yi Wang

Yi Wang proposed, organized, and oversaw the entire study, taking the lead on the project. Qingchun You originated the design, conducted the theoretical modeling, analysis, simulations, carried out the experiments, interpreted the results, and drafted the manuscript. Peter Young and Nathan Miller offered advice and guidance throughout the project, Peter Hunyor and Peter Huggard provided the gold plating, while Talal Skaik supported the fabrication and measurement. All authors contributed to the writing of the paper and reviewed the final manuscript.

This chapter is based on the following publication: 5. Q. You, T. Skaik, P. Young, N. Miller, P. Hunyor, P. Huggard and Y. Wang., "Subterahertz Monolithic Metal 3D-Printed Corrugated Horn Antenna with High Cross-Polar Discrimination," *IEEE Trans. Terahertz Sci. Technol*, vol. 15, no. 1, pp. 128-132, Jan. 2025, doi: 10.1109/TTHZ.2024.3501585..

Abstract

This letter presents a high-performance corrugated horn for the sub-terahertz, manufactured monolithically using high-precision 3D printing technology based on Micro Laser Sintering (MLS) of stainless-steel powder. The horn features 45° inclined corrugation stubs that allow the building of the component with its vertical axis without any internal support structures. This ensures circular symmetry of the horn and high cross-polarization discrimination, and circumvents radiation performance degradation, typical of tilted printing. Departing from traditional designs, the horn also incorporates a rectangular-to-circular waveguide adapter, not only enhancing compactness but also avoiding errors and losses associated with assembly. The stainless-steel antenna was plated with gold. The prototype, measuring 10.8 mm × 10.8 mm × 29.7 mm, exhibits outstanding performance with a peak gain from 18 to 22 dBi, and >36 dB cross-polar discrimination over the frequency band of 145-225 GHz. This is the first demonstration of 3D-printed corrugation structures in corrugated horns showing high performance beyond 100 GHz.

Keywords: Corrugated horn antenna, 3D Printing, cross-polarization discrimination.

7.1 Introduction

The beam radiated by a corrugated horn antenna possesses desirable characteristics such as circular symmetry in its radiation pattern, low sidelobes, and minimal cross-polarization. Serving as a highly efficient mode coupler between the Gaussian mode in free space and the transmission mode within the metal waveguide, it is widely used in satellite communications, radio astronomy, and measurement instruments. The corrugated horn antenna is often utilized as a primary feed source for reflector antennas to enhance their efficiency and beam symmetry and to reduce cross-polarization [1]. Typically, two types of corrugations are used: radial corrugations for large bandwidth and high beam symmetry [2], and axial corrugations for compact longitudinal dimensions and ease of manufacturing [3].

Millimeter-wave corrugated horns are usually manufactured through direct mechanical machining [4] or electroforming [5]. When the frequency reaches the sub-terahertz or terahertz range, both processes become significantly more challenging and involve very lengthy manufacturing cycles. Direct machining of the corrugation is limited by a depth-to-width ratio of 3-4 for the corrugation, due to the size constraint of the usable milling and turning tools. The process is extremely time-consuming and costly. The same is true for the electroforming approach, as the production of the mandrel requires high-precision machining of increasingly delicate structures. Both the machining and electroforming processes rely on and are ultimately limited by the subtractive manufacturing approach. The recent advancement of additive manufacturing technology offers a new alternative fabrication route for metal waveguide structures like horn antennas. In particular, the laser powder bed fusion (LPBF) technology [6] allows the 3D printing of all-metal antennas. A 35-50 GHz metal 3D-printed horn antenna with radial corrugations has been reported in [7]. It was printed at an inclined angle to avoid overhang. A separately machined rectangular-to-circular waveguide transition was required for measurements. Results indicate comparable performance with directly machined corrugated horns. Another 30-50 GHz metal 3D printed corrugated horn was reported in [8], employing a small flare angle to achieve a wider operating bandwidth. Again, an inclined printing orientation was adopted. Internal support structures, removed before use, were used to ensure fabrication accuracy. A shortcoming of the angled build orientation is the break of circular symmetry during the layer-by-layer printing. The circularity of the waveguide structure can be affected, potentially degrading the radiation pattern and cross-polarization, especially for operation in sub-terahertz and terahertz bands. Additionally, the symmetry of the corrugated horn becomes crucial when employed in feed systems. Orientating the horn with its axis vertical during printing would circumvent this problem in radial corrugated horns [9].

Most LPBF techniques, typically with a manufacturing tolerance of 20 - 200 μm, cannot deliver the manufacturing precision and surface quality required for sub-millimeter features in corrugated horns above 100 GHz, where the corrugation width is usually under 200 μm. A few conical horn antennas, with no corrugation, near the G-Band were reported in [10] and [11]. In [11], a 300 GHz corrugated horn was printed using a polymer stereolithography based printer. However, the subsequent attempt to metallize the antenna failed. We have not found reports of any 3D-printed metal corrugated horns working above 50 GHz in the literature. This is because metal printers delivering a tolerance below 10 mm and a centimeter-scale printing volume are very rare. The use of Micro Laser Sintering

(MLS) based metal 3D printing was reported on different waveguide filters operating from 60 to 300 GHz [12] – [15]. In these components, MLS achieved 5-10 μm manufacture tolerance, under 2 μm surface roughness, and monolithic print with integrated waveguide flanges.

In this letter, we have applied the MLS technique to the additive manufacture of corrugations for the first time and demonstrated its capability in a wideband, monolithically printed and plated, metal corrugated horn for the sub-terahertz (145 - 225 GHz). This end-to-end manufacturing process delivers a high-performance corrugated horn with excellent structural integrity and low surface roughness, without additional polishing. Unlike previous 3D printed corrugated horns [7]-[9] at much lower frequencies, we have integrated the rectangular-to-circular waveguide transition within the monolithic build, making the structure more compact and removing the extra mass of a pair of waveguide flanges. Critically, we have devised a 45° inclined corrugation to allow for the horn to be printed with its axis vertical, which ensures a balance between structural symmetry, bandwidth, cross-polarization, and high gain.

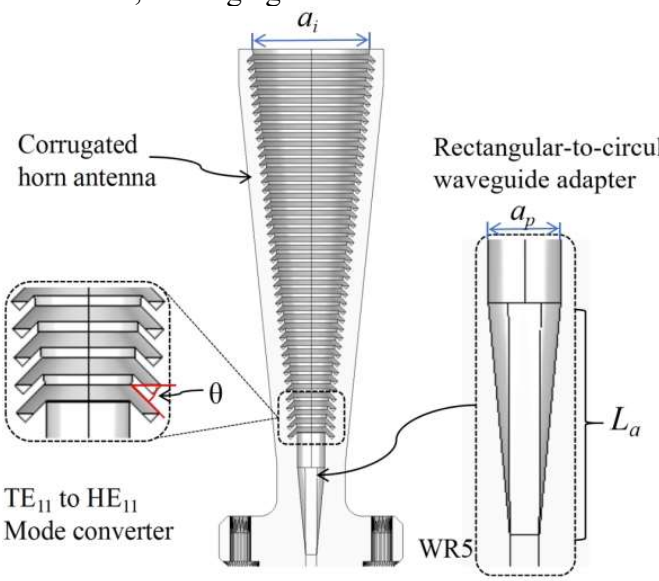
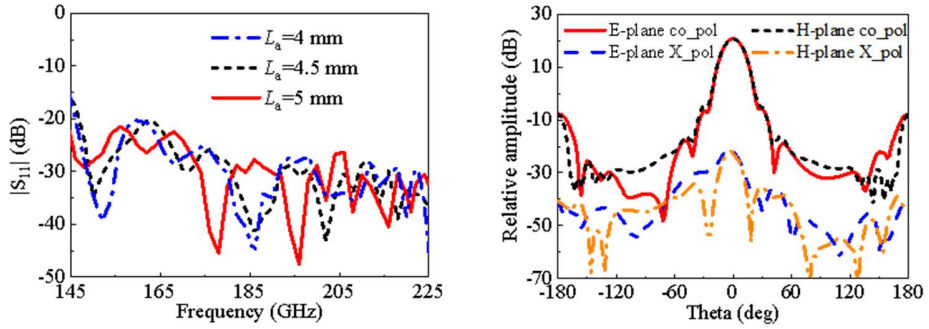


Fig. 7.1 Configuration of the proposed wideband corrugated horn antenna. The dimensions a_i = 6.90mm, a_p =1.60mm etc.

7.2 Configuration and Design

Fig. 7.1 illustrates the configuration of the proposed wideband corrugated horn antenna that can be 3D-printed monolithically and vertically, without requiring any internal support. It consists of three key parts: a rectangular-to-circular waveguide adapter, a TE_{11} to HE_{11} mode converter, and a linear-profiled corrugated horn. This design is optimized for a centre frequency of 180 GHz and can be scaled to a higher band. The aperture size a_i of the corrugated horn is 6.90 mm, and the diameter a_p of the input circular waveguide is 1.60 mm. This is determined by the 3 dB main lobe width and directivity requirements. The input port of the horn antenna utilizes the WR5 standard rectangular waveguide. To accommodate tight spacing requirements for multiple-beam feeders [16], a compact non-standard flange (diameter is 8.3 mm) is employed in this work. The rectangular-to-circular waveguide adapter converts the TE_{10} mode into the TE_{11} mode. It further transforms the

power into the HE_{11} mode through a constant-width slot mode converter. The hybrid HE_{11} mode propagating within the corrugated conical horn section allows circular symmetry, low sidelobes, and high cross-polarization discrimination (XPD). All the modelling and simulation were conducted using HFSS.



(a) (b)

Fig. 7.2 Simulated results. (a) Reflection coefficient of the transition structure with different lengths L_a; (b) Radiation pattern at 180 GHz.

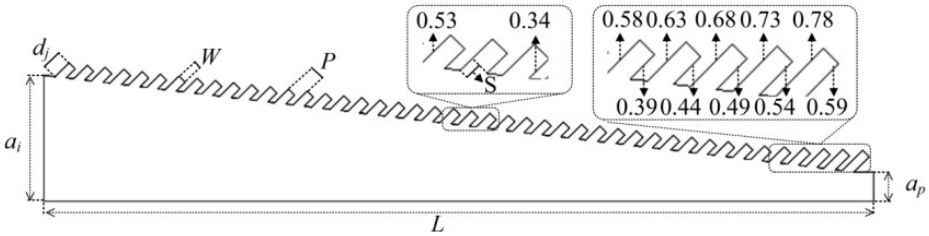


Fig. 7.3 Side view profile and dimensioning of the corrugations. d_j = 0.53mm, W = 0.2mm, P = 0.5mm, S = 0.19mm and L = 24mm.

7.2.1 Rectangular-to-circular waveguide adapter

Benefiting from the free-form modeling capability of 3D printing technology, we achieved a seamless transition from a rectangular to a circular waveguide, thereby ensuring excellent wideband impedance matching. The length, L_a, of the tapered waveguide is a crucial factor influencing impedance matching. A longer L_a would result in a smoother transition and an improved matching bandwidth, especially for the lower frequency, as the parameter study presented in Fig. 7.2(a). However, due to the build height limitation of the 3D printer (< 30 mm), we chose the longest possible length L_a = 5 mm, and the simulated return loss of the adapter remains better than 20 dB across the entire frequency bands of 145-225 GHz.

7.2.2 TE_{11}- HE_{11} mode converter

To excite the HE_{11} mode, a mode converter is required between the circular waveguide and the corrugated horn. This converter is also used for broadband impedance matching. A constant-width slot structure, which is relatively simple in architecture, was chosen. The detailed design process is described in [17]. Fig. 7.2(b) shows the radiation pattern at the central frequency using this mode converter. The main lobes in the H-plane and E-plane are almost identical. The dimensions of the 5-corrugation mode converter are given in Fig. 7.3.

7.2.3 Linear-profile corrugated horn

There is extensive literature on the theory and design of radial corrugated horns [9]. Our key innovation is the use of angled corrugation that avoids overhang in printing and allows the build of the horn antenna vertically without any tilting or support structures. This helps maintain the highly desired circular symmetry of the horn and therefore high XPD. To satisfy beam symmetry and XPD requirements [2], the relative power content of TE_{11} and TM_{11} modes is ideally at 0.85 and 0.15, respectively. The relative phase of TE_{11} and TM_{11} modes at the aperture should be equal. Smaller tooth widths are desirable for optimal coupling from TE_{11} to TM_{11} mode but are constrained by mechanical feasibility. Based on the capabilities of the printer, a minimum tooth width of 0.20 mm and a slot width of 0.30 mm are selected for implementation.

The inclination angle, θ, of the corrugations is defined in Fig. 7.1. Different corrugation inclination angles mean different tooth step lengths, S, as shown in Fig. 7.3. Both S and slot depth, d_j, influence XPD. Fig. 4 shows the variation of reflection coefficient and XPD at θ = 30°, 45°, and 60° with a slot depth of 0.53 mm. It reveals that a 45° corrugation inclination offers
the best XPD. This is also an acceptable angle for avoiding overhanging during printing. From Fig. 7.4(a), it is evident that the smaller θ is (i.e. closer to radial corrugation), the better the impedance matching at low frequencies, resulting in a wider bandwidth. Conversely, the larger θ becomes (closer to axial corrugation), the poorer the impedance matching at low frequencies, leading to a narrower bandwidth. The impact of slot depth on antenna reflection coefficient and XPD is shown in Fig. 7.5. A slot depth of 0.53 mm is ultimately chosen for its higher than 36 dB XPD and competitively low S_{11} below -20 dB across the entire bandwidth.

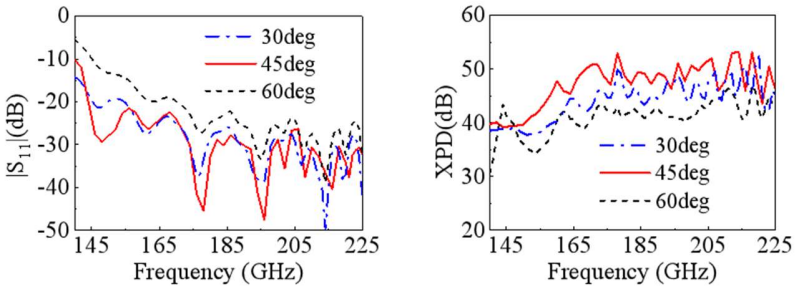


Fig. 7.4 Simulated (a) S_{11} and (b) XPD with different inclination angles, θ of the corrugations.

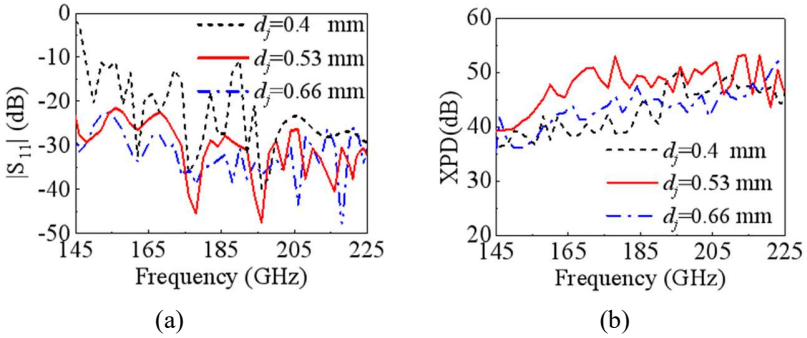


Fig. 7.5 Simulated (a) S_{11} and (b) XPD with different slot depth d_j.

7.3 Fabrication and Experimental Results

The prototype corrugated horn was printed in one piece in stainless steel using Micro Laser Sintering (MLS) technology [12], as shown in Fig. 7.6. It measures 10.8 mm × 10.8 mm × 29.7 mm including the miniature flange, with an aperture size of 9.5 mm × 9.5 mm. The cross-sectional view shown in Fig. 7.6(c) reveals well defined corrugations. The manufacturing tolerance is better than 10 μm.

Due to the low conductivity of stainless steel, a coating of gold is applied to reduce transmission loss. An in-house proprietary electroless plating process was used. The plating process consists of an electroless nickel underlayer to promote the adhesion of the subsequent electroless immersion gold layer followed by an autocatalytic gold layer that is able to produce thicker (~3μm) deposits. The plating process sequence is as follows: (1) rinse, (2) degreasing soak, (3) rinse, (4) acid dip, (5) rinse, (6) Wood's nickel strike, (7) rinse, (8) electroless nickel plating, (9) rinse, (10) immersion and autocatalytic gold plating. The use of electroless plating processes ensure a uniform nickel and gold deposit on the corrugations without the buildup on high current density areas and low deposits on the low current density areas (as seen using an electrolytic plating process) and, due to their levelling properties, improve the surface roughness as well. The finished parts exhibit an average surface roughness (Sa) of 1.8 μm. This roughness results in an effective surface conductivity of 1.03×10^7 S/m [18]. Notably, when contrasted with an ideally smooth gold surface, this level of surface roughness incurs an Ohmic loss of 0.4 to 1 dB across the frequency band according to simulation.

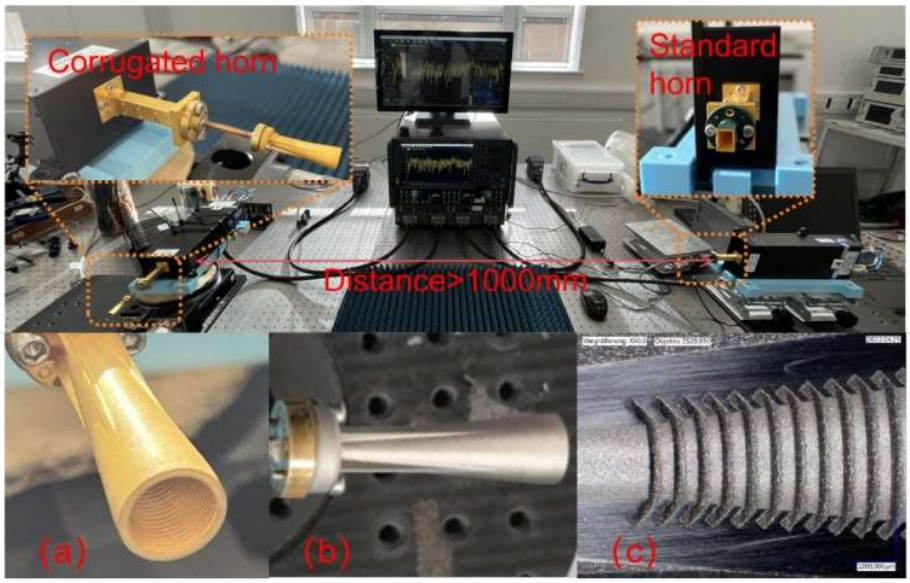


Fig. 7.6 Photographs: (a) Gold plated horn showing the corrugations, (b) As-printed horn before gold coating, (c) Close view of the as-printed corrugations.

As the printed corrugated horn antenna utilizes a non-standard flange, a 40 mm straight waveguide adapter was employed to connect to the testing system. Fig. 7.7 shows that the measured S_{11} of the antenna is better than -13 dB and there is little difference before and after gold coating. The discrepancy between the measured and simulated S_{11} is mainly due to the waveguide adapter. With a non-standard flange, it is not calibrated out of the measurements, resulting in considerable errors in measuring the reflection coefficient.

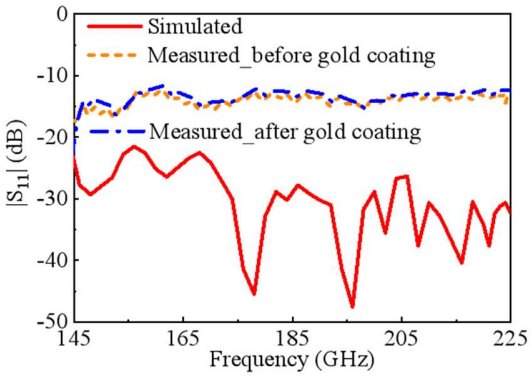
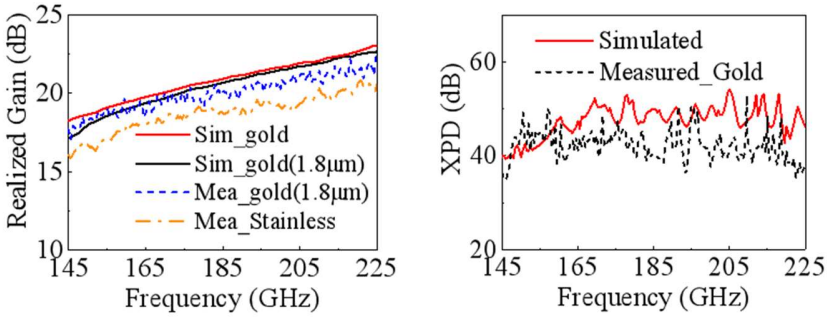


Fig. 7.7 Simulated and measured $|S_{11}|$ of the horn before and after gold coating.



(a) (b)

Fig. 7.8 Measurements in comparison with simulations: (a) peak gain before and after gold coating, (b) XPD of the proposed horn antenna.

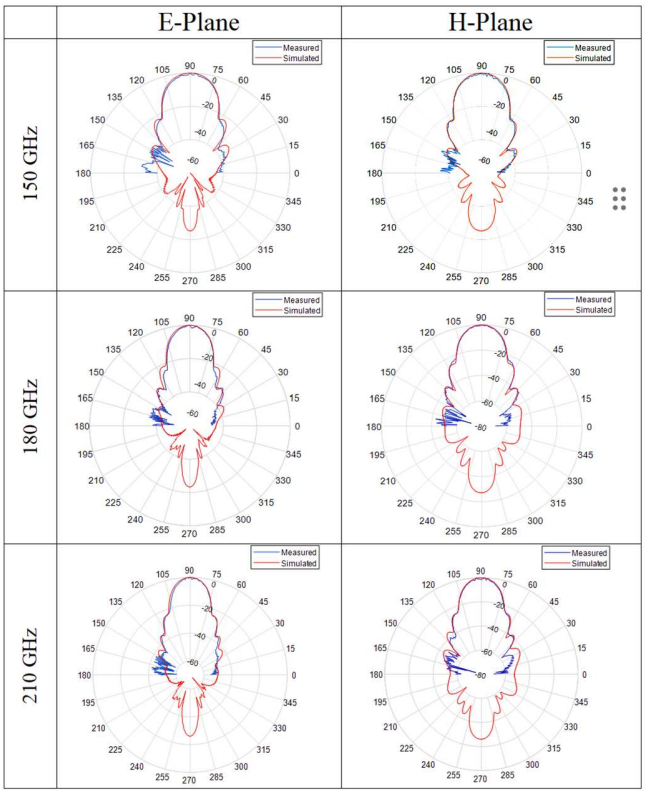


Fig. 7.9 Simulated and measured radiation patterns in E- and H-plane at 150,180 and 210 GHz.

TABLE I
COMPARISONS WITH OTHER PUBLISHED 3D PRINTED HORNS

Ref.	Type	Process	f (GHz)	XPD (dB)	Gain (dB)
[5]	CHorn[a]	Electroform	75-110	＞32	/
[7]	CHorn	LPBF	35-50	＜24	15
[8]	CHorn	LPBF	30-50	＜26.1	/
[10]	Horn	SLM[b]	60-90 110-170 220-325	/	22.2-24.5 22.8-25 21.5-24
[11]	Horn	SLA[c]	200-320	/	/
This work	CHorn (integrated adapter)	MLS	145-225	＞36	17.8-22

[a]λ_{min} is the wavelength at the lowest frequency

Its radiation performance was measured using an in-house far-field planar scanner system, as shown in Fig. 7.8. Over 145 to 225 GHz, the measured peak gain after gold coating varies from 18 to 22 dBi, which agrees very well with the simulated gain, predicted to rise from 18.2 to 22.3 dBi, shown in Fig. 7.8(a). The simulations have been considered effective conductivity due to surface roughness. The measured gain of the horn before the gold coating process is about 1.5 dB lower than that after gold coating. This is due to the poor electrical conductivity of stainless steel and the roughness of the surface before gold coating. Gold plating not only improves the electrical conductivity of the metal surface but also slightly enhances its surface smoothness.

The horn antenna achieves over 36 dB of XPD as shown in Fig. 7.8(b), thanks to the structure symmetry achieved by vertical printing. This is slightly lower than the simulated minimum XPD of 40 dB. The simulated and measured radiation patterns in E- and H-planes at 150, 180, and 210 GHz are presented in Fig. 7.9. The measured results are in very good agreement with the simulations, with the patterns almost overlapping. The simulated and measured sidelobes are all below -20 dB in both E-planes and H-planes. There are some small ripples around the main beam. This is due to scattering from the measurement set-up.

7.4 Conclusion

A sub-terahertz corrugated horn antenna made from stainless steel powder using the micro-laser sintering (MLS) process has been fabricated and characterized. This marks the highest operating frequency achieved for a corrugated horn antenna made with metal 3D printing technology. Far-field test results show that after applying a gold coating, the measured radiation patterns and gains exhibit excellent consistency with the simulation results, with the XPD exceeding 36 dB. The 45° angled corrugation design, combined with a bottom-up vertical printing approach, not only allows a monolithic print without requiring any internal support structure, but also reduces the risk of antenna performance degradation problems exhibited by horns printed at a tilted angle. The circular symmetry achieved delivers high XPD and wideband matching. The horn also incorporates the rectangular-to-circular waveguide transition in the same print. This work demonstrates a new, viable end-to-end manufacturing process for corrugated horns, with a precision printing technique and

an effective gold plating process. Compared to traditional manufacturing techniques, this method potentially offers shorter manufacture cycle, lower cost and new design flexibility for complex corrugated horn antennas used in sub-terahertz and terahertz bands.

Reference

[1] P. J. B. Clarricoats and A. D. Olver, Corrugated Horns for Microwave Antennas. *London, U.K: Peter Peregrinus Ltd.*, 1984.

[2] Z. Ying, A. A. Kishk, and P-S. Kildal, "Broadband compact horn feed for prime-focus reflectors," *Elec. Lett.,* vol. 31, no.14, pp. 1114-1115, 1995.

[3] A. Gonzalez, K. Kaneko, and S. Asayama, "Recent work on (sub-) mm-wave ultra-wideband corrugated horns for radio astronomy," in *Proc. IEEE 11th Eur. Conf. Antennas Propag.*, 2017, pp. 3327–3331.

[4] Y. Beniguel, A. Berthon, C. V. Klooster and L. Costes, "Design realization and measurements of a high performance wide-band corrugated horn," *IEEE Trans. Anten. Propag.*, vol. 53, no. 11, pp. 3540-3546, Nov. 2005.

[5] V. Bhavar, P. Kattire, V. Patil, S. Khot, K. Gujar, and R. Singh, "A review on powder bed fusion technology of metal additive manufacturing," *Additive Manufacturing Handbook*. Boca Raton, FL, USA: CRC Press, 2017, pp. 251 – 253.

[6] A. Gonzalez, K. Kaneko, C.-D. Huang, and Y.-D. Huang, "Metal 3D-printed 35-50-GHz corrugated horn for cryogenic operation," *J. Infrared Millimeter THz Waves*, vol. 42, no. 9, pp. 960 – 973, 2021.

[7] H. Kang, K. Kaneko, R. Sakai, and A. Gonzalez, "A Wideband Millimeter-Wave Corrugated Horn at 30-50 GHz Taking Advantage of All-Metal 3-D Printing Fabrication," *IEEE Antennas Wireless Propag. Lett.*, vol. 22, no. 6, pp. 1446-1450, June 2023.

[8] I. Agnihotri and S. K. Sharma, "Design of a 3D Metal Printed Axial Corrugated Horn Antenna Covering Full Ka-Band," *IEEE Antennas Wireless Propag. Lett.*, vol. 19, no. 4, pp. 522-526, Apr. 2020.

[9] B. Zhang, Z. Zhan, Y. Cao, H. Gulan, P. Linnér, J. Sun, T. Zwick, H. Zirath, "Metallic 3-D Printed Antennas for Millimeter- and Submillimeter Wave Applications," *IEEE Trans. Terahertz Sci. Techn.*, vol. 6, no. 4, pp. 592-600, July 2016.

[10] D. Rostyslav, A. S. Andy, E. Saleh, R. C. Jones, R. S. Donnan, C. J. Tuck , "Additive manufacturing of a terahertz back-to-back horn antenna for use in life sciences," *IEEE Trans. Compon. Packag. Manuf. Techn.,*vol. 12, no. 4, pp. 595-601, April 2022.

[11] T. Skaik, M. Salek, P. Hunyor, P. Huggard, H. Wang and P. Wilson, Y. Wang, "Evaluation of 3D Printed Monolithic G-band Waveguide Components," *IEEE Trans. Compon. Packag. Manuf. Techn.*, 13(2), pp. 240-248, Feb. 2023.

[12] Y. Yu, Y. Wang, T. Skaik, T. Starke, X. Shang, M. Lancaster, P. Hunyor, P. Huggard, H. Wang, M. Harris, M. Beardsley, Q. Cheng, "D-band Waveguide Diplexer Fabricated Using Micro Laser Sintering," *IEEE Trans. Compon. Packag. Manuf. Techn.*, vol. 12, no. 9, pp. 1446 – 1457, Sept. 2022.

[13] T. Skaik, Y. Wang, M. Salek, P. Hunyor, H. Wang, P. G. Huggard, T. Starke, M. Attallah and R. Martinez, "A 3D Printed 300 GHz Waveguide Cavity Filter by Micro

Laser Sintering", *IEEE Trans. Terahertz Sci. Techn.*, vol. 12, no. 3, pp. 274-281, May 2022.

[14] T. Skaik, D. Wang, P. Hunyor, H. Wang, P. G. Huggard, T. Starke, Q. Zhang, Y. Wang, "A 3D Printed V-Band Twisted Monolithic Waveguide Bandpass Filter," in 53rd *Eur. Microw. Conf. (EuMC)*, Berlin, Germany, 2023, pp. 231-234.

[15] J. Cao, W. Wang, W. Song B. Chen, "Study of the Scanning Characteristics of On-board Reflector Antenna with 7-feed Cluster." *J. Phys.: Conf. Series.* vol. 1802. no. 2. IOP Publishing, 2021.

[16] G. L. James and B. M. Thomas, "TE11-to-HE11 Cylindrical Waveguide Mode Converters Using Ring-Loaded Slots." *IEEE Trans. on Microwave Theory and Tech,* vol. 30, no. 3, pp. 278-285, Mar. 1982.

[17] E. Hammerstad and O. Jensen, "Accurate models for microstrip computer-aided design," in *IEEE MTT-S Int. Microw. Symp. Dig.*, 1980, pp. 107–409.

CHAPTER 8: CONCLUSIONS AND FUTURE WORK

8.1 Conclusions

This thesis addresses key challenges in expanding bandwidth for dual-polarized waveguide array antennas, introduces innovative topologies for multi-band shared-aperture dual-polarized antennas, and establishes advanced design methodologies for ultra-wideband waveguide array antennas. It also explores the use of high-precision 3D printing in manufacturing sub-terahertz corrugated horn antennas.

Chapter 3 demonstrates a novel feeding topology for dual-polarized slot array antennas based on a hollow waveguide (HW) structure. By implementing two distinct wideband full-corporate-feed networks, the method minimizes slot spacing to less than one free-space wavelength at the highest operating frequency, ensuring efficient dual polarization. This approach, validated through CNC milling and laser cutting, achieved over 25.5 dBi peak gain and more than 81.5% efficiency across 17-21.5 GHz, with excellent isolation and XPD. These results demonstrate significant advancement for high-data-rate applications like satellite and 5G millimeter-wave communications.

Chapter 4 presents a pioneering method using 3D printing technology to develop a wideband, dual-polarized hollow-waveguide antenna array. The proposed approach integrates a dual-mode back cavity operating in multiple modes with a diamond-shaped radiation slot, achieving broad bandwidth and stable radiation patterns. The design-for-manufacture strategy, leveraging SLA printing and copper plating, significantly simplifies the feeding network, facilitating wider bandwidths and improved waveguide antenna performance.

Chapter 5 introduces a method for developing a dual-band, dual-polarized (DBDP) waveguide antenna array that employs orthogonal continuous transverse stub (CTS) arrays with DBDP parallel plate waveguide (PPW) feed networks and bandstop structures. This approach effectively manages polarization leakage and allows flexible frequency band adjustments up to 2.64:1. The method achieved over 18% fractional bandwidth in the K-band and over 12% in the Ka-band, offering a highly efficient and adaptable solution for advanced SATCOM applications.

Chapter 6 showcases an ultra-wideband planar antenna design methodology that achieves a 105% fractional bandwidth over 10 to 32 GHz with aperture efficiencies reaching up to 90%. By employing a corporate feed network that directly excites quasi-TEM radiators in a one-to-one configuration, this method greatly enhances both bandwidth and efficiency. The experimental results confirm the potential of this design for point-to-point and SATCOM systems, offering a scalable, high-gain solution for wideband applications.

Chapter 7 investigates the design and fabrication of sub-terahertz corrugated horn antennas using Micro Laser Sintering (MLS) metal 3D printing, addressing the limitations of planar waveguide arrays at these frequencies. The proposed monolithic 3D-printed horn features a 45° inclined corrugation design, allowing vertical printing without internal support, which preserves circular symmetry and optimizes radiation performance. The method successfully achieves over 36 dB XPD and 18–22 dBi gain across 145–225 GHz, demonstrating the first high-performance 3D-printed metal corrugated horn beyond 100 GHz. These findings establish horn-fed reflector antennas as a viable alternative to planar

waveguide arrays in sub-terahertz applications, providing a more practical and scalable approach for high-frequency SATCOM, radar, and sensing systems.

8.2 Future Work

From what has been investigated and achieved as well as from the lessons learned throughout this thesis, more research and development opportunities have been manifested. Three examples are given as follows:

(1) Lightweight and Low-Profile Design for Dual-Polarized Hollow Waveguide Array Antennas

One research direction is to reduce the size, weight, and profile of dual-polarized hollow waveguide array antennas to enhance their integration into compact, high-frequency communication systems. Additionally, advanced manufacturing techniques, such as precision machining and metal 3D printing, could help achieve thinner walls and more compact structures without compromising mechanical stability or radiation characteristics. These efforts will be particularly valuable for aerospace and satellite applications, where weight and volume constraints are critical.

(2) High-Efficiency Beam-Scanning Waveguide Antennas for LEO SATCOM

The increasing deployment of low Earth orbit (LEO) satellite constellations necessitates the development of high-efficiency beam-scanning waveguide antennas to support seamless connectivity and dynamic beam control. Future research should explore beam scanning waveguide arrays, leveraging phase-shifting techniques, traveling-wave feed architectures, and hybrid waveguide-lens designs to achieve wide-angle beam scanning while maintaining high aperture efficiency. The integration of multi-beam feed networks can further enhance coverage and flexibility, enabling more efficient spectrum utilization for next-generation satellite communication systems.

(3) Extending Metal 3D Printing to Array Antenna Fabrication

The successful implementation of Micro Laser Sintering (MLS) metal 3D printing for sub-terahertz corrugated horns demonstrates the feasibility of using additive manufacturing for high-frequency antennas. Future research could extend MLS-based fabrication to waveguide arrays, enabling monolithic, high-precision, multi-band, and dual-polarized antenna structures. This approach can simplify assembly, reduce losses at interconnections, and unlock new design possibilities for waveguide-fed phased arrays and shared-aperture systems.